National Library of Canada
Acquisitions and Bibliographic Services Branch
395 Wellington Street
Ottawa, Ontario
K1A 0N4

Bibliothèque nationale du Canada
Direction des acquisitions et des services bibliographiques
395, rue Wellington
Ottawa (Ontario)
K1A 0N4

Your file Votre référence

Our file Notre référence

NOTICE

The quality of this microform is heavily dependent upon the quality of the original thesis submitted for microfilming. Every effort has been made to ensure the highest quality of reproduction possible.

If pages are missing, contact the university which granted the degree.

Some pages may have indistinct print especially if the original pages were typed with a poor typewriter ribbon or if the university sent us an inferior photocopy.

Reproduction in full or in part of this microform is governed by the Canadian Copyright Act, R.S.C. 1970, c. C-30, and subsequent amendments.

AVIS

La qualité de cette microforme dépend grandement de la qualité de la thèse soumise au microfilmage. Nous avons tout fait pour assurer une qualité supérieure de reproduction.

S'il manque des pages, veuillez communiquer avec l'université qui a conféré le grade.

La qualité d'impression de certaines pages peut laisser à désirer, surtout si les pages originales ont été dactylographiées à l'aide d'un ruban usé ou si l'université nous a fait parvenir une photocopie de qualité inférieure.

La reproduction, même partielle, de cette microforme est soumise à la Loi canadienne sur le droit d'auteur, SRC 1970, c. C-30, et ses amendements subséquents.

Canada

University of Alberta

Isolation Current Measurement System with Magnetic Coupling

by

Andrew Vainshtein

A thesis
submitted to the Faculty of Graduate Studies and Research
in partial fulfillment of the requirements for the degree
of Master of Science

Department of Electrical Engineering

Edmonton, Alberta
Fall 1995

National Library
of Canada

Acquisitions and
Bibliographic Services Branch

395 Wellington Street
Ottawa, Ontario
K1A 0N4

Bibliothèque nationale
du Canada

Direction des acquisitions et
des services bibliographiques

395, rue Wellington
Ottawa (Ontario)
K1A 0N4

Your file Votre référence

Our file Notre référence

THE AUTHOR HAS GRANTED AN IRREVOCABLE NON-EXCLUSIVE LICENCE ALLOWING THE NATIONAL LIBRARY OF CANADA TO REPRODUCE, LOAN, DISTRIBUTE OR SELL COPIES OF HIS/HER THESIS BY ANY MEANS AND IN ANY FORM OR FORMAT, MAKING THIS THESIS AVAILABLE TO INTERESTED PERSONS.

L'AUTEUR A ACCORDE UNE LICENCE IRREVOCABLE ET NON EXCLUSIVE PERMETTANT A LA BIBLIOTHEQUE NATIONALE DU CANADA DE REPRODUIRE, PRETER, DISTRIBUER OU VENDRE DES COPIES DE SA THESE DE QUELQUE MANIERE ET SOUS QUELQUE FORME QUE CE SOIT POUR METTRE DES EXEMPLAIRES DE CETTE THESE A LA DISPOSITION DES PERSONNE INTERESSEES.

THE AUTHOR RETAINS OWNERSHIP OF THE COPYRIGHT IN HIS/HER THESIS. NEITHER THE THESIS NOR SUBSTANTIAL EXTRACTS FROM IT MAY BE PRINTED OR OTHERWISE REPRODUCED WITHOUT HIS/HER PERMISSION.

L'AUTEUR CONSERVE LA PROPRIETE DU DROIT D'AUTEUR QUI PROTEGE SA THESE. NI LA THESE NI DES EXTRAITS SUBSTANTIELS DE CELLE-CI NE DOIVENT ETRE IMPRIMES OU AUTREMENT REPRODUITS SANS SON AUTORISATION.

ISBN 0-612-06549-9

Canada

University of Alberta

Library Release Form

Name of Author: Andrew Vainshtein

Degree: Master of Science

Year this Degree Granted: 1995

Permission is hereby granted to the University of Alberta Library to reproduce single copies of this thesis and to lend or sell such copies for private, scholarly, or scientific research purposes only.

The author reserves all other publication and other rights in association with the copyright in the thesis, and except as hereinbefore provided, neither the thesis nor any substantial portion thereof may be printed or otherwise reproduced in any material form whatever without the author's prior written permission.

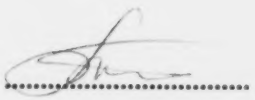

232 Hillcrest Place
Edmonton, Alberta
Canada, T5R 5X6

Sept 22, 1995

University of Alberta

Faculty of Graduate Studies and Research

The undersigned certify that they have read, and recommend to the Faculty of Graduate Studies and Research for acceptance, a thesis entitled
Isolation Current Measurement System with Magnetic Coupling
submitted by Andrew Vainshtein in partial fulfillment of the requirements for the degree of Master of Science

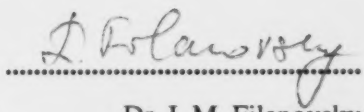

Dr. I. M. Filanovsky

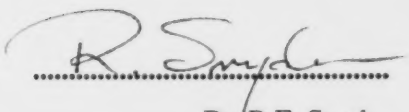

Dr. R.E. Snyder

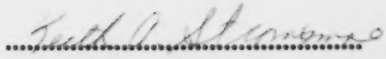

Dr. K. A. Stromsmoe

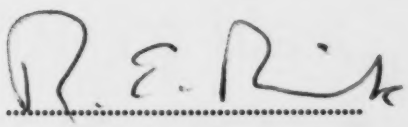

Dr. R.E. Rink

Abstract

An approach to design isolation current sensors is presented. The basic bipolar current sensor comprises a magnetic multivibrator which uses one of the nonlinear coil windings. The oscillation duty ratio in this multivibrator is modulated by the input current signal applied to another coil winding. Several magnetization models are considered in order to quantitatively describe the current sensor operation. Output characteristics of the sensor were obtained for linear-saturable model (both with and without hysteresis), piecewise approximation with arbitrary number of segments, polynomial approximation. Application limits and error factors for the presented magnetization models are discussed. The mathematical simulation was complemented by the SPICE computer simulation. Analog and digital data processing mechanisms supporting the high frequency operation of the basic isolation current sensor are presented. The highest possible conversion speed and maximal measurement bandwidth can be achieved by combining the dual integration with the sample-and-hold operation. Several designs based on this concept were generated. An experimental sensor operating at the frequency 25 kHz can measure an input current in a range $\pm(0.2 - 2.2)$ mA. The nonlinearity of the circuit for input signals from dc to 1500 Hz is 0.08 %.

Table of contents

1. INTRODUCTION TO ISOLATION MEASUREMENTS.....1

1.1. APPLICATION OF ISOLATION MEASUREMENT SYSTEMS.....1

1.2. TECHNIQUES FOR ISOLATION.....2

1.3. CURRENT SENSING DEVICES WITH MAGNETIC COUPLING.....3

1.4. OBJECTIVES OF THE PROJECT.....7

1.5. THESIS CONTENT.....8

2. OSCILLATOR WITH NONLINEAR MAGNETIC COUPLING AS A BASIS FOR ISOLATION CURRENT TRANSDUCER.....9

2.1. INTRODUCTION TO MAGNETIZATION CURVES APPROXIMATION.....9

2.1.1. Piecewise approximation.....10

2.1.2. Polynomial and power series.....13

2.1.3. Froelich's function.....13

2.1.4. Arctan and Sinh functions.....14

2.1.5. Jiles-Atherton model.....14

2.1.6. The choice of magnetization model.....15

2.2. LINEAR - SATURABLE MAGNETIZATION MODEL.....16

2.2.1. Anhysteretical linear-saturable model.....17

2.2.2. Linear - saturable coil with hysteresis.....21

2.2.3. Current versus flux control in a current transducer circuit.....22

2.2.4. Transient current in a linear-saturable coil.....23

2.2.5. Reference levels.....24

2.2.6. Calculated transient characteristics for linear-saturable model.....26

2.3. PIECEWISE LINEAR APPROXIMATION.....31

2.3.1. Transient analysis.....31

2.3.2. Calculation example.....36

2.3.3. Magnetization loops distortion.....38

2.3.4. ΔT offset and hysteresis errors.....40

2.4. POLYNOMIAL APPROXIMATION.....42

2.4.1. Transient analysis....42
2.4.2. Formatting of the output signal....44
2.4.3. Application limits of the polynomial model....50
2.5. SPICE SIMULATION....51
2.5.1. Circuit and simulation data....51
2.5.2. Discussion of the SPICE results....57
2.6. CONCLUDING REMARKS....60
3. TRANSDUCER CIRCUIT CONFIGURATIONS AND DATA PROCESSING....61
3.1. FILTERING....61
3.2. DUAL INTEGRATION WITH SAMPLE-AND-HOLD....62
3.2.1. Basic circuit structure....62
3.2.2. Dual integration with leading sample-and-hold....65
3.2.3. Bandwidth limitations....65
3.2.4. Boosting the oscillation frequency and dead zone reduction....71
3.2.5. Increasing the dynamic range of dual integration....75
3.2.6. Flux saturation detector....77
3.2.7. Suppression of the oscillation frequency interference in a primary loop....77
3.3. DIGITAL PROCESSING....78
4. DESIGN OF THE ISOLATION MEASUREMENT SYSTEM....82
4.1. PERFORMANCE PARAMETERS....82
4.1.1. Current range....82
4.1.2. Operating temperature range....83
4.1.3. Power consumption....84
4.1.4. Isolation voltage....84
4.2. DESIGN EXAMPLES....85
4.2.1. Basic low-frequency circuit....85
4.2.2. Basic low-frequency circuits experimental results....88
4.2.3. High frequency isolation current measurement circuit....95

4.2.4. High frequency circuit experimental results.....99
4.2.5. Circuits with dead zone reduction.....105
4.2.6. Experimental results for the circuit with DZR.....108
4.2.7. IC digital processor for the isolation current transducer.....111
4.2.8. Testing of the IC.....111
4. 3. CONCLUDING REMARKS.....112
5. CONCLUSION.....113
REFERENCES.....119
APPENDIX 1. PSPICE SIMULATION.....124
APPENDIX 2. FPGA IC - DIGITAL PROCESSOR FOR CURRENT SENSOR.....128

List of figures

Fig. 1. General configuration of isolation systems....2
Fig. 2. RL-multivibrator with nonlinear transformer....6
Fig. 3. Piecewise linear model....10
Fig. 4. Typical dc magnetization characteristics for Magnesil and Supermendur....12
Fig. 5. Linear - saturable model....16
Fig. 6. Flux linkage waveform for linear-saturable coil....17
Fig. 7. Linear-saturable magnetization characteristic with hysteresis....21
Fig. 8. Current in saturable coil....23
Fig. 9. Definition of the reference levels....25
Fig. 10. Sensitivity of the current transducer for different IREF settings....26
Fig. 11. Circuit used for sample calculation....27
Fig. 12. Calculated characteristics of the current sensor with 2826MB amorphous core transformer....28
Fig. 13. Calculated characteristics of the current sensor with Supermendur core transformer....29
Fig. 14. Calculated duty cycle of the current sensor output signal for 2826MB and Supermendur core transformers....30
Fig. 15. Piecewise linear representation of a magnetization curve....32
Fig. 16. Discrete presentation of the RL-multivibrator waveforms....33
Fig. 17. Three-section magnetization model....35
Fig. 18. Comparison of the linear-saturable and three-section piecewise models for the Supermendur core....37
Fig. 19. Undersaturated current transducer mode....38
Fig. 20. Displacement of the magnetization curve n-th section....39
Fig. 21. Magnetization loop displacement "memory"....41
Fig. 22. Waveforms of the coil current for polynomial model....43
Fig. 23. Calculated sensitivity of combined terms of the sensor output signal....46
Fig. 24. Calculated sensor output characteristic Y3....47
Fig. 25. Calculated output signal frequency as a function of input current....48

Fig. 26. Calculated output signal frequency as a function of input current.....49
Fig. 27. PSpice schematics.....51
Fig. 28. Simulated waveforms of coil current and Schmitt trigger output for input current -200 mA.....52
Fig. 29. Simulated waveforms of coil current and Schmitt trigger output for input current +200 mA.....53
Fig. 30. Simulated B-iL loop for input current +200 mA.....54
Fig. 31. Simulated B-iL loop for input current -200 mA.....55
Fig. 32. Simulated waveforms of coil excitation current for ac input current.....56
Fig. 33. Current sensor output characteristic according to the polynomial model and PSpice.....59
Fig. 34. Direct filtering of the transducer output signal.....61
Fig. 35. Block diagram of the transducer with dual integration and S/H.....62
Fig. 36. Timing diagrams of the dual integration - S/H.....62
Fig. 37. Control signals in the INTEGRATOR - S/H circuit.....64
Fig. 38. Current transducer with leading sampling.....65
Fig. 39. Zero-hold operation of the S/H output.....66
Fig. 40. Rectangular (rect) function and its inverse transform.....66
Fig. 41. Amplitude distortion error of the current sensor.....68
Fig. 42. Switching error evaluation model.....70
Fig. 43. Reference level effect on the sensitivity and oscillation frequency.....71
Fig. 44. Dead zone of the current transducer.....72
Fig. 45. Transducer with dead zone reduction (DZR) function.....74
Fig. 46. Increasing the dynamic range of dual integration.....76
Fig. 47. Interference suppresser.....78
Fig. 48. Digital processing.....80
Fig. 49. Loop displacement vs magnetization loop uncertainty.....82
Fig. 50. Basic low-frequency current sensor.....86
Fig. 51. Basic low-frequency current sensor with output filter and feedback.....87

Fig. 52. Experimental coil current waveforms for low frequency current sensor and dc input current....89
Fig. 53. Coil current for ac input current (low-frequency current sensor)....90
Fig. 54. Experimental output characteristics of the low-frequency isolation current sensor without feedback (dc input current)....91
Fig. 55. Experimental large - signal output characteristic of the current sensor with feedback....92
Fig. 56. Experimental small - signal output characteristic of the current sensor with feedback....93
Fig. 57. Oscillation frequency of the current sensor as a function of input current....94
Fig. 58. Schematics of the current transducer for 25-50 kHz operating frequency....97
Fig. 59. Timing diagram of the current transducer for 25-50 kHz operating frequency....98
Fig. 60. S/H output signal for 25 kHz current sensor without feedback (dc input current)....100
Fig. 61. S/H output signal for 25 kHz current sensor with feedback....101
Fig. 62. Hysteresis of the current sensor as a function driving current....102
Fig. 63. S/H output of the current sensor with feedback and suppression of hysteresis....103
Fig. 64. Frequency response of the isolation current sensor....104
Fig. 65. Current sensor with dead zone reduction....106
Fig. 66. Current sensor with dead zone reduction designed with additional excitation voltage sources....107
Fig. 67. Output characteristics of the isolation current sensor with DZR....109
Fig. 68. Sensitivity of the isolation current sensor with DZR as a function of oscillation frequency....110

List of symbols and abbreviations

A	thermal energy parameter
ac	alternating current
B	magnetic flux density
CMOS	complementary metal-oxide semiconductor
dc	direct current
DCCT	direct current current transformer
DZR	dead zone reduction
ECG	electrocardiogram
F	magnetomotive force
f	frequency
f_d	driving frequency
FPGA	field programmable gate array
GPIB	general purpose interface bus
H	magnetic field strength
$H(\omega)$	transfer function
I_S	saturation current
IA	isolation amplifier
IC	integrated circuit
L	inductance
MOS-FET	metal oxide silicon field effect transistor
M	magnetization
M_{an}	anhysteretic magnetization
M_S	saturation magnetization
OA	operational amplifier
P-PW-V	voltage - pulse-width - voltage conversion
S	sensitivity
S/H	sample-and-hold
S/N	signal to noise ratio
SPICE	circuit simulation software package

SR	slew rate
t_{pd}	propagation delay
UPS	unity power system
V_{SRC}	voltage source
V - f - V	voltage - frequency - voltage conversion
α	interdomain coupling parameter
β	Raleigh constant
δ_a	amplitude distortion error
δ_c	relative counting error
δ_{sw}	relative switching error
λ	coil ratio
μ	magnetic permeability
Φ	flux
Θ	phase shift
ρ	hysteresis parameter
ψ	flux linkage
ψ_s	saturation flux linkage

1. Introduction to isolation measurements

1.1. Application of isolation measurement systems

A class of measurement systems galvanically isolated from a signal source is commonly referred to as "isolation systems". Such systems are used in three categories of applications:

- measurement of low level signals in the presence of high common-mode voltages
- elimination of severe ground noise
- fault protection for either the source of the measurement data or its receiver or both.

Isolation systems are widely used in remote measurements of electrical power equipment where high common-mode voltage (to thousands of volts) can easily damage a data-acquisition circuit. It is likewise possible that protection is needed from accidental high voltages arising downstream, in order to protect an object which is being measured. A relevant example is a transducer located inside a gas tank and connected to a remote computer. If no isolation is used, possible short circuits and faults in a sensor's interface may cause sparks and gas ignition.

Two-way isolation protection is needed in medical patient monitoring equipment for systems providing electrocardiogram (ECG) monitoring. A patient must be protected from an accidental electric shock caused by the ECG machine. However, if the patient's heart stopped and high voltage pulses (>7.5 kV) are applied by a defibrillator the ECG machine itself must be protected.

As presented in Fig. 1, an isolation measurement system is comprised of two sections with an isolation gap between them. An input current or voltage signal is converted inside a primary section to a special form allowing its passage through the isolation barrier; at the measurement side incoming data are converted back to a suitable format for further processing. Power supplies of both sections must also be isolated. This requirement is met by either transmitting power from the measurement to the primary

side or by using autonomous power supplies for each section. Power can also be transmitted from a power unit isolated from both the primary and measurement sections. Such a configuration is called "3-port isolation".

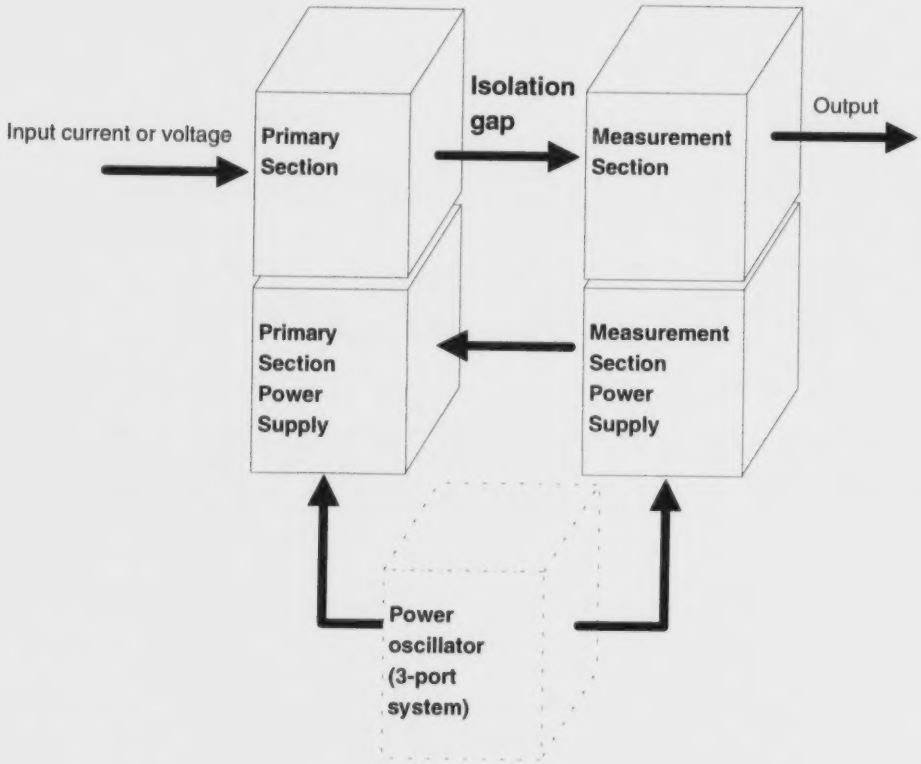

Fig. 1. General configuration of isolation systems

1.2. Techniques for isolation

World leading analog integrated circuits (IC) and instrumentation manufacturers have their own lines of isolation products that now include single-chip and hybrid amplifiers, isolation channels, signal conditioning modules and various isolation sensors [1 - 7].

Three major principles are used to transmit measurement data across the isolation barrier. These include: transformer magnetic coupling, capacitive coupling and optical coupling. Modulator-demodulator structures such as V-PW-V (voltage-pulse width -

voltage) and V-f-V (voltage-frequency-voltage) are common for transformer based circuits [1 - 3]. In 1995 the Analog Devices Corporation offers five isolation amplifiers (IA) with magnetic coupling. The company projects [1] that transformer based amplifiers will achieve 16 bits analog accuracy with several hundred kHz bandwidth and maximum isolation voltage at 10 kV. These ratings are still far from the best specifications to date: the fastest 3-port AD210 provides 12 bit (0.025%) accuracy , 20 kHz bandwidth and 3.5 kV isolation.

The Burr-Brown Corporation in 1995 has two transformer based isolation amplifiers with 8 kV isolation, amplitude modulation-demodulation, 12 bit accuracy and a power supply which is isolated from both sides [3].

Capacitive isolation circuits represent a relatively new trend in isolation technology which employs a concept of switching capacitors [3], [9]. There are several amplifiers available on the market with a typical bandwidth of 50-70 kHz, isolation from 2 to 8 kV and nonlinearity about 0.02% [1], [3]. All these circuits require a separate power supply which cannot be provided via capacitors. To solve this problem the Burr-Brown Corporation developed an amplifier with mixed capacitor and transformer isolation; the latter is used for power conversion.

The third type of isolation system is based on opto-isolators, comprising a LED - photocell pair. These circuits also require separate power supplies for primary and measurement sections. Opto-coupled amplifiers are considered less accurate and less linear than the previous two types, but they are the least expensive [1].

1.3. Current sensing devices with magnetic coupling

Isolation current measurements are required in power electronics, industrial robots and motor drives. Isolation current control loops and overcurrent protection circuits are widely used in DC-DC converters and unity power systems (UPS).

Although isolation amplifiers (IA) can be used in many of the above applications, these devices are quite expensive and generally require additional circuits to convert current into voltage. For example, to implement a motor control current sensor using a AD210 an additional instrumentation OA is recommended to amplify the small signal from a low-resistance shunt [1]. This additional OA must be powered from the primary section of the AD210.

An alternative approach to isolation current measurements involves specially designed current magnetic sensors exploiting some sort of nonlinear or saturable core operation. These sensors can be considered as an economical solution in all applications which do not require ultra-high precision. The unique application area of these devices are noncontact current measurements where there are no shunt resistors and accordingly IA can be used. There are several known sensor types. Among them are:

- second harmonic type modulator
- dc current transformer
- apparent coercive field strength measurement
- balancing type
- transistor core multivibrator

A family of current sensors that operates on the basis of the so-called DCCT (dc current transformer) was designed by Kiwaki et al. from Hitachi Research Laboratory [8]. A DCCT sensor comprises a magnetic coil with 2 to 4 windings on the measurement side included in a bridge circuit. The core is forced into saturation according to the sequence set by additional ac sources. The signal from two bridges is fed into a differential amplifier. This configuration allows one to measure a dc input current in the primary winding. The developed sensors range from ±100 A to ±1000 A with rated output ±5 V and accuracy ±0.5%. It is also reported that a ±1000 A sensor with an accuracy of 0.0014% was designed for precision power supplies [8].

A current sensor based on the effect of magnetization loop shift by an external current was proposed by Son and Sievert [11]. To measure this shift (which the authors denote as apparent coercive field strength) the circuit contains an ac driving source which is applied to two identical windings. While the first winding is connected to the input current the second acts as a reference. The differential signal is measured at the times when the magnetization loops of the above coils are crossing the zero. The circuit provides 0.01% nonlinearity for dc input currents of 0 to 1A. As reported, the circuit can be designed to operate up to 20 kHz.

The balancing-type weight scale resembling the charge-balance principle used in analog-digital converters was proposed by Sonoda, Ueda and Koga [10]. To measure the unknown current the sensor uses a reference triangular voltage source which is applied to the core via an additional winding. The reference bipolar magnetic field and the field from the input current are superimposed in a core. A zero flux detector is used to determine the moment when both sources are equal. The sensor operates with an input current of 50 mA to 10 A from dc to several hundred Hertz providing 0.01% accuracy.

A transistor multivibrator with two MOS-FETs controlled by a small magnetic core was reported by Harada and Sakamoto [12]. The circuit uses the resonance between the FET's gate-source capacitance and the saturating inductance of the core. A current sensor designed on this principle operates in the ±10 A range from dc to 40 kHz.

A novel concept allowing current measurements via an isolation gap in a wide range of frequencies including dc was proposed and investigated by Filanovsky, Piskarev and Taylor [13 - 16]. The basic circuit shown in Fig. 2 employs a coil and a comparator which are connected into a RL-multivibrator circuit. A current limiting resistor R1 in series with a driving winding is chosen in such a way that the coil operates in a nonlinear mode approaching saturation in each oscillation half-cycle.

magnetic field modifies the core's saturation condition, which in turn alters the oscillation duty cycle.

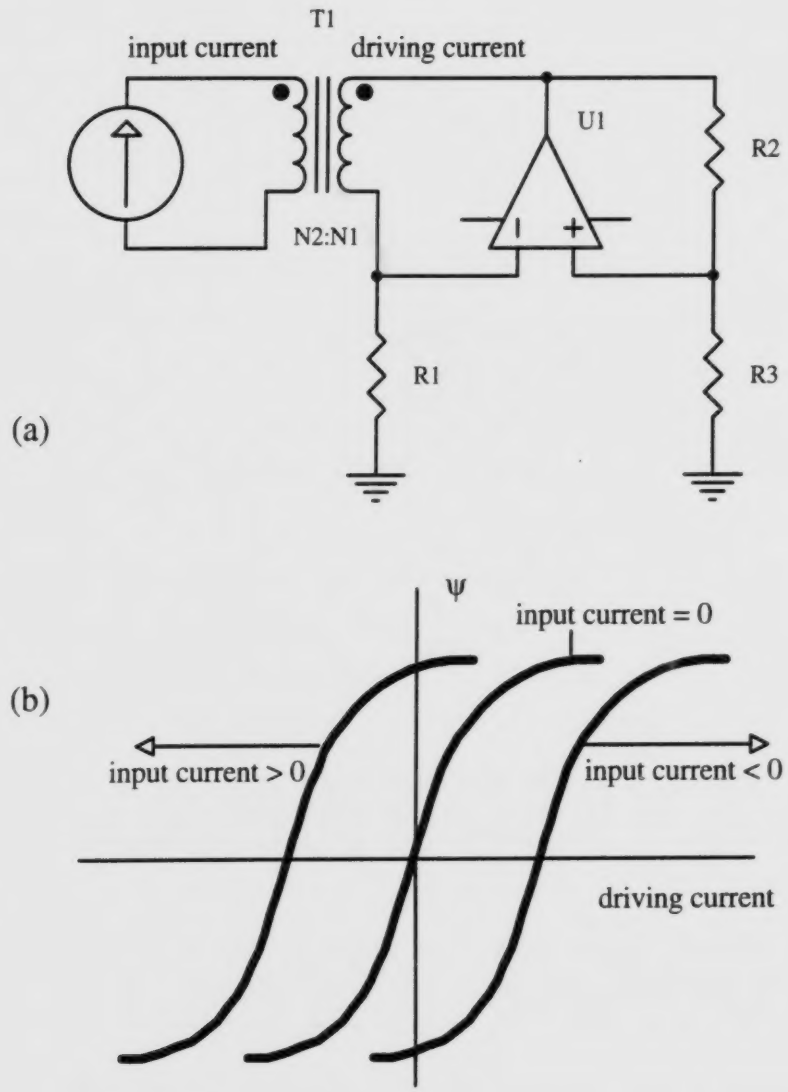

Fig. 2. RL-multivibrator with nonlinear transformer

(a) schematics, (b) magnetization curve

The sensor transfer characteristics were simulated using 2-segment piecewise and power series (cubic) approximation of the core magnetization characteristic. It was demonstrated that the duty cycle is proportional both to the value and polarity of the measured current. The obtained output characteristic of the current sensor were close to linear. Experimental verification of the theoretical model was performed using a low-frequency pulse transformer.

1.4. Objectives of the project

This project is intended to study further the class of isolation measurement circuits proposed by Filanovsky, Piskarev and Taylor. Specifically the project is aimed to:

1) study and quantitatively describe the current sensor using
(a) piecewise approximation with arbitrary number of segments;
(b) power series approximation with output signal formatting;
(c) SPICE simulation;

2) develop data processing circuits supporting high frequency operation of the above current sensor;

3) investigate error sources and limitation factors affecting the sensor's accuracy, sensitivity and frequency bandwidth and develop procedures for their minimization;

4) design practical current sensors and experimentally verify the proposed data processing mechanisms.

1.5. Thesis content

Beyond this introduction the thesis contains four chapters. Chapter 2 is concerned with magnetization curve simulation and sensor circuit analysis. Linear - saturable, general piecewise and polynomial models were used to describe the behavior of a nonlinear coil. The results of the analysis were then compared with the SPICE simulation in a version employing the Jiles-Atherton magnetization model.

Data processing methods used for conversion of the primary sensor's signal into analog and/or digital format are discussed in Chapter 3. Circuit configurations for both analog and digital versions are considered. The same chapter presents an insight into error sources, bandwidth limitations and techniques for improving the circuit performance.

Several designed and tested analog circuits and custom digital FPGA IC are presented in Chapter 4 along with the experimental results obtained.

2. Oscillator with nonlinear magnetic coupling as a basis for isolation current transducer

It is our intention to investigate further the concept of current transducer with magnetically coupled multivibrator [13], [14]. To accomplish this goal we should obtain an adequate quantitative model of the fundamental switching network comprising a nonlinear coil and consider ways to process the output data. In this chapter the circuit transient behavior is discussed in regard to the transducer output signal with special attention given to coil magnetization models. General performance characteristics such as current range, sensitivity and bandwidth are considered with respect to different magnetic materials and their properties.

2.1. Introduction to magnetization curves approximation

Due to the fact that most B-H characteristics depend on the previous history of ferromagnetic material their behavior is not generally governed by a single law in a form of an algebraic or another expression. According to the review by Cullity [20] in only three cases have adequate expressions been developed for the B-H curves. The first is the Raleigh law which is valid for low H for many ferromagnetics. It states that

$$B = \mu H + \beta H^2$$

where μ is the initial permeability and β is the Raleigh constant. The other two cases include high field curves for single crystals studied by Williams [21] and the law of approach to saturation (typical for polycrystals) obtained by Chikazumi [22].

In the following synopsis of magnetization models we shall briefly consider only those which deal with reversible magnetization. Reversible processes result in energy stored and released but not dissipated. Here it is assumed for all circuits evaluated that irreversible phenomena such as Barkhausen noise and eddy currents introduce some errors, but do not affect the basic shape of magnetization curves.

2.1.1. Piecewise approximation

In this model a B-H characteristic is divided into several sections, which are then linearized. Fig. 3a presents a piecewise transformation of a sigmoid-type loop which is typical for many ferromagnetic materials.

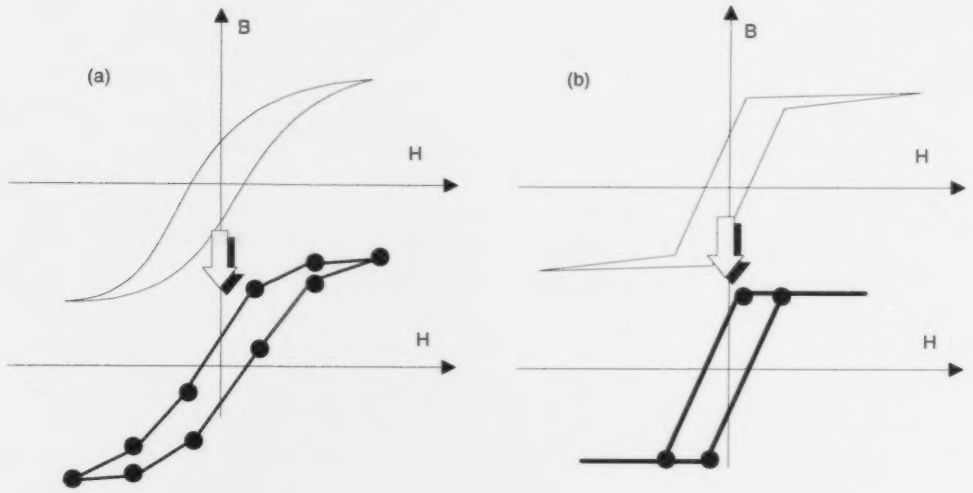

Fig. 3. Piecewise linear model for (a) sigmoid type B-H curve, (b) rectangular B-H curve (linear-saturable model)

If the hysteresis shown in Fig. 3 is neglected, then for small H, the B-H curve can be modeled by a straight line set through the origin of the coordinate system. Another straight line section is added at the point where H increases and the initial assumption of constant magnetic permeability is no longer valid. This point is commonly called the "saturation knee". Further simulation segments and eventual saturation cutoff can be added to the model subject to particular ferromagnetic properties.

Piecewise approximation can be applied to an arbitrary curve and can be easily obtained from the experimental data. A considerable number of piecewise approximation models have been reported for various magnetic materials [24 - 26]. The negative side of this model is the discontinuity of the first derivatives of B with respect to H and, sometimes, an excessive number of linear segments.

The linear-saturable model (Fig. 3b) is the simplest 3-section case of the piecewise linear simulation. This model is applicable to a number of ferromagnetic materials with sharp rectangular magnetization characteristics. Many of the materials specifically developed for magnetic amplifiers, current transformers and magnetometers match the linear-saturable model as the squareness of their B-H curves approaches 90%. As an example, Fig. 4 presents magnetization curves of highly refined cobalt-iron alloy Supermendur®, and silicon-iron alloy Magnesil® [27].

Fig. 4. Typical dc magnetization characteristics for Magnesil and Supermendur

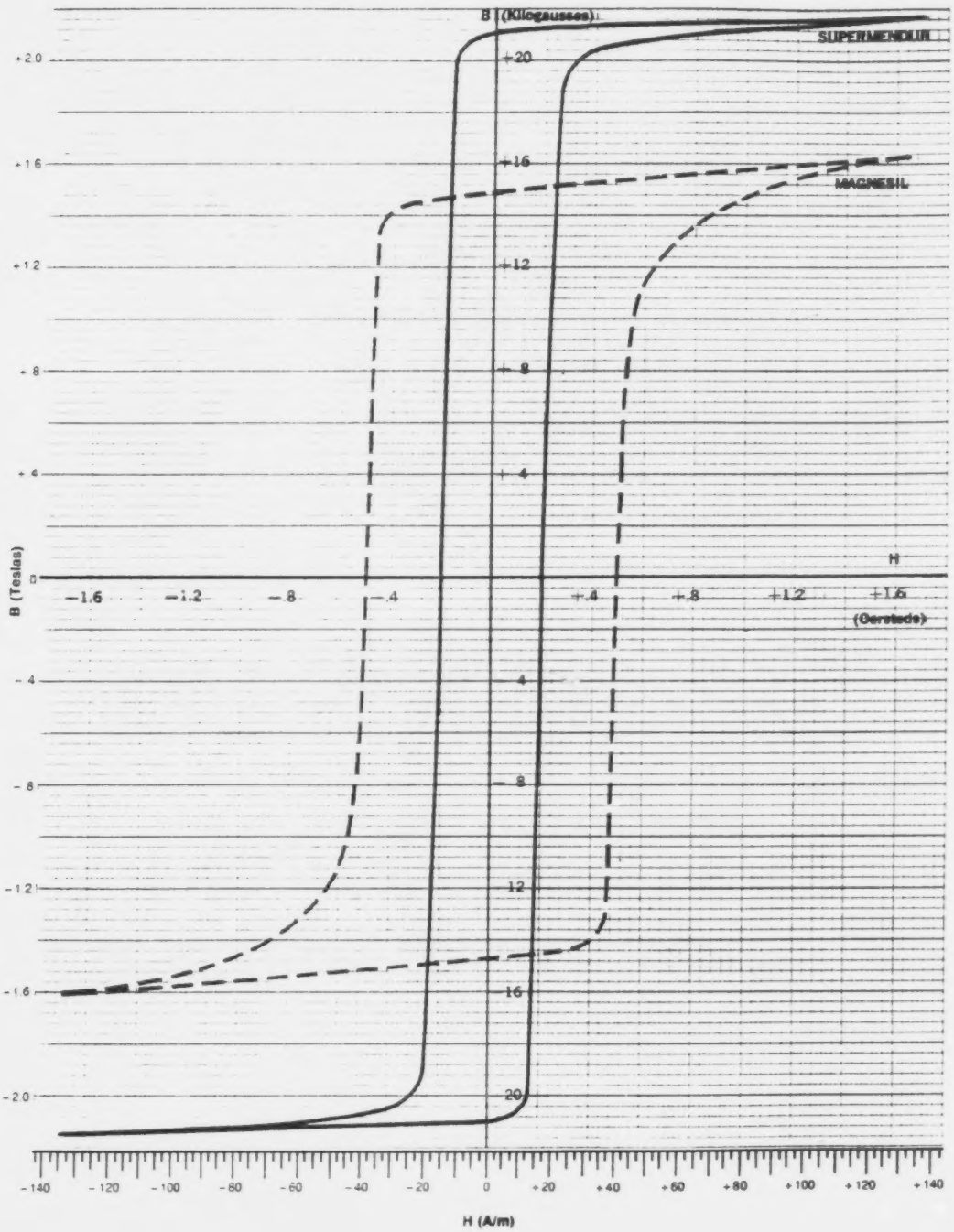

2.1.2. Polynomial and power series

Another popular practice in describing magnetization curves is to use a polynomial approach [24], [30]. Since a curve branch is given by

$$B = f(H) = A_0 + A_1H + A_2H^2 + A_3H^3 + ... + A_NH^N$$

and in the case of central symmetry B(H) = - B(- H) the general expression for the whole curve reduces to an odd powers series:

$$B = f(H) = A_1H + A_3H^3 + ... + A_NH^N$$

Alternatively the curve H = φ(B) can be expressed with the help of a polynomial function:

$$H = K_1B + K_3B^3 + ... + K_NB^N$$

For example, it was shown that the equation

$$H = K_1B + K_{17}B^{17} + K_{21}B^{21},$$

fits very well with the magnetization of iron core [17].

It was also proposed [31] to simulate the magnetization curve with the function

$$H = \Sigma K_iB^{\alpha_i}$$

where α_i is close to 0.5.

Yet another empirical function providing a good fit to the permalloy magnetization curves

$$dB/dH = aH^b$$

was proposed in [33] with coefficients a = 100, b = -2.

2.1.3. Froelich's function

It was found that the iron and transformer steel core B-H characteristics can be satisfactorily represented by a hyperbolic approximation known as Froelich's equation [18], [19]:

$$|B| = |H|/(a+b|H|)$$

However, as was mentioned in [18], this expression must be used carefully since it is valid only slightly beyond the saturation knee. For H values outside the knee this function flattens very quickly and no longer matches the actual magnetization curve.

2.1.4. Arctan and Sinh functions

Some trigonometric functions can be suitable candidates for magnetization curve simulation as they satisfy the requirements of slow growth and central symmetry of two branches

$$B = f(H) = - f(- H).$$

It was shown in [32] that the approximation function

$$B = A_0 \arctan(A_1 H)$$

with $A_0 = 2B_{sat}/\pi$ and $A_1 = 0.5\mu_0\mu_d\pi/B_{sat}$ can be satisfactory for ring and linear permalloy cores used in flux-gate magnetometers.

It was also proposed [29] to express the B-H curve as a hyperbolic function

$$H = A_0 \sinh(A_1 B)$$

2.1.5. Jiles-Atherton model

The work by Jiles and Atherton [23] is among recent very successful attempts to build a model for magnetization curves. The Jiles-Atherton model uses a state equation rather than an explicit function. It is based on existing ideas of domain wall motion, including flexing and translation. This model is used in PSpice simulation software developed by MicroSim Corporation.

The model derives a so called anhysteric (without hysteresis) magnetization curve using a mean field method in which any domain is coupled to the magnetic field (H) and the bulk magnetization (M). This anhysteric value is the magnetization which would be reached in the absence of domain wall pinning.

The equilibrium anhysteric *B-H* curve is modeled by

$$M_{an} = M_S \cdot F(H_e/A)$$

where M_{an} is the anhysteric magnetization

$H_e = H + \alpha \cdot M_{an}$

$F(x) = \coth(x) - 1/x$

and

M_S is the saturation magnetization

A is a thermal energy parameter

α is an interdomain coupling parameter

2.1.6. The choice of magnetization model

There clearly exist two trends in approaching the problem of magnetization curves approximation. The first employs a curve fitting of experimental data making it possible to describe the behavior of some industrial or electronic parts often with high levels of accuracy but with little or no theoretical basis. Alternately, there are models with certain theoretical foundation which may lead to quite elaborate mathematics and often insufficient accuracy in describing real materials.

The nonlinear coil is only a part of the current transducer to be developed and there are other components of the circuit affecting its overall performance. If a particular model employs numerical methods for plotting the magnetization curves, any attempts to describe the transient behavior of this coil as a part of larger circuit will also lead to numerical methods. This would limit the flexibility of assessing the influence of various components. For this reason we shall limit at this time our choice of magnetization models with those which allow the transient analysis to be performed in a general form. In the following sections the transducer circuit is considered from the viewpoints of linear-saturable, general piecewise and polynomial models. These results will then be compared with a SPICE simulation in a version employing the Jiles-Atherton model.

2.2. Linear - saturable magnetization model

To simulate the transient behavior of the coils employing Supermendur® and similar materials such as Supermalloy®, Orthonol®, Magnesil® and Metglas® we shall consider the circuit presented in Fig. 5. It comprises a transformer with driving coil N_1 in series with resistor R_1 and voltage source V_{SRC}, and a measurement coil, N_2 connected to the current source I to be measured. The voltage source V_{SRC} can be switched between V^{+}_{0M} or V^{-}_{0M} or simply be presented as $\pm V_{OM}$ in the case of symmetry. The polarity of V_{SRC} is decided by the circuit processor that will be considered later.

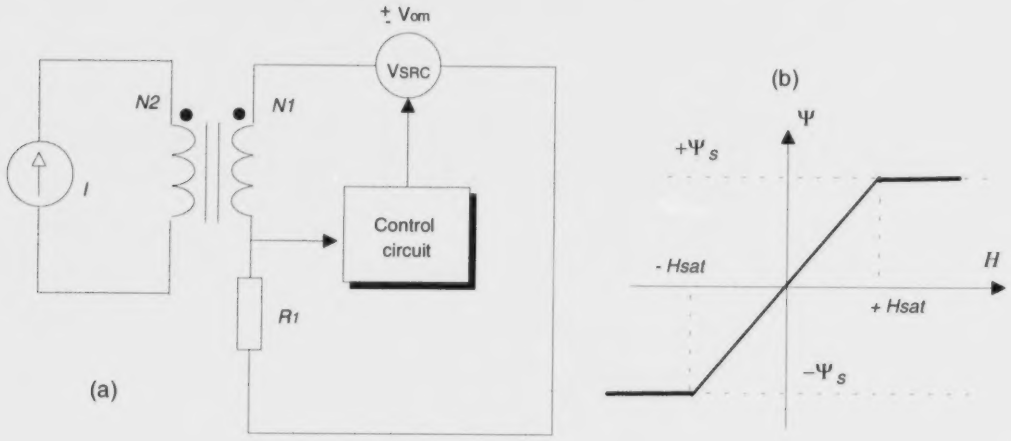

Fig. 5. Linear - saturable model

a) basic multivibrator-type network

b) anhysteretical magnetization characteristic

2.2.1. Anhysteretical linear-saturable model

Fig. 5b shows a simplified magnetization curve of the coil. It is assumed that the core magnetization is linear and symmetrical with saturation levels at ψ_S^+ and ψ_S^-. At this point we neglect the hysteresis. We designate the linear range of magnetic field intensity as $\pm H_{SAT}$. Outside this region the core immediately goes into saturation.

We consider a slowly changing "quasi-dc" input current I in N_2. Let the bipolar current i_L in N_1 be a symmetrical wave and large enough to drive the core into saturation. As a result the core will be switched from saturation level ψ_S^+ to ψ_S^- or vice versa during each half-cycle of i_L (Fig. 6).

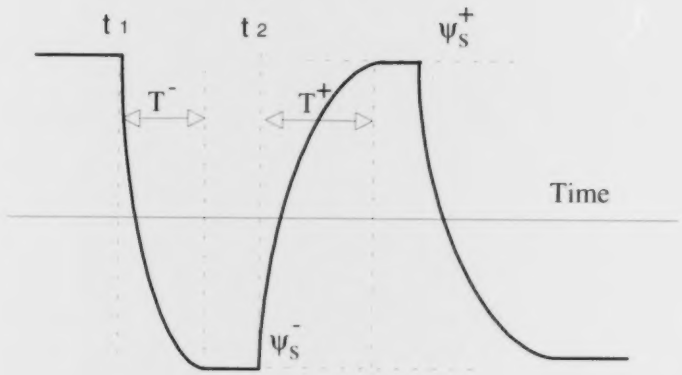

Fig. 6. Flux linkage waveform for linear-saturable coil

Let us calculate the transient time. Namely we are trying to establish how long it will take for the coil in a circuit Fig. 6 to change from one saturation level to another; and how this duration is affected by the input current I. The flux linkage can be found from the expression

$$\frac{d\psi}{dt} + i_L R_1 = V_{SRC} = \begin{cases} V_{OM}^+ \\ V_{OM}^- \end{cases} \qquad (1)$$

Since in the linear region of magnetization, according to Ampere's circuit law the magnetomotive force is

$$F = i_L N_1 + I N_2$$

while flux Φ is linearly proportional to an inductance (L) "seen" by V_{SRC} :

$$\Phi = \psi/N_1 = L\,F\,,$$

the flux linkage can be expressed as

$$\psi = L(i_L + \lambda I) \tag{2}$$

where λ is the coil ratio

$$\lambda = N_2/N_1 \tag{3}$$

Substituting (2) in (1) one obtains

$$\frac{d\psi}{dt} + \frac{\psi}{L}R_1 - \lambda I R_1 = V_{SRC} \tag{4}$$

The solution of (4) yields the general form

$$\psi(t) = L\left(\frac{V_{SRC} + \lambda I R_1}{R_1}\right) + \psi_0 \exp\left(-\frac{R_1}{L}t\right) \tag{5}$$

If we have the change from ψ_S^- to ψ_S^+ then the constant ψ_0 can be obtained from (5) assuming $t = t_2 = 0$ (Fig. 6). At this point the source is switched to V_{0M}^+, the core is still initially saturated with flux linkage ψ_S^-. This gives

$$\psi_0 = \psi_S^- - \frac{L}{R_1}(V_{0M}^+ + \lambda I R_1) \tag{6}$$

This transient process will be finished at $t = T^+$ with the corresponding flux linkage

$$\psi_S^+ = \frac{L}{R_1}(V_{0M}^+ + \lambda I R_1) + [\psi_S^- - \frac{L}{R_1}(V_{0M}^+ + \lambda I R_1)]\exp\left(-\frac{R_1}{L}T^+\right) \tag{7}$$

In a similar manner, for the opposite magnetization transition we can obtain the constant ψ_0 assuming that at $t = t_1 = 0$ when the source is switched to V_{0M}^- the core is saturated at ψ_S^+. This will give

$$\psi_0 = \psi_S^+ - \frac{L}{R_1}(V_{0M}^- + \lambda I R_1) \tag{8}$$

This transition process will be finished at $t = T^-$ with the flux linkage reaching ψ_S^-. Hence

$$\psi_S^- = \frac{L}{R_1}(V_{0M}^- + \lambda I R_1) + [\psi_S^+ - \frac{L}{R_1}(V_{0M}^- + \lambda I R_1)]\exp\left(-\frac{R_1}{L}T^-\right) \tag{9}$$

Expressions (7) and (9) show the influence of the input current I on transient time intervals T^- and T^+. When I = 0 and $-\psi_S^- = \psi_S^+$ it is easy to see that $T^- = T^+$.

Further analysis will be performed for symmetrical saturation flux

$$\psi_S^+ = -\psi_S^- = \psi_S \tag{10}$$

and symmetrical voltage source

$$V_{0M}^+ = -V_{0M}^- = V_{0M} \tag{11}$$

We also introduce $T^+ + T^- = 2T$ and $T^+ - T^- = 2\Delta T$ which results in

$$T^- = T - \Delta T \tag{12}$$

$$T^+ = T + \Delta T \tag{13}$$

where T is an average between transition times T^+ and T^-, and ΔT is the deviation from T occurring in each half-cycle. Equations (7) and (9) can now be rearranged as

$$\psi_S = \frac{L}{R_1}(V_{0M} + \lambda I R_1) + \left[-\psi_S - \frac{L}{R_1}(V_{0M} + \lambda I R_1)\right] \exp\left[-\frac{R_1}{L}(T + \Delta T)\right] \tag{14}$$

$$-\psi_S = \frac{L}{R_1}(-V_{0M} + \lambda I R_1) + \left[\psi_S - \frac{L}{R_1}(-V_{0M} + \lambda I R_1)\right] \exp\left[-\frac{R_1}{L}(T - \Delta T)\right] \tag{15}$$

Equations (14) and (15) yield

$$\Delta T = \frac{L}{2R_1} \ln\left[\frac{(\psi_S + L\lambda I)^2 - \frac{L^2}{R_1^2} V_{0M}^2}{(\psi_S - L\lambda I)^2 - \frac{L^2}{R_1^2} V_{0M}^2}\right] \tag{16}$$

and

$$2T = \frac{L}{R_1} \ln\left[\frac{\left(\psi_S + \frac{L}{R_1} V_{0M}\right)^2 - L^2\lambda^2 I^2}{\left(\psi_S - \frac{L}{R_1} V_{0M}\right)^2 - L^2\lambda^2 I^2}\right] \tag{17}$$

It can be seen from (16) that ΔT is dependent upon the value and polarity of input current. Therefore the circuit behaves as a pulse-width modulator with respect to the current signal originated in the isolated primary loop.

2T is a minimal time required to complete the change from $-\psi_S$ to $+\psi_S$ and back to ψ^-. It can be concluded from (17) that 2T is a polarity independent parabola-like function of the input current. If this pulse-width modulator is to be used as a current sensor, the highest switching frequency of the circuit ensuring its proper operation $f_{max} = 1/2T$ will define the upper limit of the measurement bandwidth. To achieve the highest switching frequency the V_{SRC} must be switched over right at the starting points of saturation.

$$f_{max} = \left[\frac{L}{R_1} \ln \left(\frac{\psi_S + \frac{L}{R_1} V_{0M}}{\psi_S - \frac{L}{R_1} V_{0M}} \right)^2 \right]^{-1} \qquad (18)$$

2.2.2. Linear - saturable coil with hysteresis

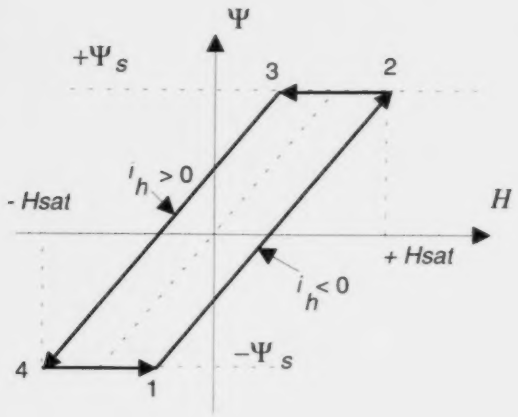

Fig. 7. Linear-saturable magnetization characteristic with hysteresis

We can emulate the effect of magnetic hysteresis by adding a small current source i_h in series with driving current i_L. To ensure that the hysteresis loop is traversed in a counterclockwise direction as presented in Fig. 5 the current source i_h must be positive for region 3-4 and negative for the region 1-2. In both cases i_h is opposite to i_L. Accordingly the magnetic flux inside the linear region of coil operation can be expressed as

$$\psi = L[i_L + \lambda I - \mathrm{sgn}(i_L) i_h] \tag{19}$$

which leads to the following equation

$$\frac{d\psi}{dt} + \frac{\psi}{L} R_1 - \lambda I R_1 - \mathrm{sgn}(i_L) i_h R_1 = V_{SRC} \tag{20}$$

The general solution of (20):

$$\psi(t) = L\left(\frac{V_{SRC} + \lambda I R_1 - \mathrm{sgn}(i_L) i_h R_{11}}{R_1} \right) + \psi_0 \exp(-\frac{R_1}{L} t) \tag{21}$$

yields for symmetrical case

$$\psi_S = \frac{L}{R_1}(V_{0M} + \lambda I R_1 - i_h R_1) + \left[-\psi_S - \frac{L}{R_1}(V_{0M} + \lambda I R_1 - i_h R_1) \right] \exp\left[-\frac{R_1}{L}(T + \Delta T) \right] \tag{22}$$

$$-\psi_S = \frac{L}{R_1}(-V_{0M} + \lambda I R_1 + i_h R_1) + \left[\psi_S - \frac{L}{R_1}(-V_{0M} + \lambda I R_1 + i_h R_1)\right] \exp\left[-\frac{R_1}{L}(T - \Delta T)\right] \quad (23)$$

with expressions for ΔT and $2T$ given below

$$\Delta T = \frac{L}{2R_1} \ln\left[\frac{(\psi_S + L\lambda I)^2 - L^2\left(\frac{V_{0M}}{R_1} - i_h\right)^2}{(\psi_S - L\lambda I)^2 - L^2\left(\frac{V_{0M}}{R_1} - i_h\right)^2}\right] \quad (24)$$

$$2T = \frac{L}{R_1} \ln\left[\frac{\left(\psi_S + \frac{L}{R_1}V_{0M} - Li_h\right)^2 - L^2\lambda^2 I^2}{\left(\psi_S - \frac{L}{R_1}V_{0M} + Li_h\right)^2 - L^2\lambda^2 I^2}\right] \quad (25)$$

It can be concluded from (24) that hysteresis generates a "countercurrent" to the current V_{0M}/R_1 in the driven winding. As a result, to provide the same magnetization effect the current supplied by the driving source V_{SRC} must be increased. This should be considered as a negative factor since it leads to higher power consumption.

2.2.3. Current versus flux control in a current transducer circuit

To implement the circuit idea based on a flux saturation in each semi-period we may recall that

$$V_{coil} = \left.\frac{d\psi}{dt}\right|_{\psi \to \psi_S} \to 0 \quad (26)$$

Accordingly a circuit controlling the polarity of V_{SRC} can be designed as a zero differential comparator with inputs connected to the driving winding N_1. Each time the V_{COIL} falls to zero this comparator will change its state and either switch the V_{SRC} or directly drive the coil provided it has the symmetrical outputs. Another way of providing a feedback control is to measure the current in the coil as a voltage drop across R_1. Here the polarity of V_{SRC} must be switched once this voltage exceeds a certain preset level. This approach was first proposed and studied by Filanovsky and Piskarev for the Schmitt trigger in place of V_{SRC} [16]. For shortness we will refer to

this latter approach as a "current control" as opposed to the prior "flux control" circuit.

2.2.4. Transient current in a linear-saturable coil

Fig. 8 shows the transient current in the coil i_L for positive and negative input current I. When the input current in N_2 is negative (I < 0) even with no driving current in N_1 the flux is also negative, it causes the movement of all magnetization characteristic in the right (positive) direction along the i_L axis. Conversely, when the input current in N_2 is positive (I > 0) the magnetization characteristic is displaced to the left along the i_L axis. As a result the value of the current saturating the coil are no longer equal to I_S but is modulated by the input current I.

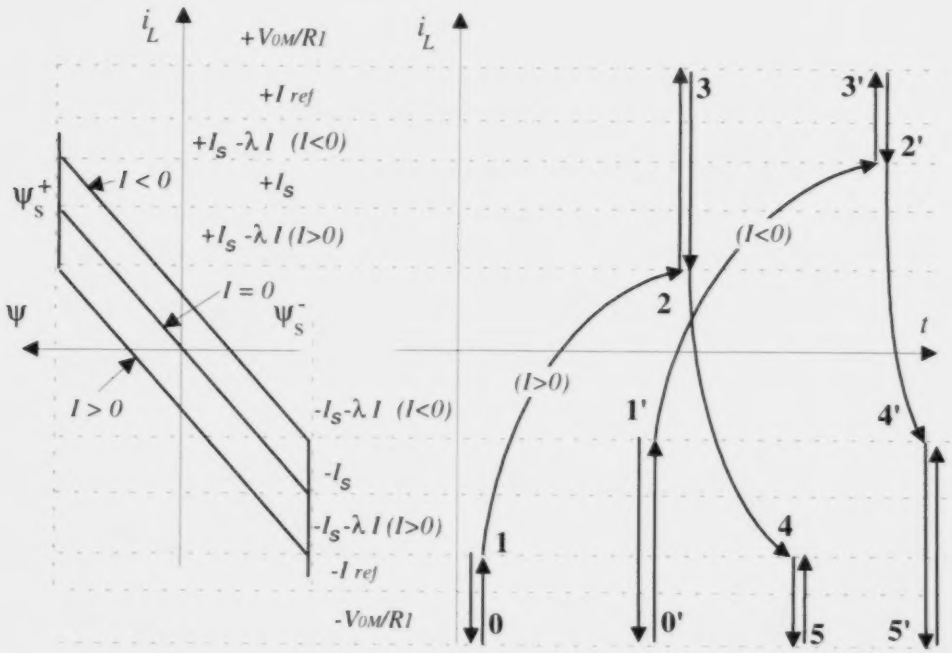

Fig. 8. Current in saturable coil

At the point 0 (or 0') the coil is saturated with negative current $i_L = -V_{0M}/R_1$ which is limited only by resistor R_1. We assume that once the polarity of V_{SRC} has been changed to positive, since no inductance is involved, the transition from 0 to 1 (0' to

1') will take place instantaneously. For the region 1-2 (1'-2') the conventional equation for the coil in series with a resistor

$$L\frac{di_L}{dt}+i_L R_1 = V_{SRC} \tag{27}$$

yields the following solution for duration T^+ :

$$T^+ = \frac{L}{R_1}\ln\frac{V_{0M}+I_S R_1+\lambda I R_1}{V_{0M}-I_S R_1+\lambda I R_1} \tag{28}$$

Right after reaching the point of saturation 2(2') the coil inductance falls to zero and the current instantly increases to V_{0M}/R_1 residing at the point 3(3'). Since the reference level has been crossed the control circuit will switch the polarity of V_{SRC} to negative. This change immediately pulls the current i_L back to 2(2'). The next transition from 2(2') to 4(4') embraces an interval

$$T^- = \frac{L}{R_1}\ln\frac{V_{0M}+I_S R_1-\lambda I R_1}{V_{0M}-I_S R_1-\lambda I R_1} \tag{29}$$

After arriving at the point of saturation 4(4') the current instantaneously falls to $-V_{0M}/R_1$ which is the point 5(5') in Fig. 8. Subsequently the polarity of V_{SRC} changes again to positive and the whole transient cycle starts again.

The difference between positive (from 0 to 3) and negative transition (from 3 to 5)

$$T^+ - T^- = \Delta T = \frac{L}{R_1}\ln\left[\frac{V_{0M}^2-(I_S R_1+\lambda I R_1)^2}{V_{0M}^2-(I_S R_1-\lambda I R_1)^2}\right] \tag{30}$$

is described by essentially the same equation as (16) obtained earlier for a flux-control circuit which can be checked after substituting ψ_S by Li_S.

2.2.5. Reference levels

Two reference levels in the multivibrator based current transducer define the points where the polarity of V_{SRC} is switched over. Comparison of the displaced magnetization curves for $I = 0$, $I > 0$, $I < 0$ in Fig. 9 shows that they contain identical central segments (shown in bold) between $Is - \lambda|I_{max}|$ and $-(Is - \lambda|I_{max}|)$. Since these central segments have the same slope, integration of the equation (27) in the indicated limits will yield the same ΔT for all three characteristics. It means that if the

reference levels were chosen inside the above region the transducer would be insensitive to the input current.

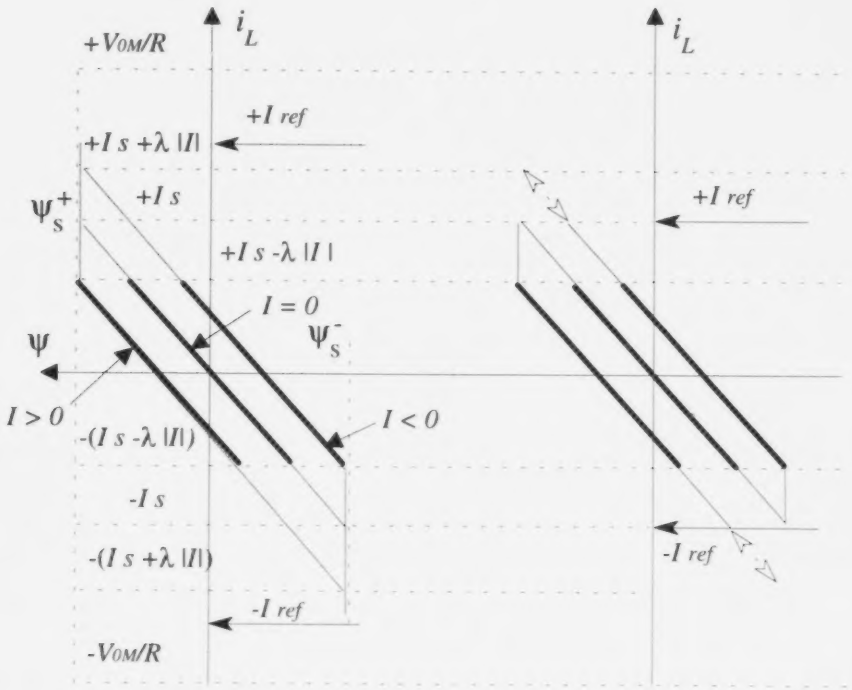

Fig. 9. Definition of the reference levels

The question arises as to how the reference points must be chosen outside the above dead region to provide the maximal sensitivity of the transducer. Two cases shown in Fig. 9 lead us to an assumption that the reference levels must be set in the regions corresponding to the coil's complete saturation:

$$+ I_{REF} > + I_S + \lambda \left| I_{max} \right| \text{ and } - I_{REF} < - I_S - \lambda \left| I_{max} \right|$$

Indeed comparing characteristics given in Fig. 9 we note that the second case for which the reference levels $\pm I_{REF}$ are set equal to the saturation levels $\pm I_S$:

$$+ I_{REF} = + I_S, - I_{REF} = - I_S$$

excludes the two otherwise active segments (shown with double arrows). The output characteristic corresponding to the second case is described by

$$T^+ - T^- = \Delta T = \frac{L}{R} \ln \left[\frac{V_{0M}^2 - (I_S R)^2}{V_{0M}^2 - (I_S R - \lambda I R)^2} \right] \qquad (31)$$

for $I > 0$ and

$$T^{+} - T^{-} = \Delta T = \frac{L}{R} \ln\left[\frac{V_{0M}^2 - (I_S R + \lambda I R)^2}{V_{0M}^2 - (I_S R)^2}\right] \tag{32}$$

for $I < 0$. It can be shown that (31) and (32) relate to the transducer operation with much less sensitivity than (30). Obviously making I_{REF} smaller than I_S will truncate the characteristics along with sensitivity even more.

It should be noted that the reference levels must not exceed the current set by the limiting resistor: $\pm V_{0M}/R_1$. In addition the input current must be limited to the value defined as

$$|I_{max}| < V_{0M}/(\lambda R_1) - I_s/\lambda \tag{33}$$

Performance of the current transducer as a function of reference levels is summarized in Fig. 10.

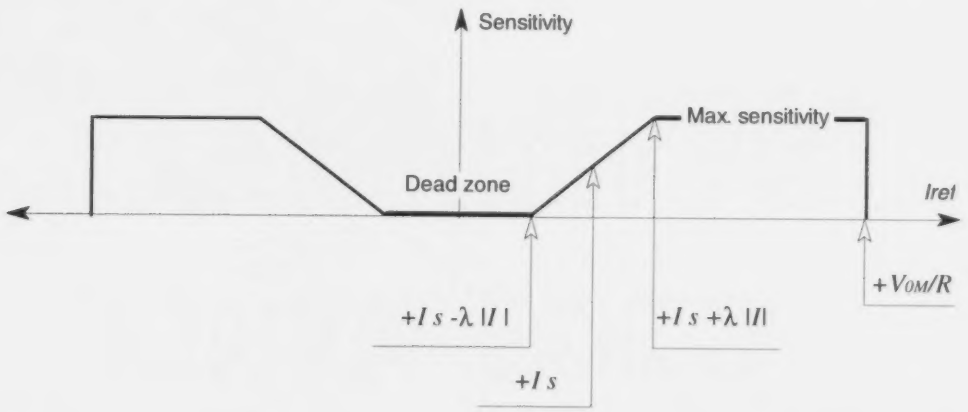

Fig. 10. Sensitivity of the current transducer for different I_{REF} settings

2.2.6. Calculated transient characteristics for linear-saturable model

We can use equations (16), (18), (24), (25) to obtain ΔT and f_{max} versus input current characteristics for any particular coils and core materials provided their magnetization curves satisfy the linear-saturable model. As an example we can perform design

calculations based on a circuit Fig. 11 for two core materials - amorphous core 2826MB [10] and the earlier described Supermendur [27].

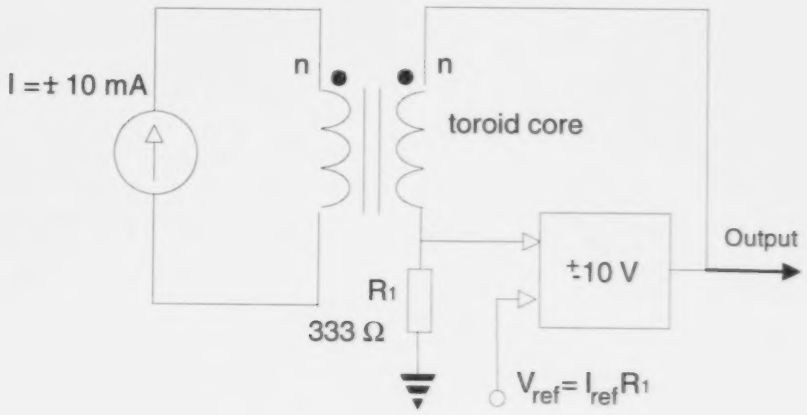

Fig. 11. Circuit used for sample calculation

In order to demonstrate how the above materials affect the circuit performance we choose R_1, toroid size, driving and saturation currents equal for both cases (Table 1).

Table 1

Initial data		
Core type (material)	2826MB	Supermendur
B_{sat}, T	0.835	2.1
H_{sat}, A/m	1	5
Crossection A_e, m^2	2.25E-05	2.25E-05
Magnetic path, l_e, m	0.0955	0.0955
Calculated parameters		
Number of turns, $n = N_1 = N_2$	10	50
Saturation flux , $F_{sat} = B_{sat}A_e$, W	1.88E-05	4.72E-05
Saturation flux linkage $\psi_{sat} = nF_{sat}$, V*s	0.000188	0.002358
$i_{sat} = H_{sat}l_e/n$, A	0.00955	0.00955
$L = \psi_{sat}/i_{sat}$, H	0.019638	0.246942
V_{0M}, V	10	10
I_{max}, A	0.01	0.01
$R_1 < V_{0M}/(I_{sat} + I_{max})$, Ω	333	333

Calculated ΔT and f characteristics are plotted in Fig. 12, 13, 14.

Fig. 12. Calculated characteristic of the current sensor with 2826MB amorphous core transformer ($N_1 = N_2 = 10$, $L = 20$ mH, $i_s = 10$ mA)

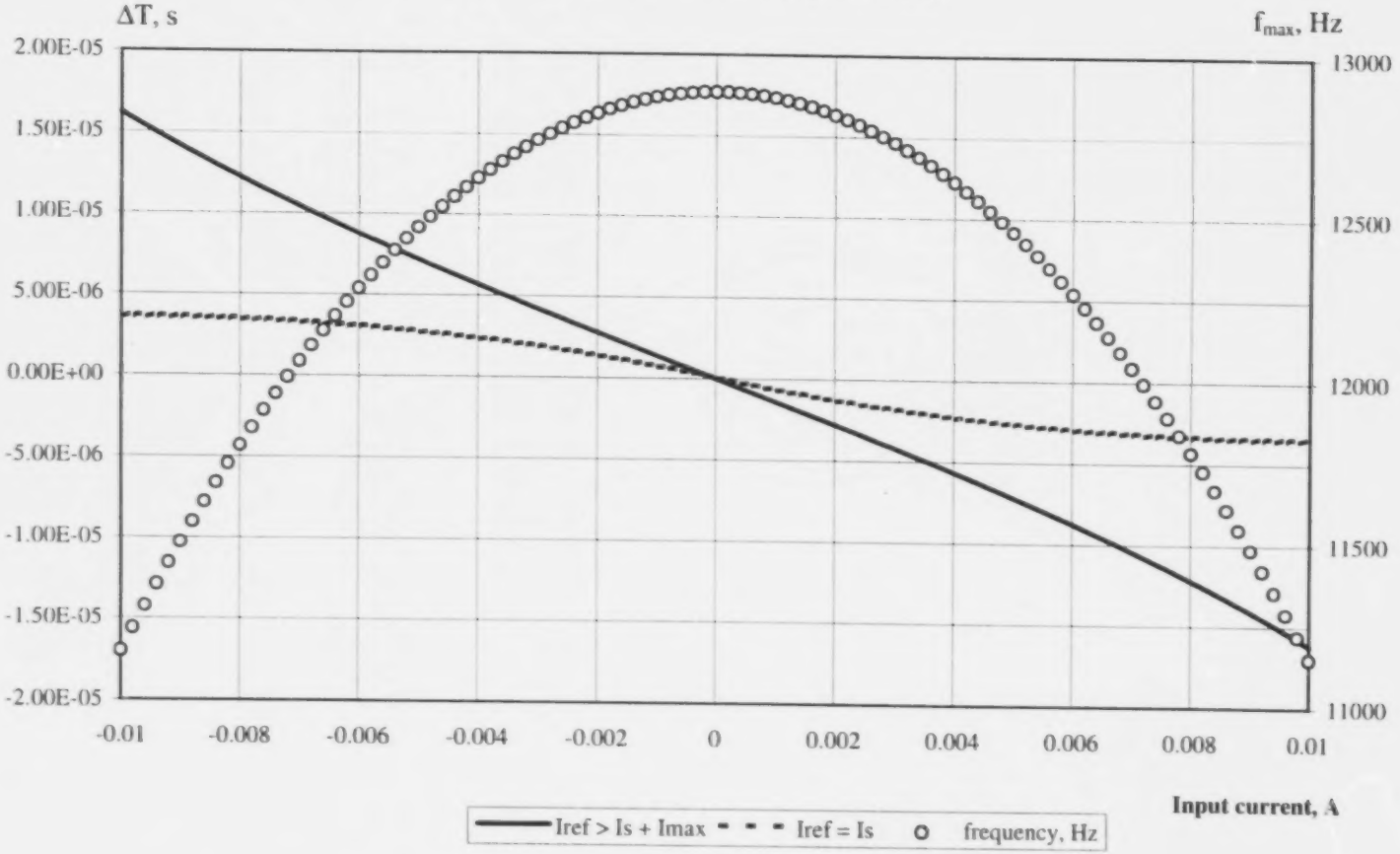

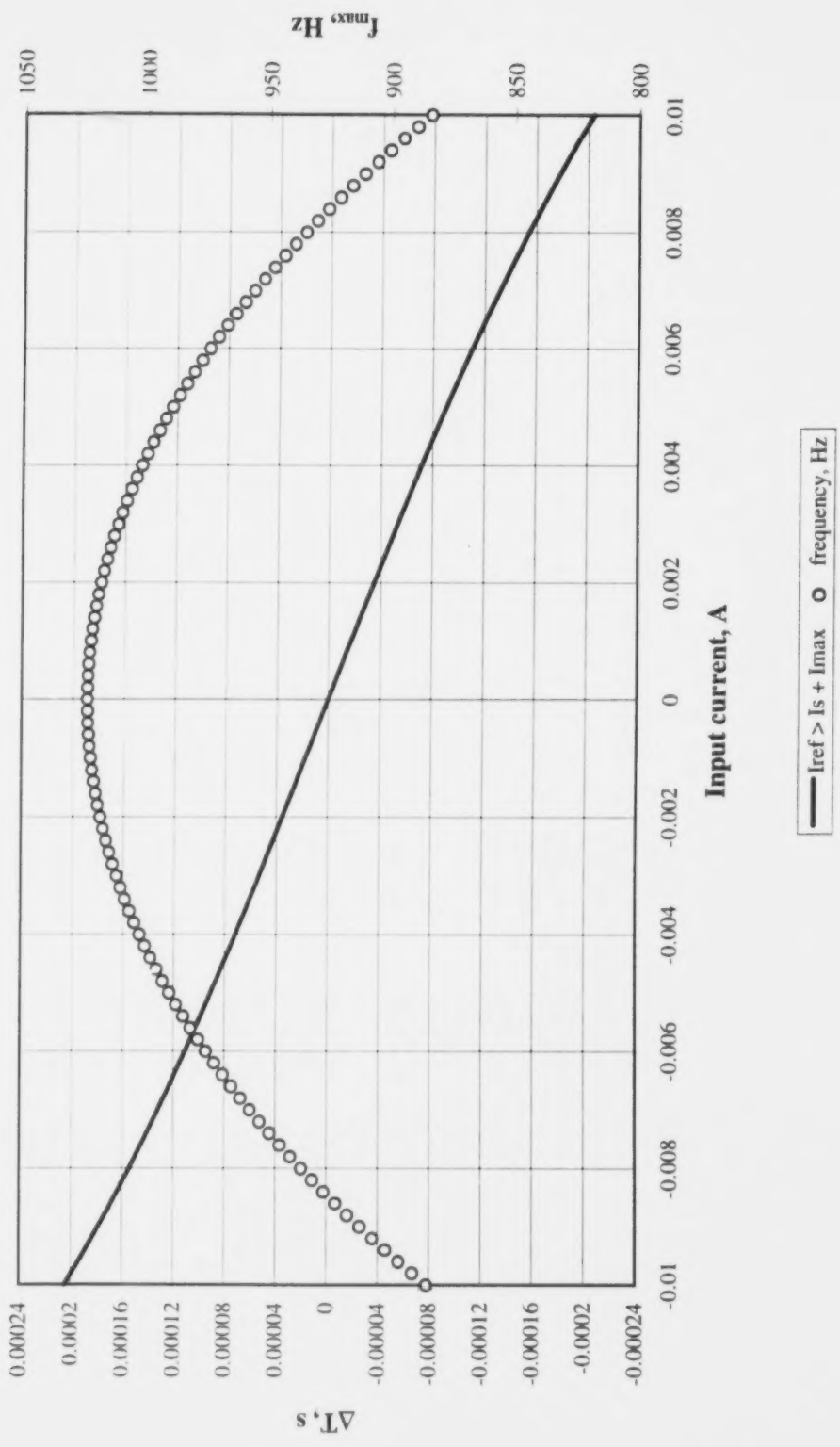

Fig. 13. Calculated characteristics of the current sensor with Supermendur core transformer ($N_1 = N_2 = 50$, $L = 0.25$ H, $i_s = 10$ mA)

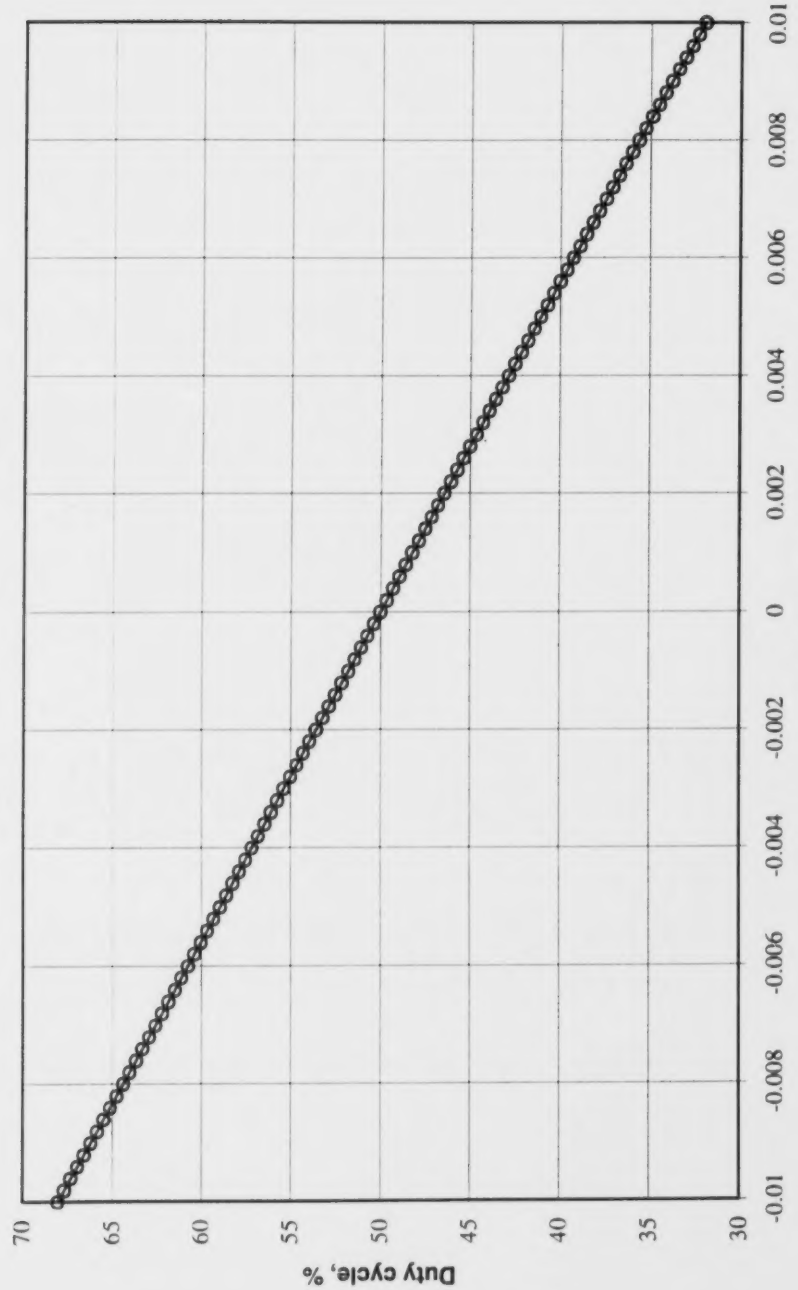

Fig. 14. Calculated duty cycle of the current sensor output signal for 2826MB and Supermendur core transformers

2.3. Piecewise linear approximation

Let us expand the circuit analysis to include the core materials whose B-H characteristics are not linear 'enough' to fit the linear-saturable model. For such cases it is appropriate to introduce additional linear segments which can reflect the real picture more accurately. In this section we shall discuss the piecewise linear simulation with an arbitrary number of sections, a general approach which can be used for any type of nonlinear magnetization curves.

In addition we are particularly interested in finding how the smoothed transition from the linear to saturation region may affect the sensor sensitivity. The effect of smoothing is observed for all known magnetic materials including special alloys such as Square Permalloy 80®, Magnesil® and Supermendur® whose squareness factor exceeds 90%. It is important in design practice to assess the errors introduced when a realistic magnetization curve is simulated by the linear-saturable model.

2.3.1. Transient analysis

We consider a magnetization curve with two symmetrical branches deviated from the linear-saturable characteristic. Each branch of the curve depicted in Fig. 15 comprises N linear sections with successively decelerating slopes. For example, the n-th section confined between ψ_{n-1} and ψ_n has a lesser slope than the (n-1)-th section between ψ_{n-2} and ψ_{n-1}. For the branch in the third quadrant we choose negative (-n) notation to stress the symmetry, therefore the (-n)-th section is situated between $-\psi_{n-1}$ and $-\psi_n$. The last N-th sections of each branch reach the saturation levels ψ_s and $-\psi_s$ accordingly.

When a coil with the shown in Fig. 15 ψ versus i_L characteristic becomes a part of the multivibrator circuit the magnetic flux during every oscillation cycle changes from ψ_s to $-\psi_s$ and back to ψ_s. Consequently each of the shown linear sections is responsible for its own portion of transient time spent in both directions. That allows us to

introduce the time difference ΔT_n associated with each linear segment separately (see Fig. 16) as opposed to the global pulse-width difference observed for the complete oscillation cycle.

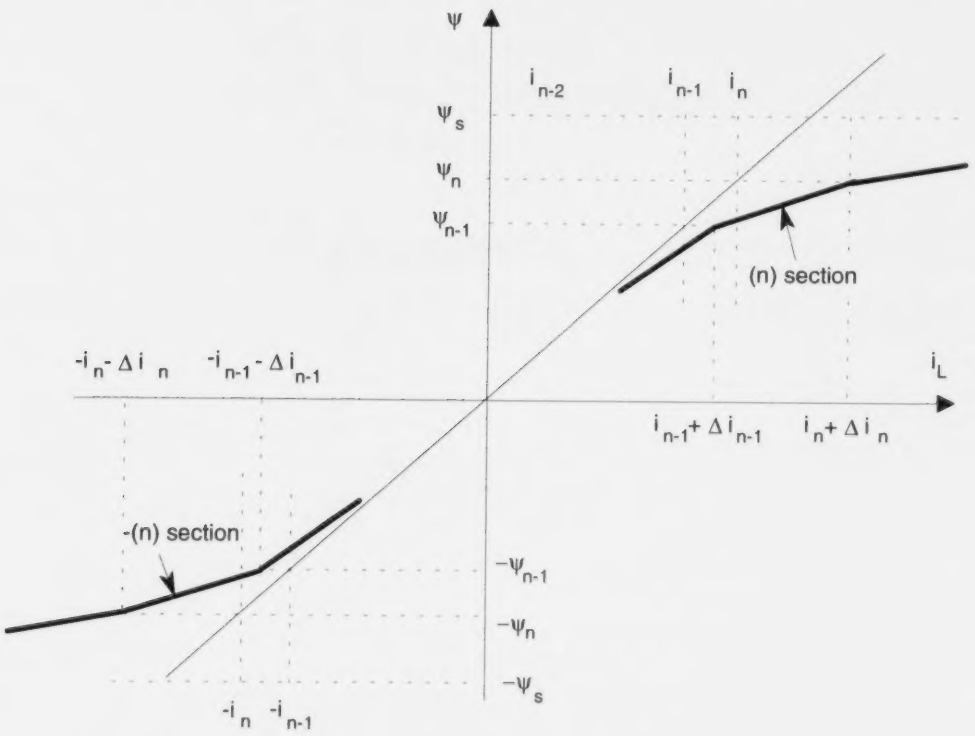

Fig. 15. Piecewise linear representation of a magnetization curve

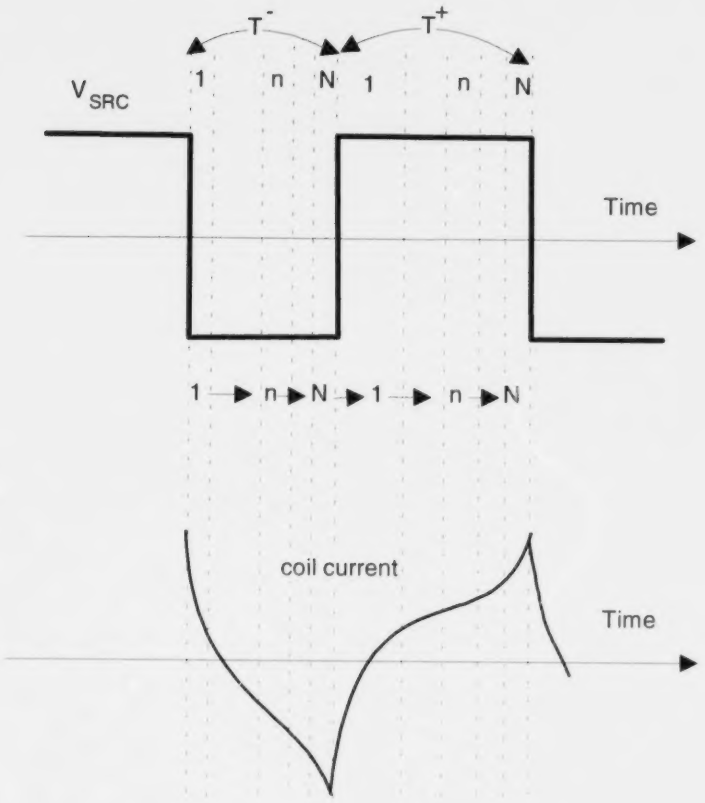

Fig. 16. Discrete presentation of the RL-multivibrator waveforms

In our analysis we group the effect of opposite sections (n) and (-n) of the N-section characteristic such that the global measured pulse-width deviation will be a sum of their corresponding partial differences. Recalling that ΔT is 50% of the difference between "+" and "-" transient time intervals we can write

$$\Delta T = \frac{1}{2}\sum_{n=1}^{N}\left(T_n^+ + T_{-n}^+ - T_n^- - T_{-n}^-\right) \tag{34}$$

Here T_n^+ is the time interval needed to reach the point ψ_n, starting from ψ_{n-1},

T_{-n}^+ - time interval between $-\psi_{n-1}$ and $-\psi_n$,

T_n^- - time interval between ψ_n and ψ_{n-1},

T_{-n}^- - time interval between $-\psi_n$ and $-\psi_{n-1}$,

Solving the equation (27) for the n-th section we obtain

$$T_n^+ = \frac{L_n}{R_1} \ln\left(\frac{i_{n-1} + \Delta i_{n-1} - \lambda I - I_{0M}}{i_n + \Delta i_n - \lambda I - I_{0M}}\right) \tag{35}$$

$$T_n^- = \frac{L_n}{R_1} \ln\left(\frac{i_n + \Delta i_n - \lambda I + I_{0M}}{i_{n-1} + \Delta i_{n-1} - \lambda I + I_{0M}}\right) \tag{36}$$

Since the inductance of the symmetrical section (-n) as "seen" by the source V_{SRC} is equal to the one of the (n) section $L_n = L_{-n}$ we obtain

$$T_{-n}^+ = \frac{L_n}{R_1} \ln\left(\frac{i_n + \Delta i_n + \lambda I + I_{0M}}{i_{n-1} + \Delta i_{n-1} + \lambda I + I_{0M}}\right) \tag{37}$$

$$T_{-n}^- = \frac{L_n}{R_1} \ln\left(\frac{i_{n-1} + \Delta i_{n-1} + \lambda I - I_{0M}}{i_n + \Delta i_n + \lambda I - I_{0M}}\right) \tag{38}$$

Finally, we express the global pulse-width deviation as a sum of constituents corresponding to (n) and (-n) segment pairs.

$$\Delta T = \sum_{n=1}^{n=N} \frac{\psi_n - \psi_{n-1}}{2\left(i_n + \Delta i_n - i_{n-1} - \Delta i_{n-1}\right) R_1} \ln\left\{\frac{\left[\left(i_n + \Delta i_n + \lambda I\right)^2 - I_{0M}^2\right] \times \left[\left(i_{n-1} + \Delta i_{n-1} - \lambda I\right)^2 - I_{0M}^2\right]}{\left[\left(i_n + \Delta i_n - \lambda I\right)^2 - I_{0M}^2\right] \times \left[\left(i_{n-1} + \Delta i_{n-1} + \lambda I\right)^2 - I_{0M}^2\right]}\right\} \tag{39}$$

Equation (39) is a general form allowing us to obtain and analyze practically any type of magnetization characteristics. For example, for the linear-saturable model (sections -2, -1, 1, 2 in Fig. 17) we obtain

$$\Delta T_{-2,-1,1,2} = \frac{L_1}{2R_1} \ln\left[\frac{\left(i_1 + \lambda I\right)^2 - I_{0M}^2}{\left(i_1 - \lambda I\right)^2 - I_{0M}^2}\right] + \frac{L_1}{2R_1} \ln\left\{\frac{\left[\left(i_{s1} + \lambda I\right)^2 - I_{0M}^2\right] \times \left[\left(i_1 - \lambda I\right)^2 - I_{0M}^2\right]}{\left[\left(i_{s1} - \lambda I\right)^2 - I_{0M}^2\right] \times \left[\left(i_1 + \lambda I\right)^2 - I_{0M}^2\right]}\right\} \tag{40}$$

which can be reduced to the form obtained previously for the linear-saturable model:

$$\Delta T = \Delta T_{-n} + \Delta T_n = \frac{L_1}{2R_1} \ln\left[\frac{\left(i_{s1} + \lambda I\right)^2 - I_{0M}^2}{\left(i_{s1} - \lambda I\right)^2 - I_{0M}^2}\right] \qquad \circ \tag{41}$$

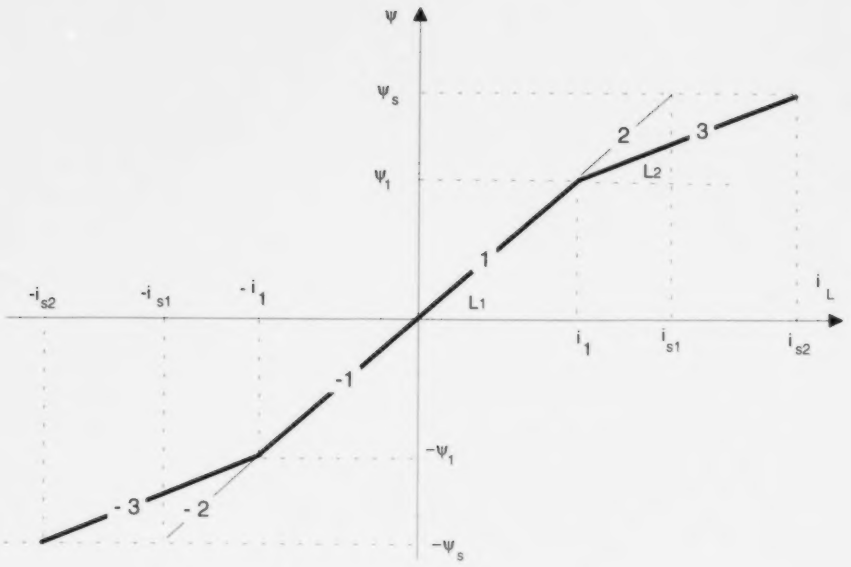

Fig. 17. Three-section magnetization model

Let us consider the case of a rectangular characteristic which is inclined in the near saturation region. Since even very sharp magnetization curves are slightly smoothed in the vicinity of saturation we are interested in assessing the errors introduced when a realistic curve is simulated by the linear-saturable model. The global pulse-width deviation for three-section characteristic -3, -1, 1, 3 presented in Fig. 17 is

$$\Delta T_{-3,-1,1,3} = \frac{L_1}{2R_1}\ln\left[\frac{(i_1+\lambda I)^2 - I_{0M}^2}{(i_1-\lambda I)^2 - I_{0M}^2}\right] + \frac{L_2}{2R_1}\ln\left\{\frac{\left[(i_{s2}+\lambda I)^2 - I_{0M}^2\right]\times\left[(i_1-\lambda I)^2 - I_{0M}^2\right]}{\left[(i_{s2}-\lambda I)^2 - I_{0M}^2\right]\times\left[(i_1+\lambda I)^2 - I_{0M}^2\right]}\right\} \quad (42)$$

where saturation current

$$i_{s2} = i_1 + \frac{L_1}{L_2}(i_{s1} - i_1) \quad (43)$$

The sections -1, 1 are the same for both characteristics and obviously result in the same pulse-width difference, as opposed to sections 3 and -3 which are inclined from 2 and -2 and can bring different ΔT. This observation can be generalized, in a sense, that in order to compare different types of magnetization curves we only need to trace the influence of nonshared sections.

2.3.2. Calculation example

Using the specifications for Supermendur® [27] given in Table 1 it is possible to perform a sample calculation of the output pulse width deviation ΔT. In Fig. 18 the calculated sensor characteristic is presented for input current 5 mA and -5 mA and two types of approximation models. First is the linear-saturable model which presumes that the curve is linear and runs into saturation immediately once the current exceeds i_{S1}. For given data i_{S1} = 10 mA. Inductance associated with this model is L_1 = 247 mH. The second approximation is a three-section model containing two additional sections starting at $\pm i_1$ (i_1 = 9 mA). Calculations were performed with respect to the apparent inductance L_2 of these additional sections varying from 8 to 100% of L_1. References to both models can be found in Fig. 17.

Results show that the characteristic with smooth transition from linear region to saturation provides somewhat greater sensitivity than the linear-saturable model. However, this difference is not significant for the global ΔT since it is observed only for $L_2/L_1 < 0.1$.

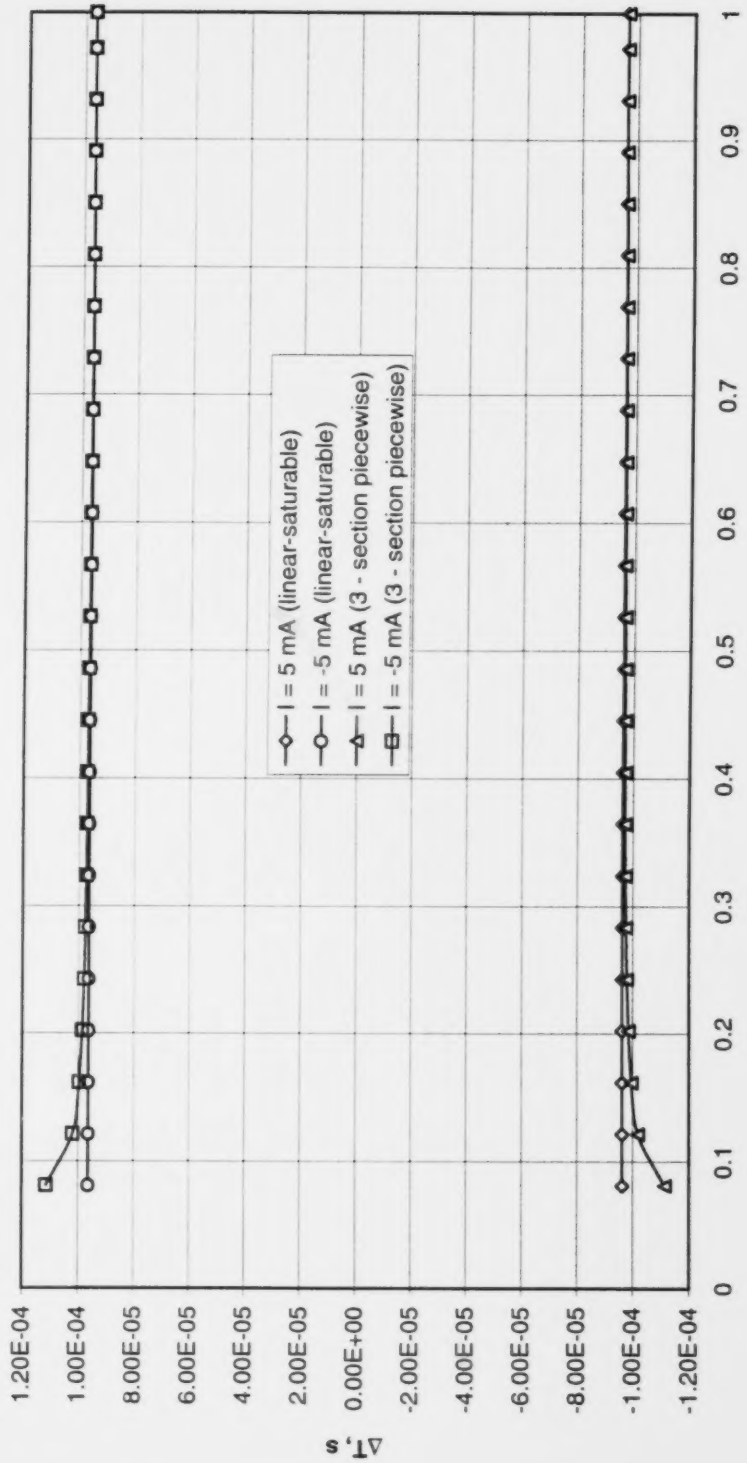

Fig. 18. Comparison of the linear-saturable and three-section piecewise model for the Supermendur core

2.3.3. Magnetization loops distortion

It was assumed throughout all previous discussions that the magnetization loop can be displaced along the current axis but not distorted from its form obtained for I = 0. This condition is valid only if the flux reaches a complete saturation in each oscillation cycle. Careful design of the circuit and proper choice of the core material must ensure this requirement is met.

However, for some types of magnetic materials the complete saturation point may far exceed the operating range of the current transducer. Among possible practical reasons for this are core power dissipation limitations or maximum current of the winding. As a result, when the saturation of the flux is not reached we recognize the "undersaturated" current transducer mode, presented in Fig. 19.

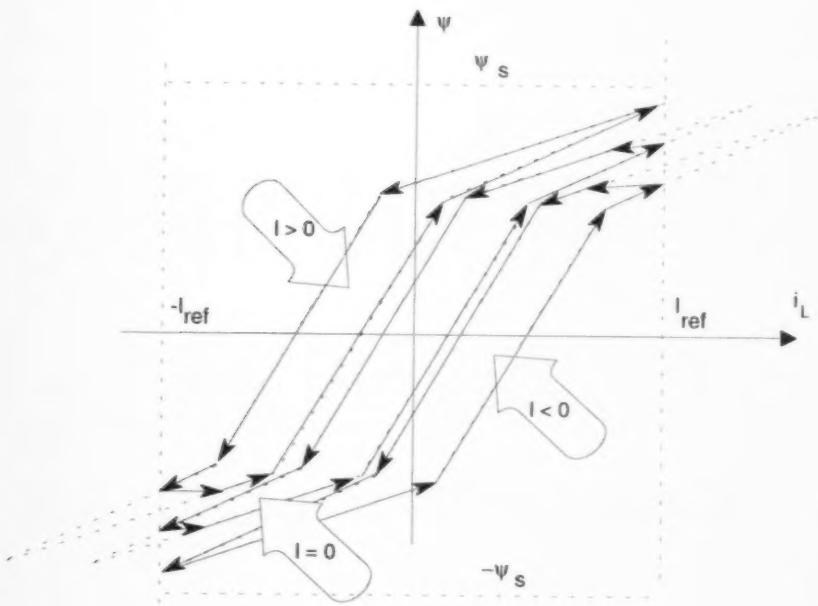

Fig. 19. Undersaturated current transducer mode

In the undersaturated mode the magnetization loop not only moves along the i_L axis but also distorts when the input current I increases or changes polarity. If the upper and lower current limits are predefined, the loop distortion, as shown in Fig. 20a, results from the effect of truncation of those sections which have been moved beyond the $\pm I_{ref}$ range. For this reason this type of distortion is typical for circuits where the multivibrator is controlled by the current reference levels.

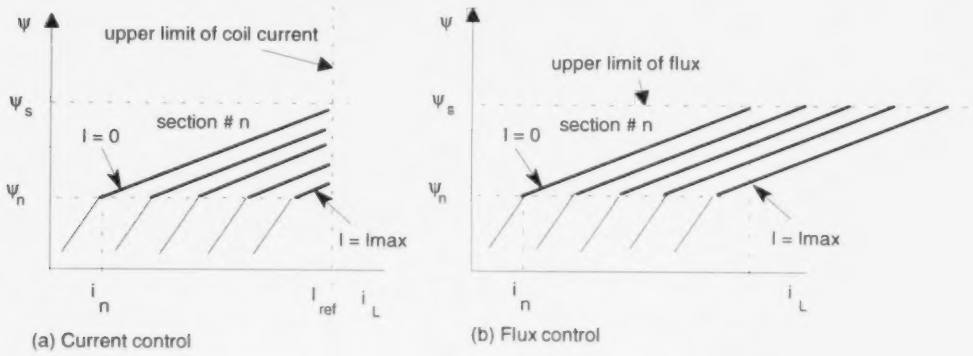

Fig. 20. Displacement of the magnetization curve n-th section
(a) for current control circuits
(b) flux control circuits

Because the n-th section length is inversely proportional to the input current we can express the pulse-width deviation of this section as

$$\Delta T_n = \frac{L_n}{R} \ln\left[\frac{\left(i_n - \lambda I\right)^2 - I_{0M}^2}{\left(I_{ref} - \lambda I\right)^2 - I_{0M}^2}\right] \simeq \frac{L_n}{R} \ln\left\{\frac{\left(i_n - \lambda I\right)^2 - I_{0M}^2}{\left[I_s\left(1 - \frac{I}{I_{MAX}}\right) + i_n - \lambda I\right]^2 - I_{0M}^2}\right\} \tag{44}$$

It follows from (44) that when the n-th section is truncated, the portion of sensitivity introduced by this section into the global transducer response is also decreased.

Fig. 20b presents the n-th section displacement for the flux controlled multivibrator. In this case the distortion does not occur since a maximum current in each oscillation cycle changes along with the loop displacement.

2.3.4. ΔT offset and hysteresis errors

From the equations (24), (41) it follows that a loop hysteresis or loop distortion (due to the above considered truncation) can influence only the linearity and sensitivity of the transducer output characteristic, but can not cause the hysteresis. Of course, in a practical design due to the slightly different V_{SRC} values for positive and negative polarity, or the difference in the reference levels, the magnetization loop can become asymmetrical even for I = 0. This will result in an offset error of ΔT. However, as long as magnetization characteristics are repeatable for the same input current this offset error will be also repeatable, in other words, systematic. Hysteresis of ΔT will not appear.

Still there exists one more source of zero error, namely, a residual "memory" of the ferromagnetic material associated with relatively large applied input dc current. The effect of this "memory" is confirmed by many studies dealing with magnetic amplifiers and second harmonic modulators [10], [32]. Although there exists some knowledge gap in respect to the quantitative evaluation of this factor some of the assumed "behavioral" characteristics relevant to the current transducer will be outlined below.

It is known that after applying a dc mmf which is then returned to zero the corresponding flux density can be displaced. This is widely known as a remanent magnetization of the material. This remanence factor can still appear to some extent when the ac demagnetizing mmf (such as driving current in N_1) is applied to the core along with dc mmf. Despite the efforts of ac mmf to drive the core around the major magnetization loop (Fig. 21), the loop can take a slightly displaced position with

respect to the origin of coordinates. The reason for this is insufficient demagnetizing mmf and non-uniform internal saturation of magnetic domains. Since the global magnetization characteristic is no more than a combination of partial characteristics associated with each of the magnetic domains some portion of them may stay undersaturated when the ac mmf is insufficient.

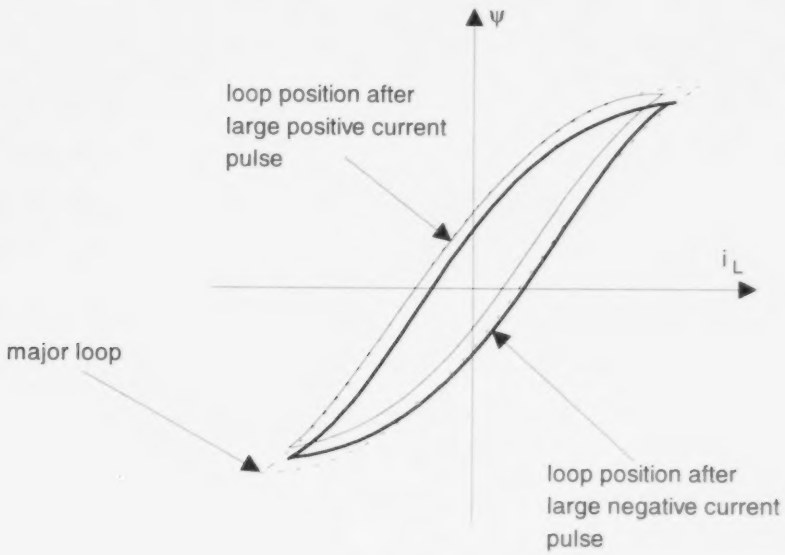

Fig. 21. Magnetization loop displacement "memory"

As a consequence, when the input current approaches zero after being at its high positive or negative level the loop can still be slightly displaced in a direction corresponding to its most recent polarity (Fig. 21). Therefore, depending upon the history of applied current, the ΔT which is a product of loop position may take in the vicinity of zero, not one, but many different positive or negative values. As a countermeasure to resulting hysteresis in the output transducer characteristic the driving current should be chosen sufficiently large to provide the compulsory saturation of all magnetic domains in each and every oscillation cycle.

2.4. Polynomial approximation

2.4.1. Transient analysis

The magnetization characteristic of a nonlinear coil can be approximated by an odd power series [16]. Recalling (1):

$$\frac{d\psi}{dt} + i_L R_1 = V_{SRC}$$

and substituting the flux linkage with a third order series

$$\psi_L = Li_L - ai_L^3 \tag{45}$$

we obtain

$$L\frac{di_L}{dt} - 3a(i_L + \lambda I)^2 \frac{di_L}{dt} = V_{0M} - i_L R_1 \tag{46}$$

Here λ is a turn ratio

$$\lambda = \frac{N_1}{N_2} \tag{47}$$

We consider the circuit with a Schmitt trigger shown in Fig. 2 where

$$I_{0M} = \frac{V_{0M}}{R_1} \tag{48}$$

is the maximal current in the coil and

$$\rho = \frac{R_3}{R_2 + R_3} \tag{49}$$

is the comparator hysteresis parameter.

Fig. 22 presents transient waveforms typical for polynomial approximation.

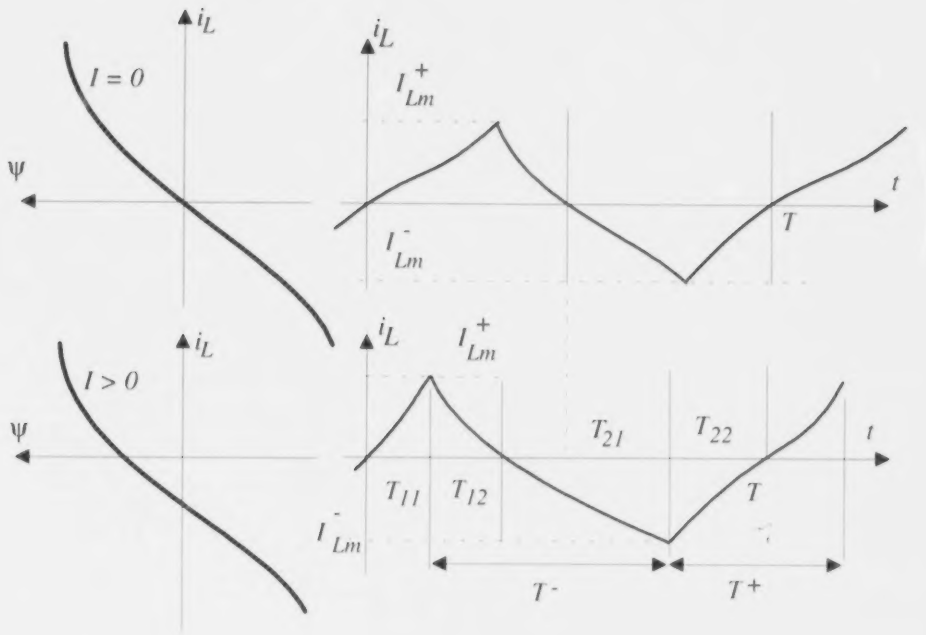

Fig. 22. Waveforms of the coil current for polynomial model

Integrating (46) one can obtain

$$T_{11} = \int_0^{I_{Lm}^+} \frac{\left[L - 3a\left(i_L + I\lambda\right)^2\right] di_L}{V_{0M}^+ - i_L R_1} \tag{50}$$

which yields for a symmetrical voltage source

$$T_{11} = \frac{L - 3aI^2\lambda^2 - 6aII_{0M}\lambda - 3aI_{0M}^2}{R_1} \ln\left(\frac{1}{1-\rho}\right) + \frac{3aI_{0M}^2\rho^2}{2R_1} + \frac{3a\left(2I\lambda + I_{0M}\right)I_{0M}\rho}{R_1} \tag{51}$$

Analogously

$$T_{12} = -\frac{L - 3aI^2\lambda^2 + 6aII_{0M}\lambda - 3aI_{0M}^2}{R_1} \ln\left(\frac{1}{1+\rho}\right) - \frac{3aI_{0M}^2\rho^2}{2R_1} + \frac{3a\left(-2I\lambda + I_{0M}\right)I_{0M}\rho}{R_1} \tag{52}$$

$$T_{21}=\frac{L-3aI^2\lambda^2+6aII_{0M}\lambda-3aI_{0M}^2}{R_1}\ln\left(\frac{1}{1-\rho}\right)+\frac{3aI_{0M}^2\rho^2}{2R_1}+\frac{3a\left(-2I\lambda+I_{0M}\right)I_{0M}\rho}{R_1} \tag{53}$$

$$T_{22}=-\frac{L-3aI^2\lambda^2-6aII_{0M}\lambda-3aI_{0M}^2}{R_1}\ln\left(\frac{1}{1+\rho}\right)-\frac{3aI_{0M}^2\rho^2}{2R_1}+\frac{3a\left(2I\lambda+I_{0M}\right)I_{0M}\rho}{R_1} \tag{54}$$

After substitution with

$$K_1=\frac{3a\lambda^2}{R_1},\ K_2=\frac{6aI_{0M}\lambda}{R_1},\ K_3=\frac{3aI_{0M}^2}{R_1}$$

we obtain

$$T_{11}=\left(\frac{L}{R_1}-K_1I^2-K_2I-K_3\right)\ln\left(\frac{1}{1-\rho}\right)+\frac{\rho^2}{2}K_3+K_2\rho I+K_3\rho \tag{55}$$

$$T_{12}=\left(\frac{L}{R_1}-K_1I^2+K_2I-K_3\right)\ln(1+\rho)-\frac{\rho^2}{2}K_3-K_2\rho I+K_3\rho \tag{56}$$

$$T_{21}=\left(\frac{L}{R_1}-K_1I^2+K_2I-K_3\right)\ln\left(\frac{1}{1-\rho}\right)+\frac{\rho^2}{2}K_3-K_2\rho I+K_3\rho \tag{57}$$

$$T_{22}=\left(\frac{L}{R_1}-K_1I^2-K_2I-K_3\right)\ln(1+\rho)-\frac{\rho^2}{2}K_3-K_2\rho I+K_3\rho \tag{58}$$

2.4.2. Formatting of the output signal

Although each of the transient components T_{11}, T_{12}, T_{21}, T_{22} is a function of the input current I they all contain dc offset and I^2 constituents. Therefore it is preferable to combine the above components in a way that would eliminate or minimize these sources of nonlinearity. The following combinations were found to be optimal since they appear free from offset and I^2 constituents.

$$Y_1=T_{11}-T_{21}=\frac{12aI_{0M}\lambda}{R_1}\left[\rho+\ln(1-\rho)\right]I \tag{59}$$

$$Y_2=T_{12}-T_{22}=\frac{12aI_{0M}\lambda}{R_1}\left[\ln(1+\rho)-\rho\right]I \tag{60}$$

$$Y_3=T_1-T_2=T_{11}+T_{12}-T_{21}-T_{22}=\frac{12aI_{0M}\lambda}{R_1}\left[\ln(1-\rho^2)\right]I \tag{61}$$

$$Y_4=T^+-T^-=T_{11}+T_{22}-T_{12}-T_{21}=\frac{12aI_{0M}\lambda}{R_1}\left[2\rho-\ln\left(\frac{1+\rho}{1-\rho}\right)\right]I \tag{62}$$

The question arises as to which of above expressions would provide the highest sensitivity. The sensitivity S_M

$$S_M = \frac{Y_m}{I} \tag{63}$$

of output signals Y_m (59)-(62) was calculated for the same value of ρ. Fig. 23 presents the results which state that the maximal sensitivity will be achieved for the output signal formatted as $Y_3 = T_1 - T_2$. The second highest sensitivity is demonstrated for $Y_1 = T_{11} - T_{21}$ followed by $Y_4 = T^+ - T^-$. The output characteristic $Y_3 = T_1 - T_2$ calculated for transformer with L = 2.63 mH, a = 0.3 V s A^{-3}, $\lambda = 0.5$ [15] is shown in Fig. 24.

The sensitivity increases with higher values of ρ while the frequency of the output signal presented in Fig. 25, 26

$$f = \frac{R_1}{2\left(L - 3a\lambda^2 I^2 - 3aI_{0M}^2\right)\ln\left(\frac{1+\rho}{1-\rho}\right) + 6aI_{0M}^2\rho} \tag{64}$$

decreases. It means that the optimal choice of ρ should be looked at as a tradeoff between achievable sensitivity and bandwidth.

It is interesting to note that the frequency in the polynomial model slightly increases with the growth of input current while the piecewise simulation presumes the opposite. One can use this fact when deciding which model is more applicable to specific experimental data.

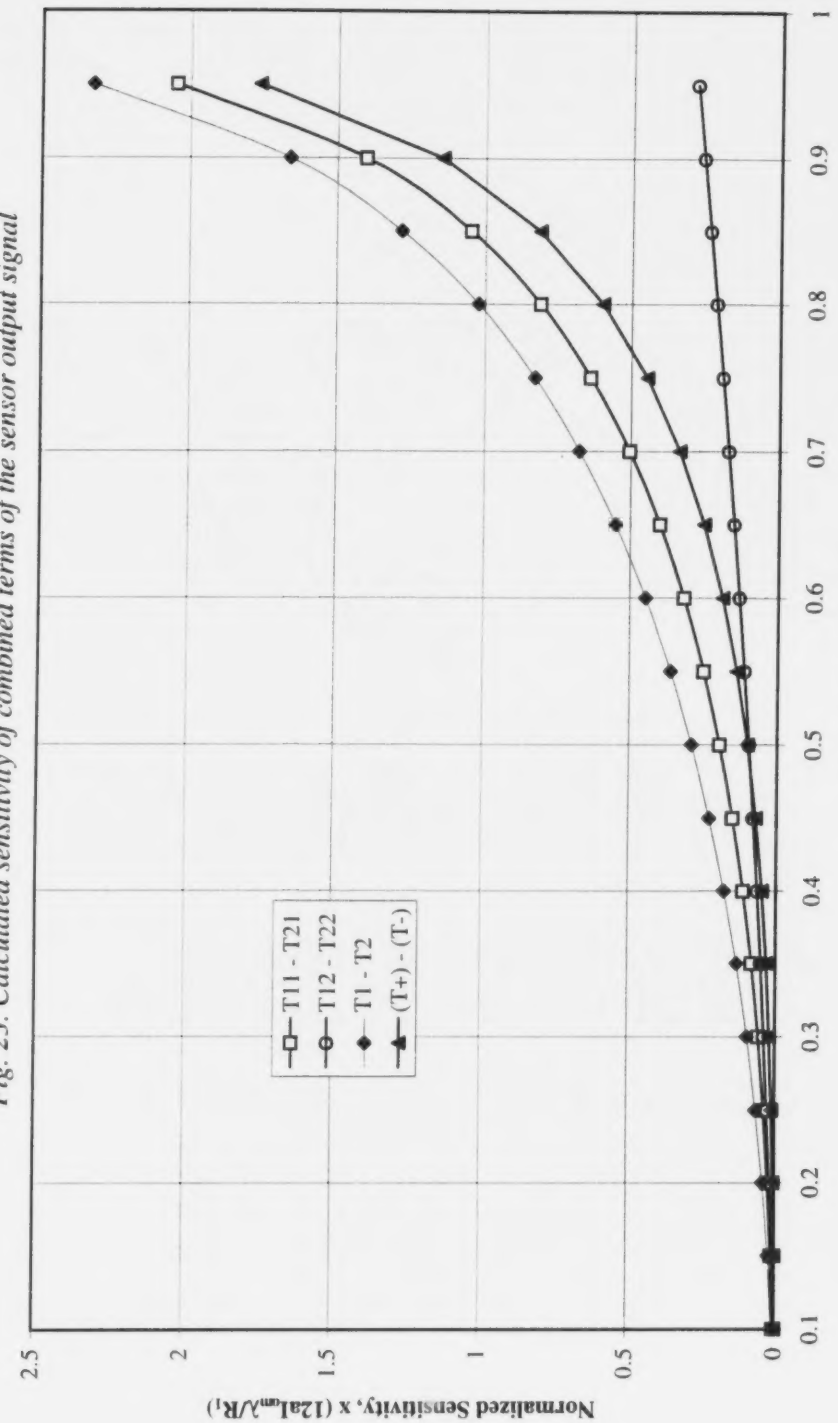

Fig. 23. Calculated sensitivity of combined terms of the sensor output signal

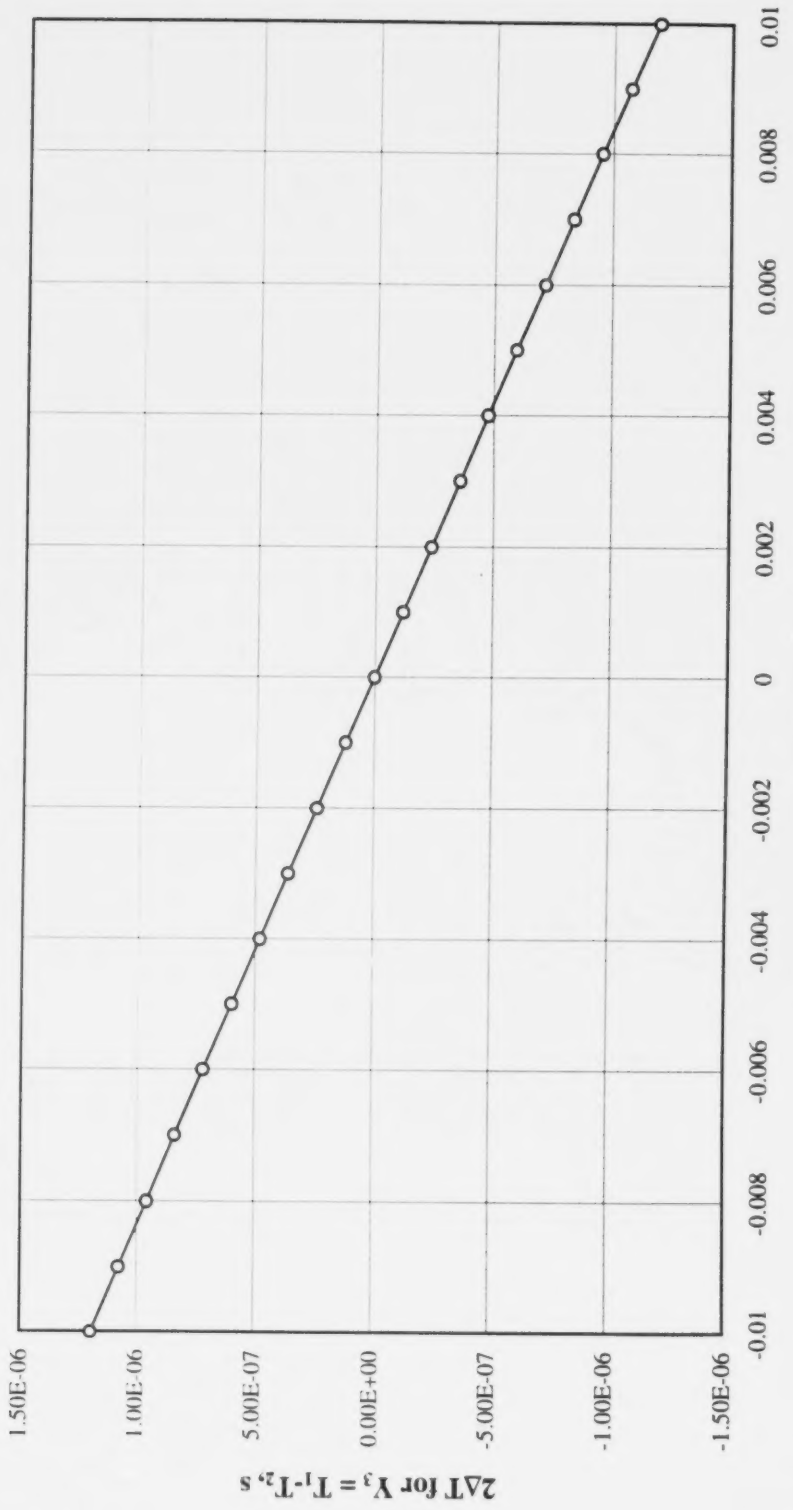

Fig. 24. Calculated sensor output characteristic Y_3
(L = 2.6 mH, a = 0.3, ρ = 0.9, N_1/N_2 = 0.5, I_{0M} = 20 mA)

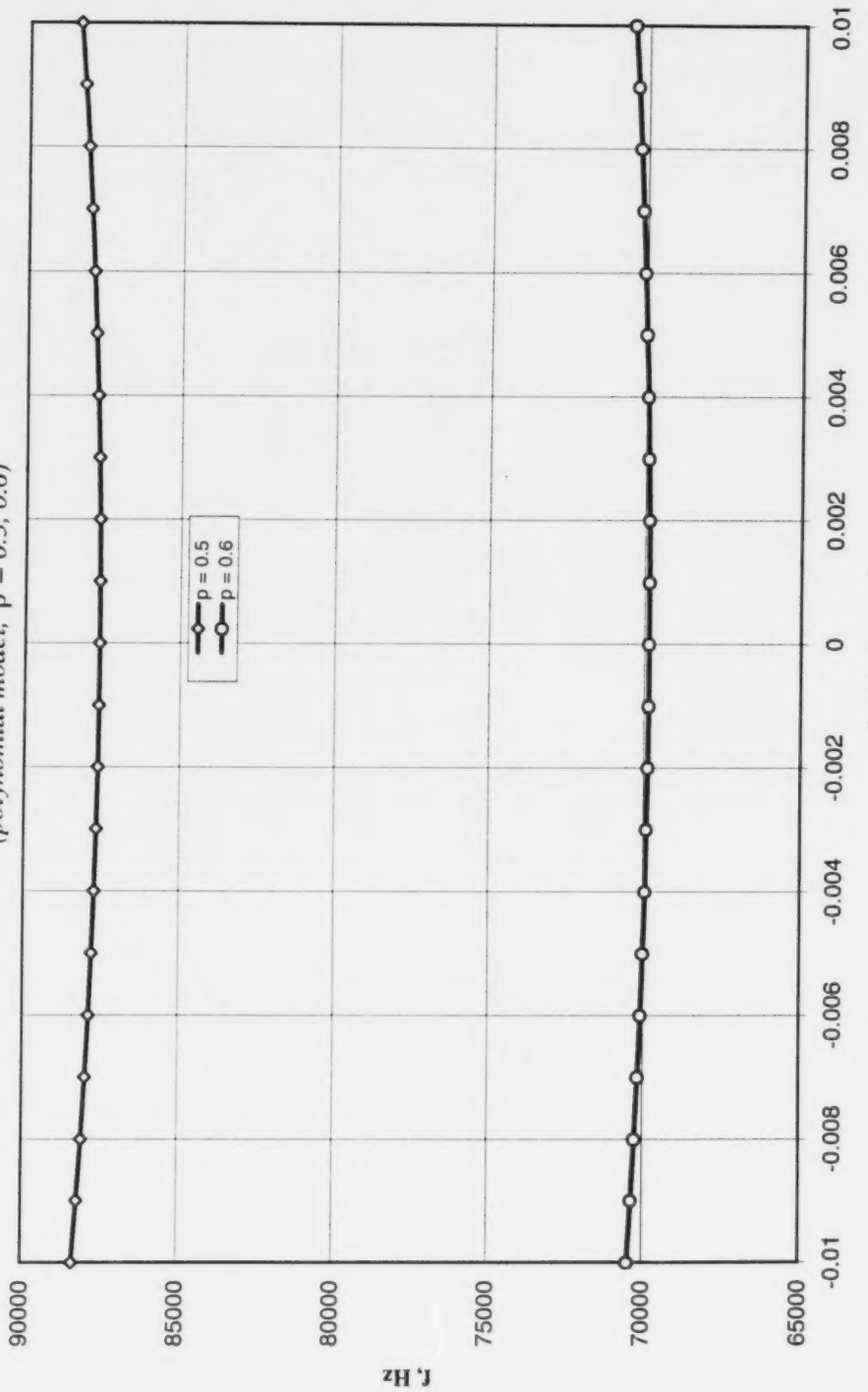

Fig. 25. Calculated output signal frequency as a function of input current (polynomial model, ρ = 0.5, 0.6)

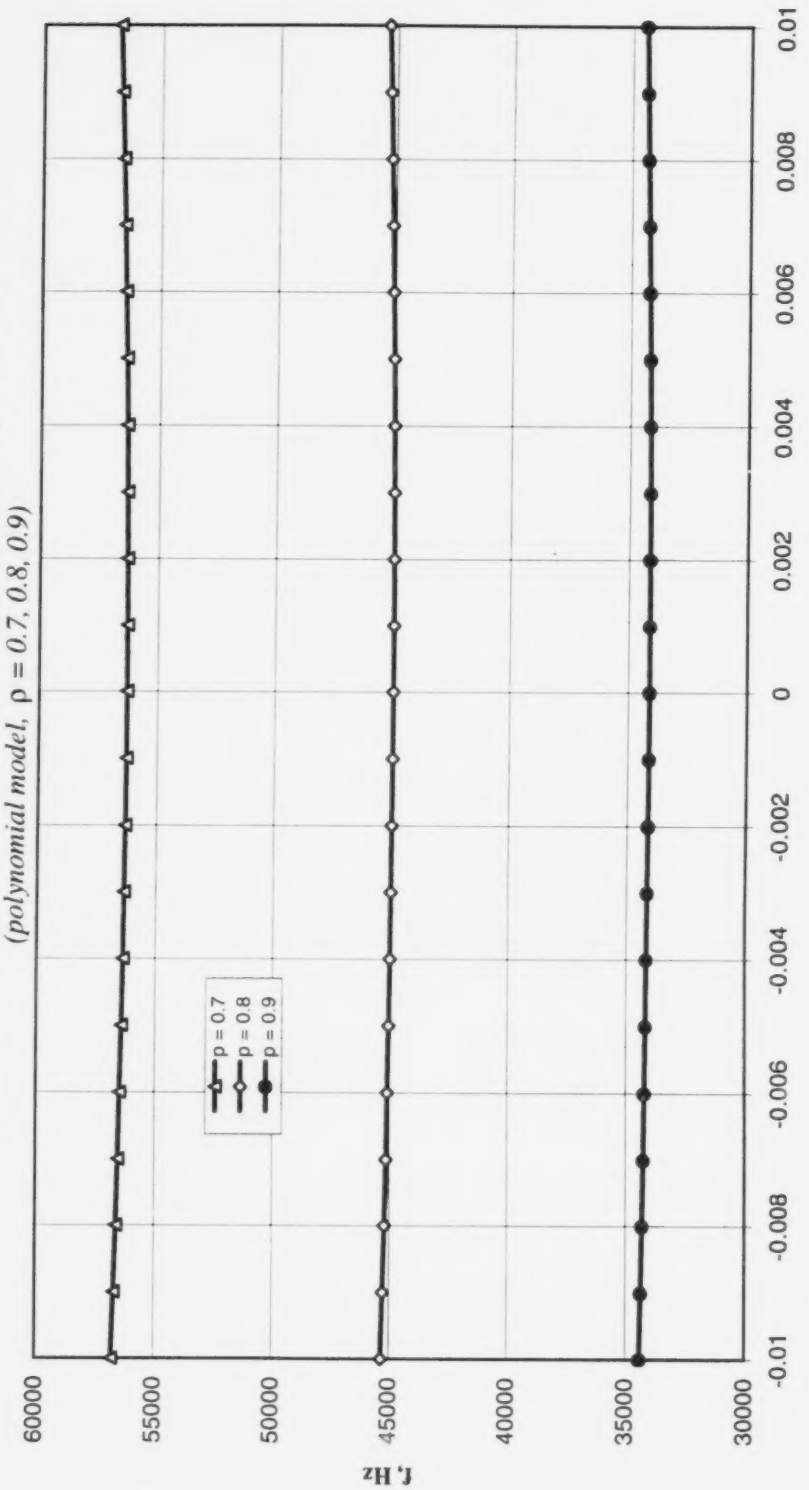

Fig. 26. Calculated output signal frequency as a function of input current (polynomial model, ρ = 0.7, 0.8, 0.9)

2.4.3. Application limits of the polynomial model

Observing results obtained for the polynomial model one may conclude that the output characteristic does not have a dead zone. This yields the fact that the dead zone results from the linear section of the B-H curve while the latter is never formally linear from the polynomial model viewpoint. Yet, for the vast majority of magnetic materials a transition between two opposite saturation limits will inevitably include the region of the B-H curve which is very close to linear. To reflect the presence of this pseudo-linear region the values of parameters used in the polynomial model must be chosen accordingly. As a result the sensor sensitivity no matter which model is used, will have the same dead zone pattern.

Limitations of the polynomial model do not follow from the model itself but rather depend on the realistic B-H curve this model attempts to replace. Using this model there appears some freedom in setting the current reference limits I_{REF} below or above I_S. In general the model would not require a complete coil saturation. This may be convenient for magnetic cores with less "square" magnetization loops. For example, this model can be utilized for applications where the choice of magnetic core is limited, such as high current measurements.

Nonetheless we must recognize that the polynomial model of the third order is much more restricted in respect to realistic magnetization data than the piecewise model. For some loops it would be very difficult to use the polynomial model without applying strong approximation limits. It means likewise that the permissible range of a loop displacement along the i_L axis should be coherent with the limits of a model's validity.

2.5. SPICE simulation

2.5.1. Circuit and simulation data

The circuit of a nonlinear magnetic multivibrator was simulated with PSpice 6.0 (MicroSim Corp.) using internal software library components. The multivibrator presented in Fig. 27 consists of a nonlinear transformer TX1 (core K3019PL_3C8-X) with two windings ($N_1 = N2 = 200$) and a feedback operational amplifier in a Schmitt trigger mode (μA741). To conform to the core requirements the trigger uses an output current booster (complimentary pair 2N3904 and 2N3906). The hysteresis parameter ρ defined by R_4, R_3 is set at 0.44.

Charts with calculated timing diagrams and magnetization curves for the input dc current source I at +200 mA, -200 mA and ac current source 200 mA are presented in Fig. 28-32. The output file is included in Appendix 1.

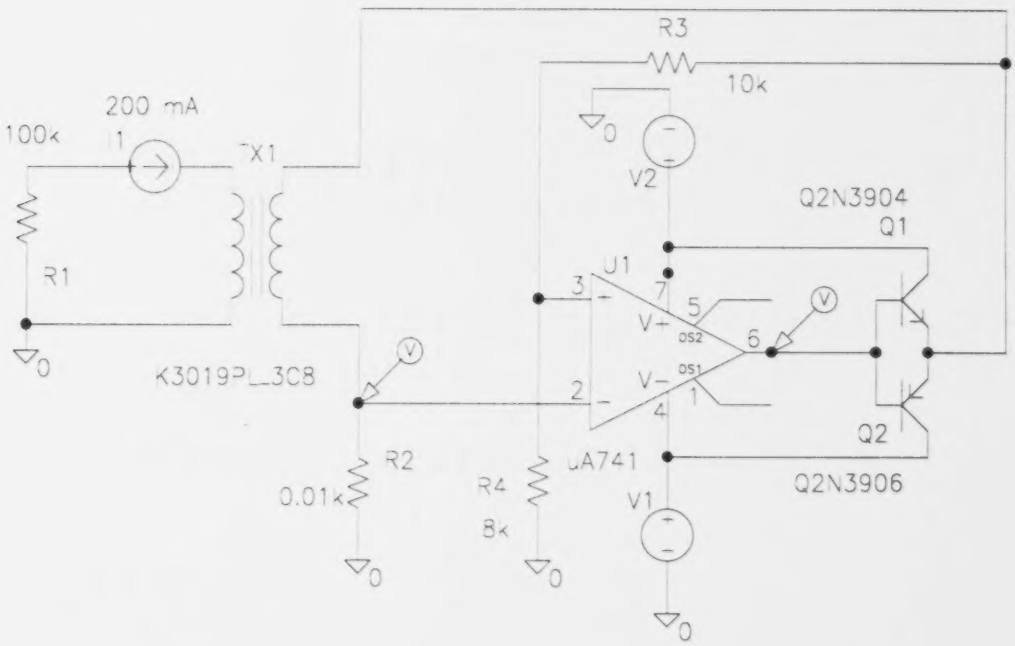

Fig. 27. PSpice schematics

Fig. 28. Simulated waveforms of coil current and Schmitt trigger output for input current -200 mA

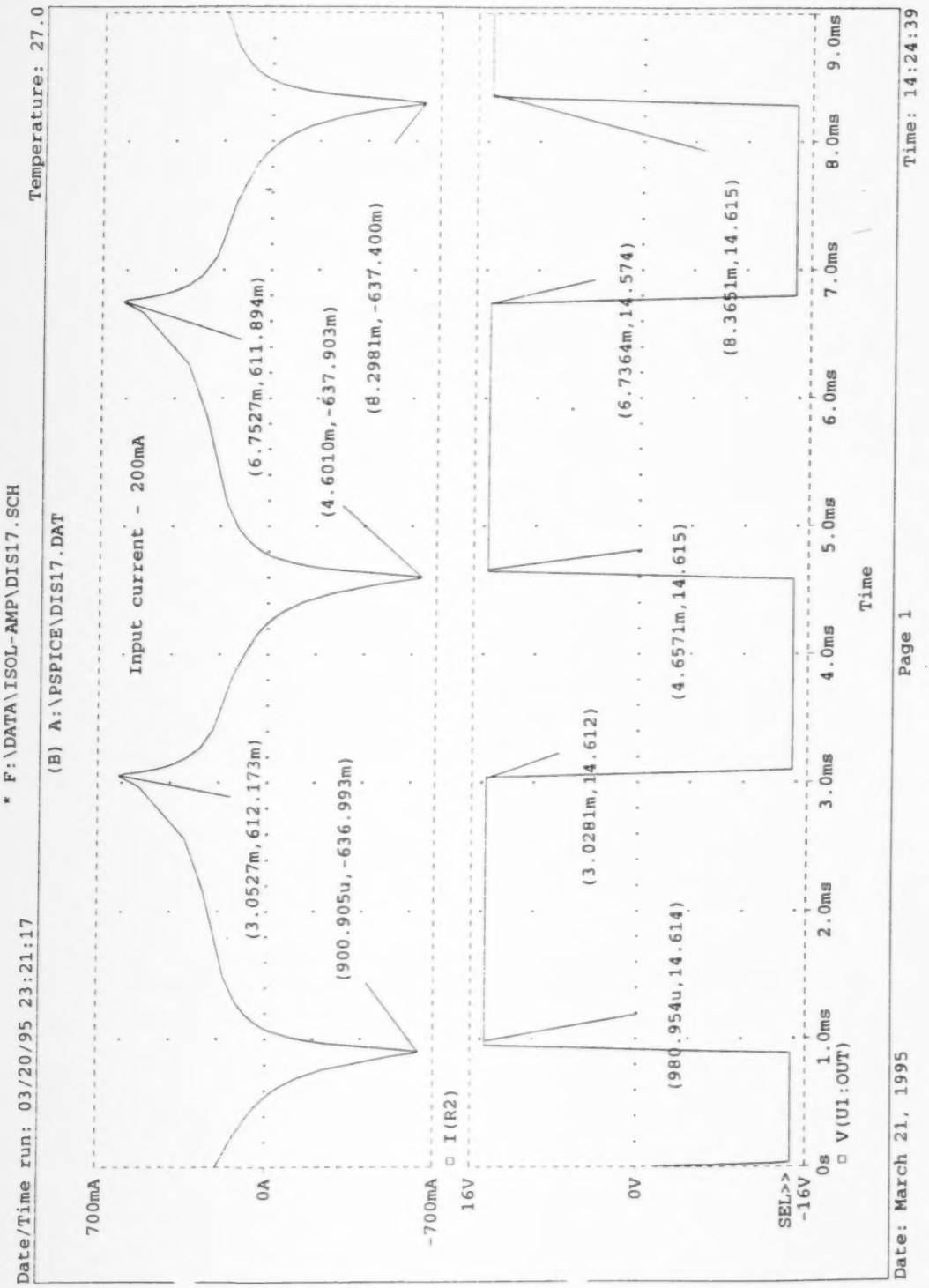

Fig. 29. Simulated waveforms of coil current and Schmitt trigger output for input current +200 mA

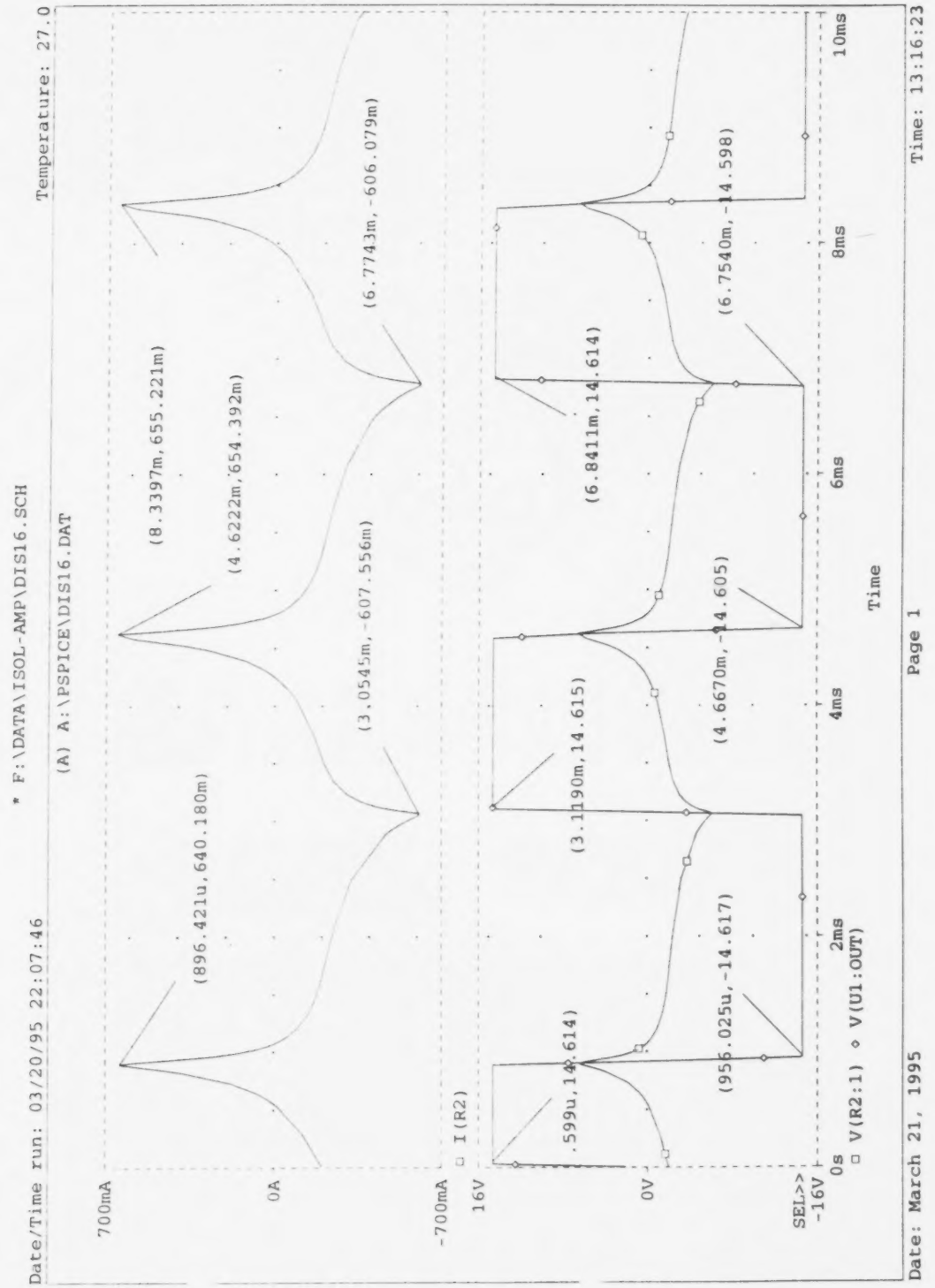

Fig. 30. Simulated B-i_L loop for input current +200 mA

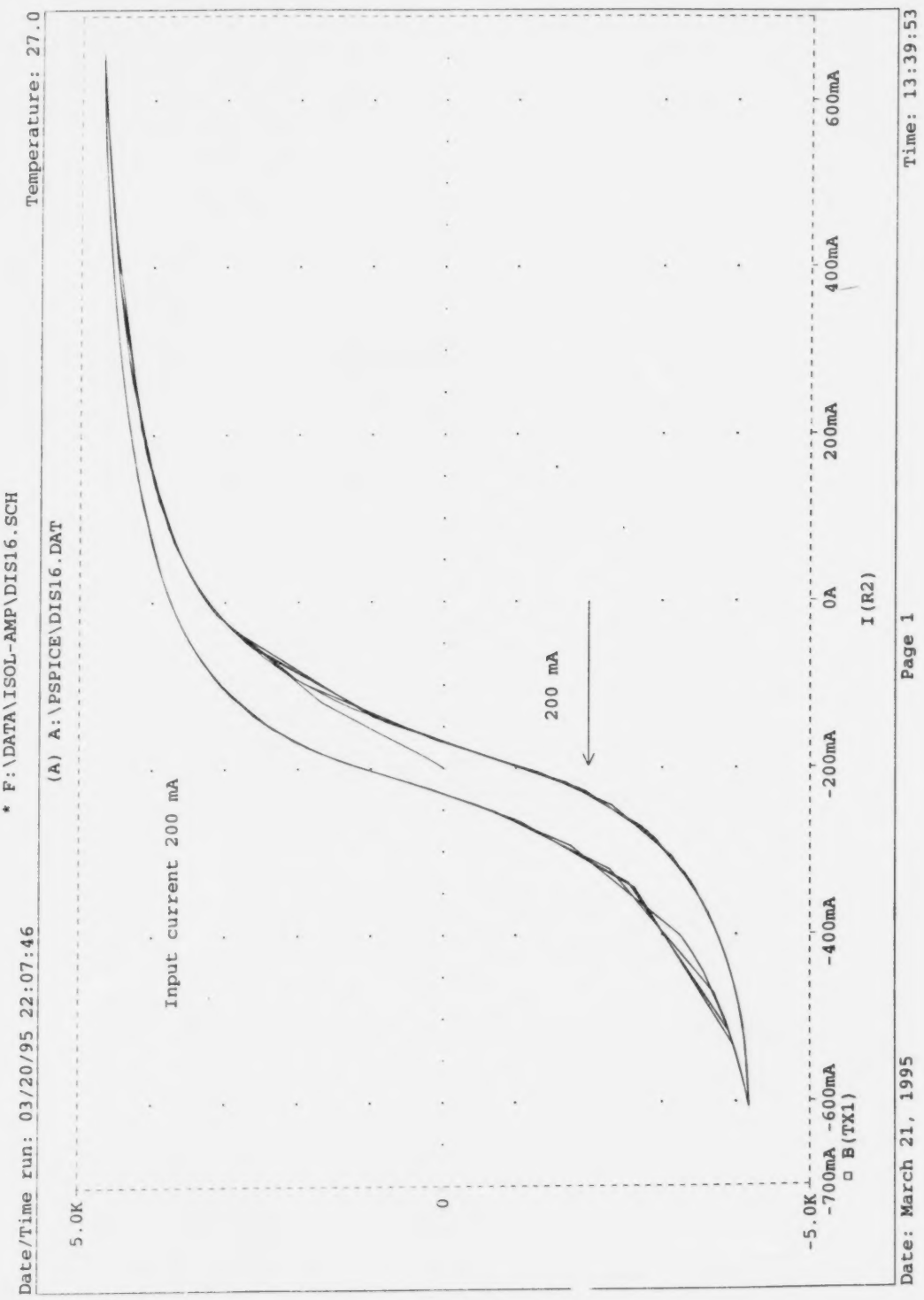

Fig. 31. Simulated B-i_L loop for input current -200 mA

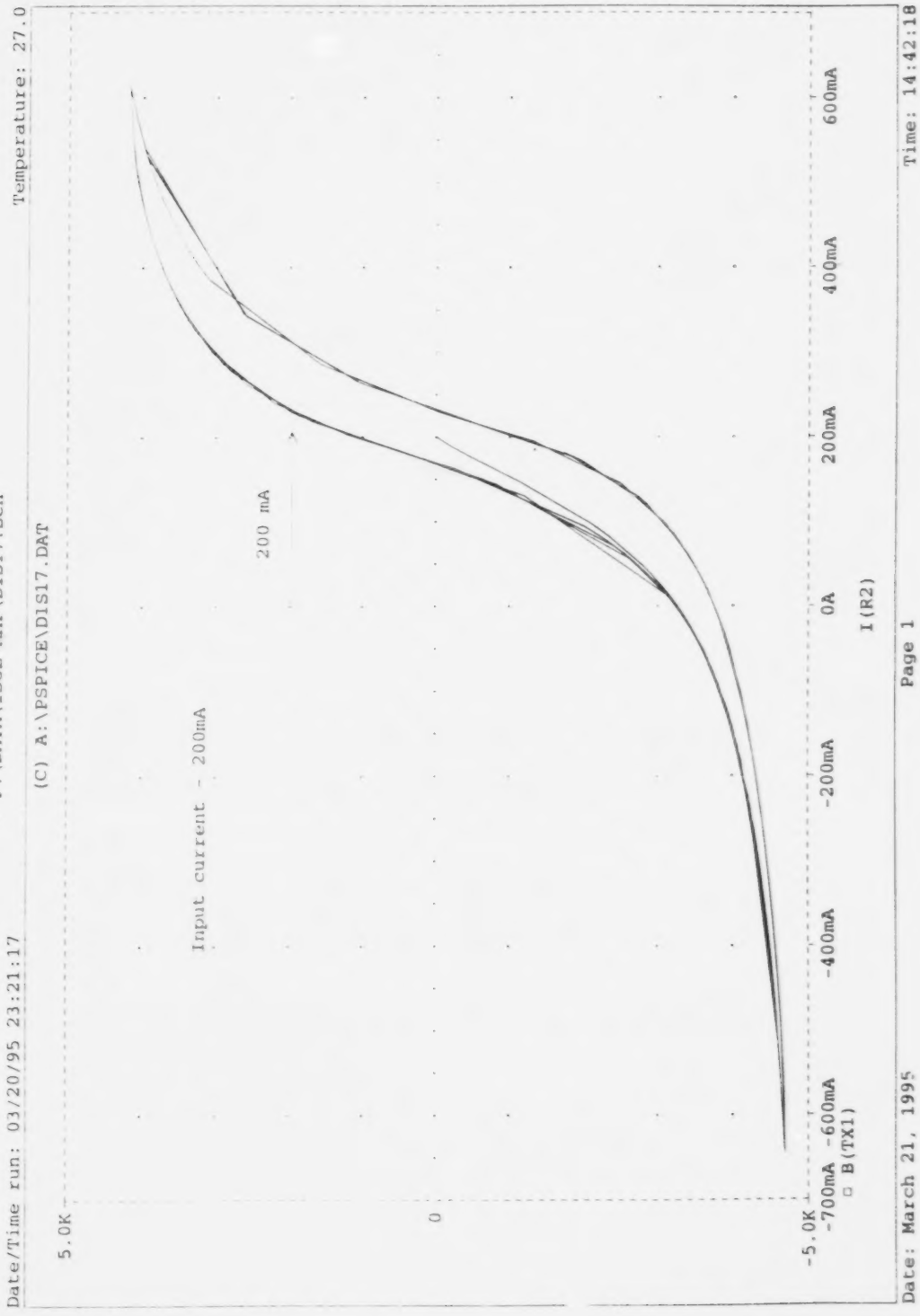

Fig. 32. Simulated waveforms of coil excitation current for ac input current

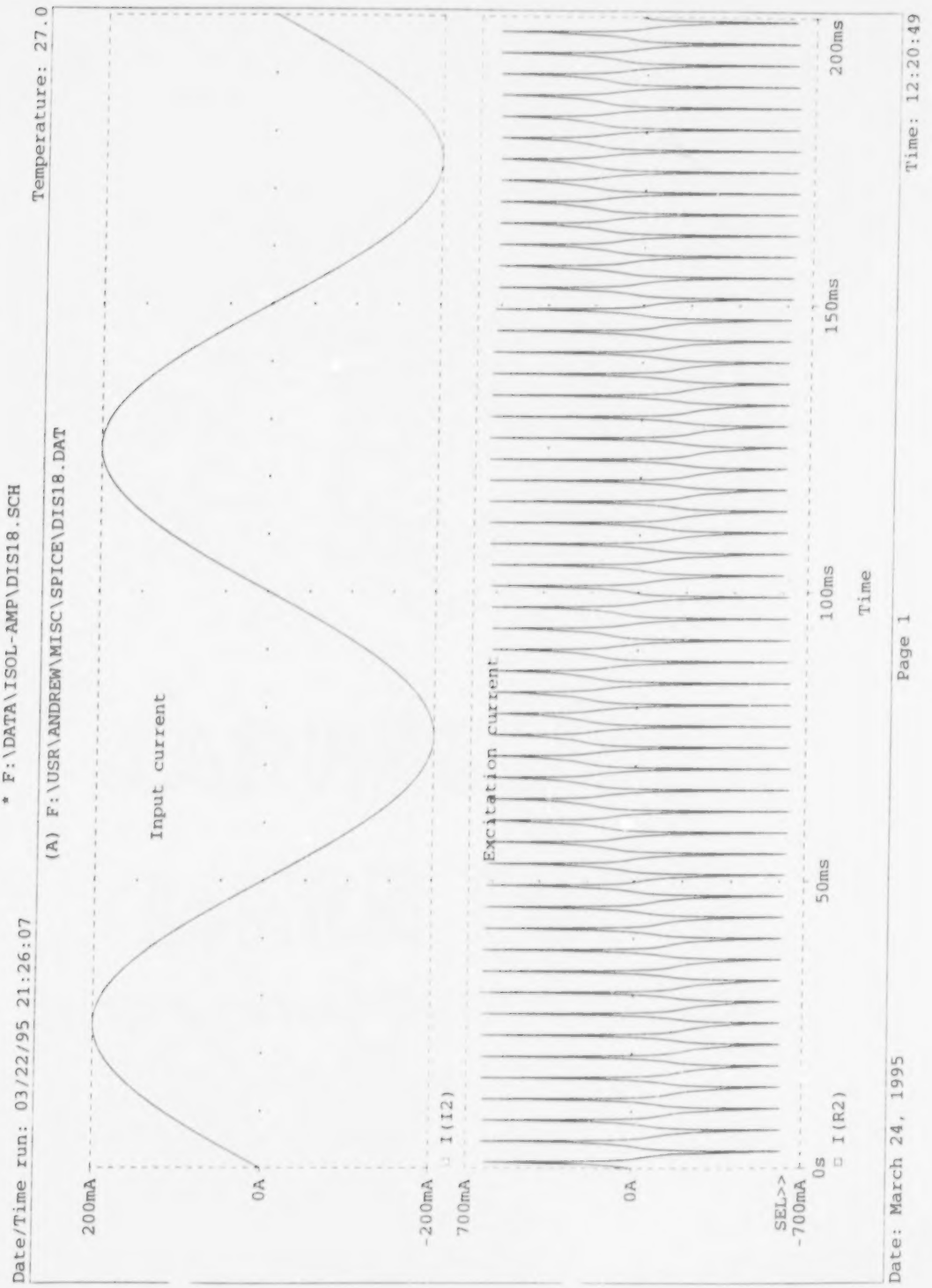

2.5.2. Discussion of the SPICE results

Although the magnetization analysis in PSpice is based on the Jiles-Atherton model the results of simulation strongly support our previous analysis based on linear-saturable, piecewise linear, and polynomial approximations.

It is clear from Fig. 28 and 29 that when the input current is different from zero the driving current waveform takes a specific shape according to the value and polarity of the input. The simulation demonstrates that both the comparator output and the coil current are modulated by the input current. This result is confirmed for both dc (Fig. 28 and 29) and ac input signals (Fig. 32).

The "B-i_L" characteristics given in Fig. 30 and 31 are displaced along the current axis as a result of magnetization by the input current. The distorted shape of these characteristics supports the discussion presented in 2.4.3 regarding undersaturated coil operation. It can be concluded from Fig. 30 and 31 that the maximum driving current set in PSpice model is not sufficient to completely saturate the coil.

The complete current sensing circuit must contain the basic current sensor and the data processing unit which converts the pulse-width modulated signal into the corresponding voltage level. Only the basic current sensor circuit was simulated using PSpice. The mixed analog-digital simulation involving the data processing unit appeared to be beyond the software capability. Nevertheless, by assigning different input current values, and post-processing of the simulation results it became possible to reconstruct the complete output characteristic presented in Fig. 33.

The simulated B-i_L curves provided by PSpice were used to obtain parameters of the polynomial model. This, in turn, allowed the building of an output characteristic according to the polynomial model and compare it with the one from PSpice. The polynomial model calculations were performed for $Y_4 = T^+ - T^-$ (62) using the

following parameters: $a = 0.18\Omega/A^2$, $I_{0M} = 0.6$ A , $\lambda = 1$, $\rho = 0.44$, $R_l = 20\ \Omega$, L = 0.06 H. The calculated current sensor output characteristic is presented in Fig. 33.

As can be seen from Fig. 33 and Table 2 the output characteristic built with the polynomial model and the one reconstructed from Pspice data appear quite close to each other especially in the range of input current ±(0 - 40) mA.

Table 2

	PSpice		Polynomial model
Input current range, A	Average sensitivity, S (sec/A)	Average deviation from the polynomial model, Δ, %	Average sensitivity, S (sec/A)
-(0 - 0.04)	0.00195	+7	0.00209
-(0.04 - 0.1)	0.00176	-16	0.00209
+(0 - 0.04)	0.00194	-7	0.00209
+(0.04 - 0.1)	0.00165	+21	0.00209

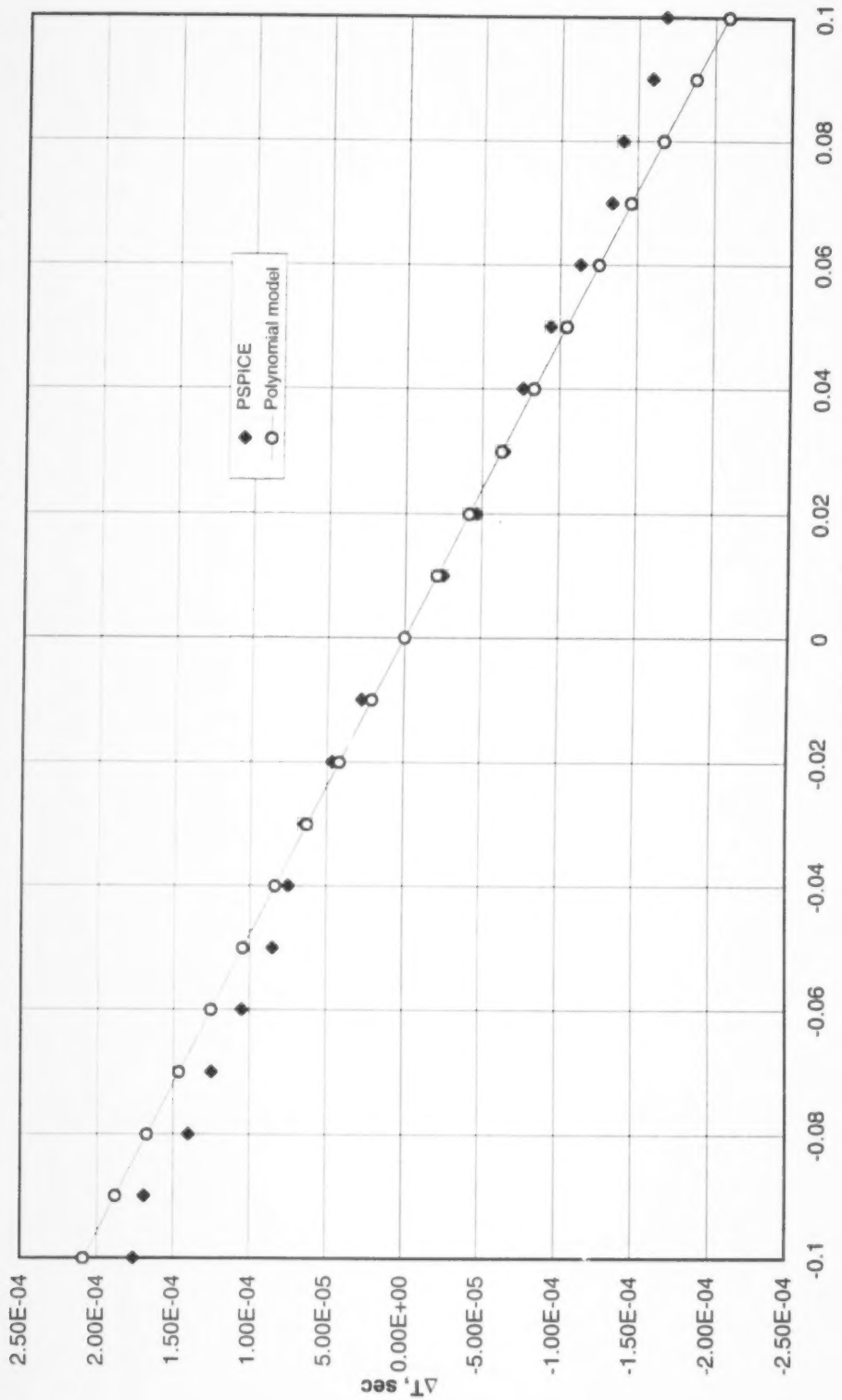

Fig. 33. Current sensor output characteristics according to polynomial model and PSpice

2.6. Concluding remarks

The results presented in this chapter show that the multivibrator circuit with nonlinear magnetic coupling can serve as a basis for transducer in isolation ac and dc current measurements. This transducer converts the input current value and polarity into the duty ratio of oscillation half-cycles.

Transient analysis performed for several magnetization models and confirmed by the SPICE simulation provides expressions for the duty ratio and frequency of the output signal. For the polynomial model it is shown how the output signal components can be formatted in a way which provides the maximal linearity and sensitivity.

Presented magnetization models refer to particular ferromagnetic materials and their properties. Sensitivity and bandwidth of the transducer are shown to be dependent upon fundamental magnetization properties such as magnetic permeability, saturation limits for both B and H and magnetization loop hysteresis.

It is shown that the sensor sensitivity is strongly affected by the circuit structure. The type of feedback control and used reference levels are recognized as two major factors affecting the transducer performance.

The offset in the output characteristic may result from the asymmetrical power supplies or the effect of loop distortion. The hysteresis in the output transducer characteristic can appear as a result of remanent magnetization coupled with an insufficient driving current.

3. Transducer circuit configurations and data processing

This chapter examines several data processing methods for conversion of the primary transducer signal into an analog and/or digital format. Circuit configurations implementing these methods are considered. Special attention is given to error sources and performance limiting factors.

3.1. Filtering

As was shown earlier by both piece-wise and polynomial approximation models, the primary signal of the current transducer has a duty ratio proportional to the input current. Should this signal be converted into an analog signal one can use the low-pass filtering. This is probably the easiest direct method of data processing.

The block diagram of the transducer with direct analog filtering is presented in Fig. 34

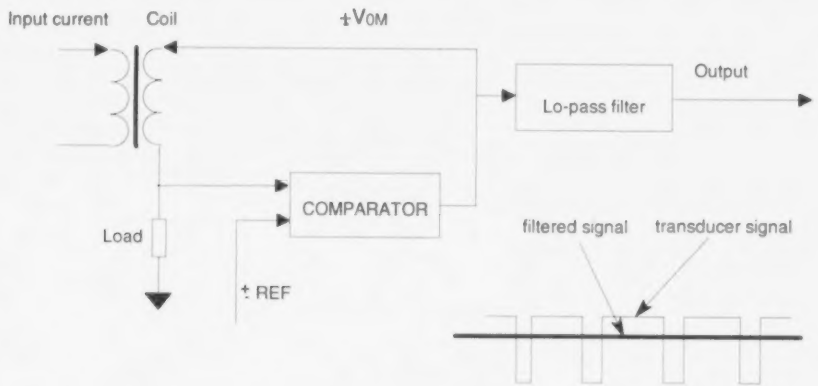

Fig. 34. Direct filtering of the transducer output signal

The filter must possess three characteristics:

- linearity in a working frequency range of input current.
- adequate bandwidth
- minimal phase distortion

Although the above requirements usually conflict in a filter design, and increase the circuit complexity, the direct filtering can still perform satisfactorily for transducers working in dc and infra-low frequency ranges.

3.2. Dual integration with sample-and-hold

3.2.1. Basic circuit structure

Bandwidth limitations associated with direct filtering method can be resolved by a circuit incorporating an integrator with an S/H unit as presented in Fig. 35. The block and timing diagrams of this circuit are shown in Fig. 36.

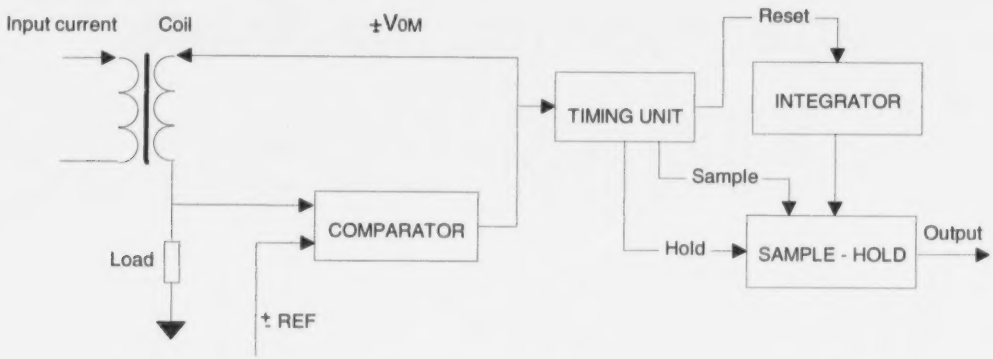

Fig. 35. Block diagram of the transducer with dual integration and S/H

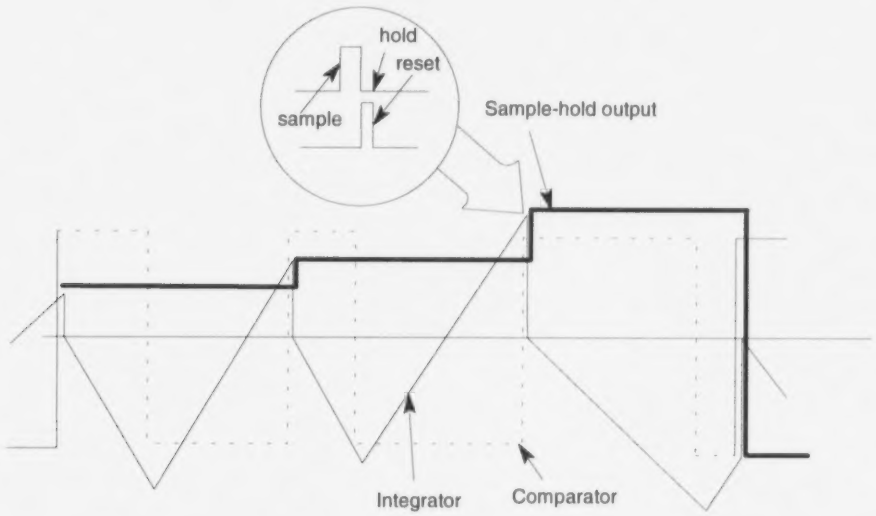

Fig. 36. Timing diagrams of the dual integration - S/H

The five major units of the circuit shown in Fig. 35 are the COIL NETWORK, COMPARATOR, INTEGRATOR, SAMPLE-HOLD and TIMING UNIT. The COIL NETWORK and COMPARATOR in a Schmitt trigger mode form the basic current

sensor circuit. The INTEGRATOR is connected to the output of the COMPARATOR. The SAMPLE-HOLD (S/H) circuit is connected to the output of the INTEGRATOR. The TIMING UNIT fed from the COMPARATOR generates digital signals, controlling both the INTEGRATOR and S/H operation.

At the beginning of each oscillation cycle the TIMING UNIT sends a series of three commands. The first is the instruction for the S/H circuit to "sample" the signal from the INTEGRATOR. The second pulse resets the INTEGRATOR to zero, and finally, the third pulse forces the S/H into "hold" mode.

The COMPARATOR output is a bipolar square wave with limits at $+V_{0M}$ and $- V_{0M}$ therefore, the INTEGRATOR operates in a dual integration mode. This means that after both half cycles the result of integration is proportional to the difference between T^+ and T^- . Since each full cycle starts with the initial reset, the result of integration does not depend on a duty ratio in the previous cycle. This voltage is sampled and held by the S/H circuit which keeps the result up to the moment when a new "sample" command is sent.

The described recurring procedure provides the data flow with the fastest possible response to the changing input signal. The theoretical delay in this circuit is equal only to the length of oscillation period T. However, in a high-frequency design neither the INTEGRATOR nor the S/H can be considered ideal. Consequently, to achieve high accuracy special precautions must be made with regard to the time delays needed for sampling, resetting the INTEGRATOR and switching the S/H back to the hold mode.

If the "sample", "hold" and "reset" commands are generated by the same COMPARATOR output which is also directly driving the coil, these signals can appear only after the V_{SRC} polarity is flipped over. Additional time will be needed to finish the sample-hold and reset operations. As a result there will be an integrated

signal disparity between the moment when the voltage source was switched over and when the actual sampling occurred. A sampling error is shown in Fig. 37(a).

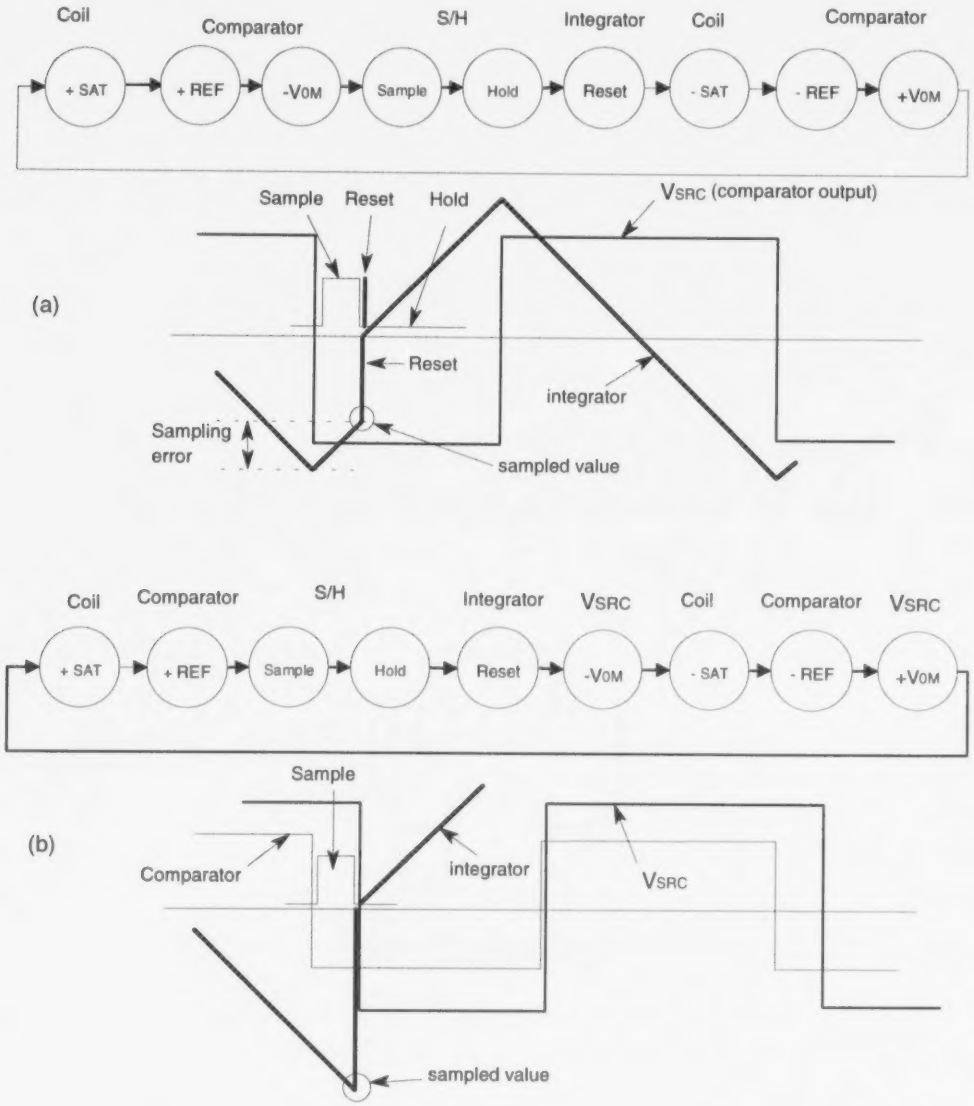

Fig. 37. Control signals in the INTEGRATOR - S/H circuit
(a) - conventional ∫ - S/H circuit with sampling error
(b) ∫ - S/H circuit with leading sampling

3.2.2. Dual integration with leading sample-and-hold

The circuit shown in Fig. 38 is intended to improve the accuracy of the current sensor in high frequency applications. The timing diagram of this circuit is presented in Fig 37(b).

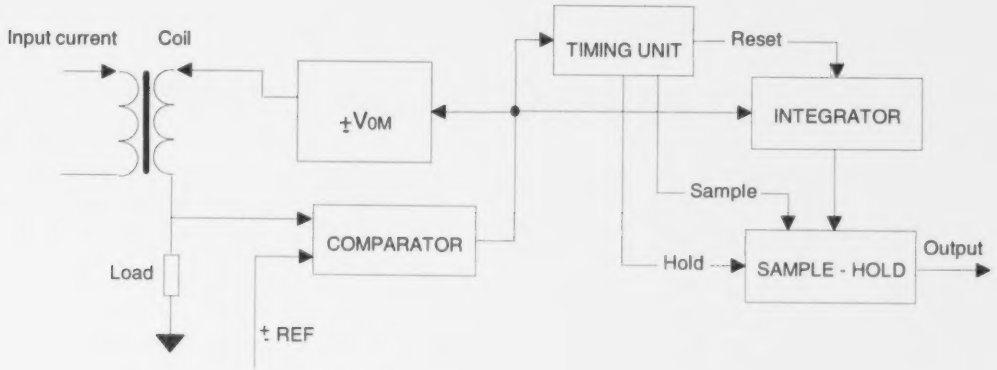

Fig. 38. Current transducer with leading sampling

The main idea of leading sampling is to change the sequence of events such that the sampling is performed before $\pm V_{0M}$ polarity change. To achieve this goal the comparator is not directly driving the coil but is instead controlling two additional switchable voltage sources ($+V_{0M}$ and $-V_{0M}$). This operation provides the time delay necessary for accurate sampling. In addition, the separate $\pm V_{0M}$ voltage sources provide a means for offset compensation and can be used in feedback control.

3.2.3. Bandwidth limitations

In order to evaluate different transducer circuit solutions it is useful to obtain a quantitative insight into the problem of current transducer bandwidth and error budget. We shall perform this analysis on the output of the S/H circuit.

The S/H signal shown in Fig. 39 represents a zero-order hold operation with respect to an 'averaged' input signal measured during the previous measurement cycle. Although the actual 'averaging' mechanism is a function of transducer linearity, to simplify the mathematical treatment we assume that the oscillation (measurement)

cycle T is small and the corresponding change of input current is linear. This allows us to consider the linear output characteristic, thus excluding the effect of input signal phase on transducer sensitivity.

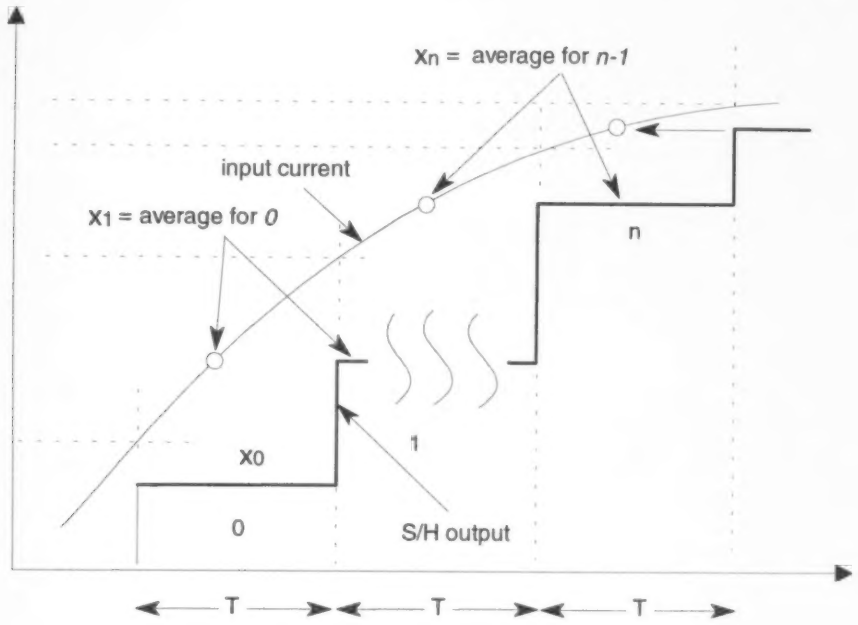

Fig. 39. Zero-hold operation of the S/H output

Applying the approach commonly used for calculation of the sampling rate of digital-analog conversion [34] we can replace the S/H signal of Fig. 39 with a sum of *sinc* functions shown in Fig. 40.

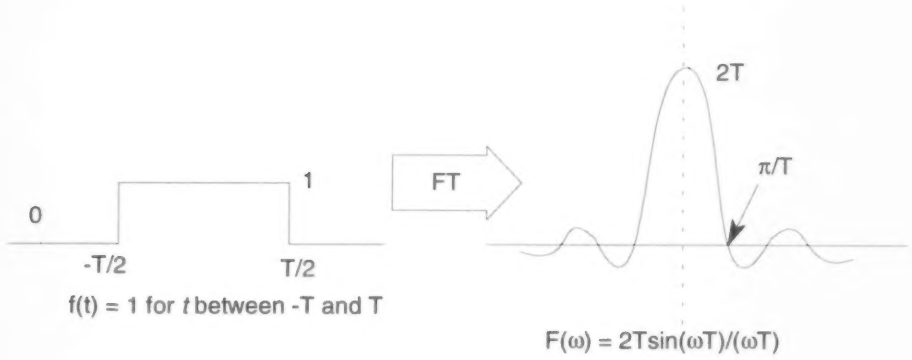

Fig. 40. Rectangular (rect) function and its inverse transform

After applying the phase shift, the spectrum of the n = 0 segment of height x_0 yields

$$X_0(\omega) = x_0 \frac{2\sin\left(\frac{\omega T}{2}\right)}{\omega} e^{\frac{-j\omega T}{2}} \tag{65}$$

Using superposition, the complete expression for all S/H values can be written as

$$X(\omega) = \sum_{n=0} x_n \frac{2\sin\left(\frac{\omega T}{2}\right)}{\omega} e^{-j\omega[n+(1/2)]T} \tag{66}$$

which can also be presented as

$$X(\omega) = \frac{1-e^{-j\omega T}}{j\omega} \sum x_n e^{-j\omega nT} \tag{67}$$

This gives us an expression for the transfer function of the zero-order system

$$H(\omega) = \frac{1-e^{-j\omega T}}{j\omega} \tag{68}$$

which can be reduced to

$$\left|H(\omega)\right| = T\frac{\sin(\omega T/2)}{\omega T/2} \tag{69}$$

Since the oscillation cycle $T = 1/f_d$ and $\omega = 2\pi f_{in}$ the expression (69) can be rewritten to clearly show the effect of the sin(x)/x amplitude distortion on the output:

$$\left|H(2\pi f_{in})\right| = \frac{1}{f_d} \frac{\sin\left(\pi \frac{f_{in}}{f_d}\right)}{\pi \frac{f_{in}}{f_d}} \tag{70}$$

The last expression enables us to calculate the relative amplitude distortion error δ_a as a function of ratio f_d/f_{in} (Fig. 41). For $f_d = 2f_{in}$, which is the lowest permissible frequency defined from the Nyquist criterion the amplitude distortion is $2/\pi$ or 3.92 dB.

From the design standpoint expression (70) provides useful information about the minimal oscillation frequency needed to obtain the particular accuracy level. It is clear for example, that in order to achieve 0.1 % accuracy at 1000 Hz input the transducer must run at a frequency of at least 40 kHz.

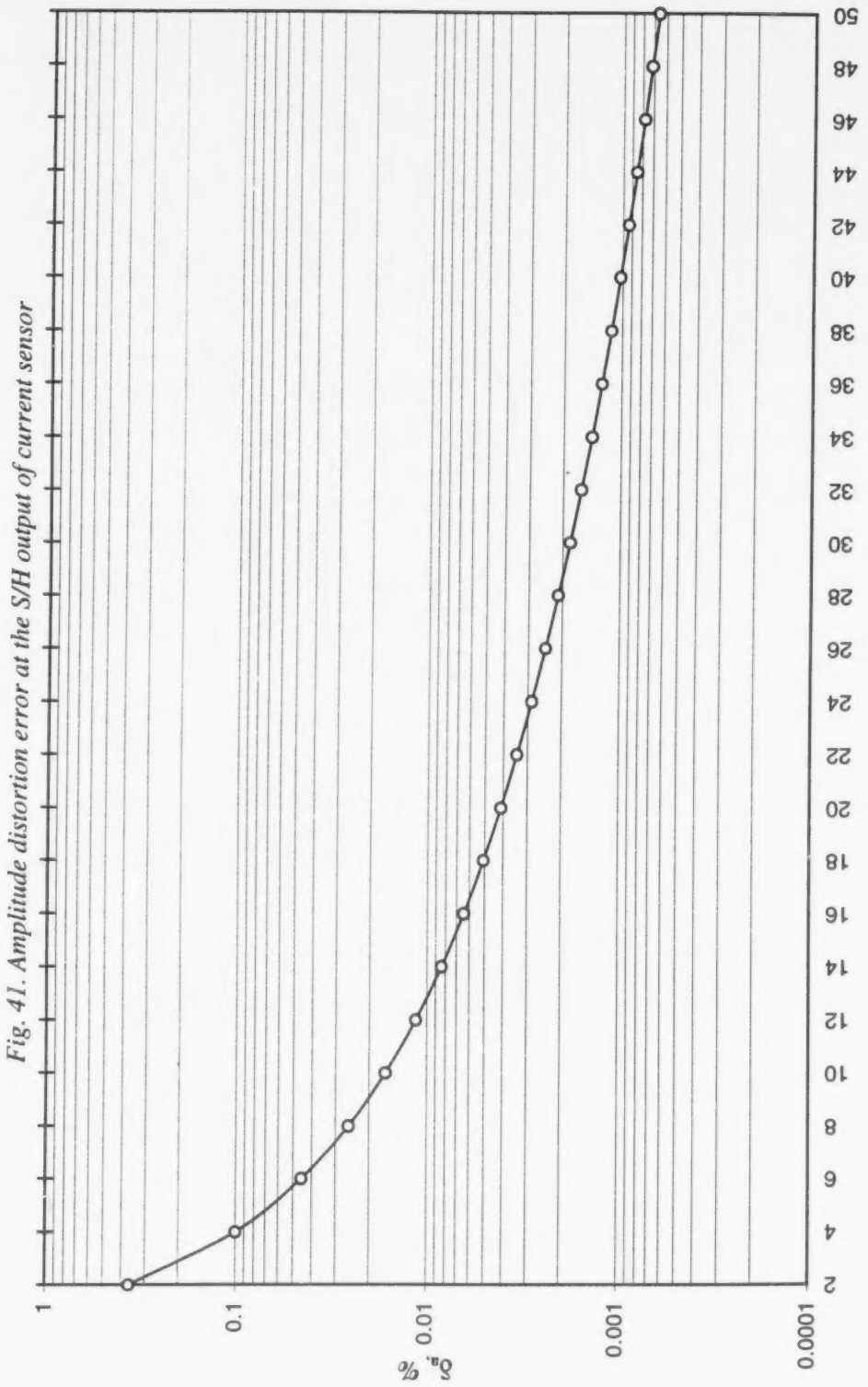

Fig. 41. Amplitude distortion error at the S/H output of current sensor

In addition to the amplitude distortion the transducer has a phase shift related to the fact that it takes at least a complete oscillation cycle of the length $T^+ + T^-$ to convert the value of input current into the duty ratio. This phase shift can be obtained from

$$\Theta = 2\pi f_{in}/f_d \tag{71}$$

It should be noted that the above discussion concerns not realistic but the lowest achievable distortion levels. The actual transducer errors will result from a combined action of many other design factors such as magnetic core properties, electronic components and coil specifications. However the analysis clearly indicates that to achieve the lowest amplitude and phase distortion the operating frequency must be made as high as possible.

Some of the frequency affecting factors fit into the category of magnetic core properties. Each type of magnetic core has a maximal recommended operating frequency. For many square loop materials in tape wound cores this limit should be set between 10 and 250 kHz. Although many ferromagnetic materials will provide much higher operating rates it can be shown that the limitations set by electronic components are usually more strict.

The limitations will be set by comparators, switches and operational amplifiers due to their finite switching rate. Fig. 42 presents the output of the comparator used for sensing the reference level crossing. The portions of the oscillation cycle pertaining to the transient intervals limit the accuracy of conversion. To guarantee the minimal accuracy the design solution must either call for faster comparators or eventually decrease the driving frequency.

Since the transducer oscillation cycle comprises three comparator transitions, and each can be a part of either T^+ or T^-, the resultant absolute switching error can be calculated as a sum of propagation delays.

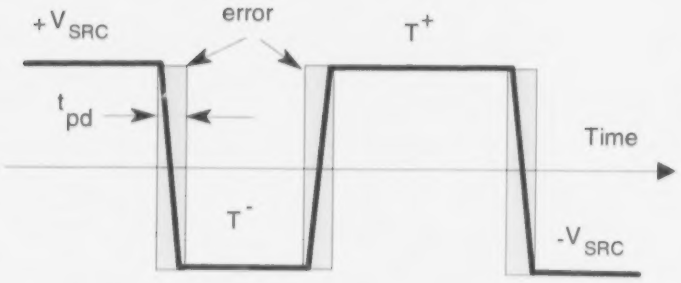

Fig. 42 Switching error evaluation model

If the relative switching error is δ_{SW} and the driving frequency is f_d the required propagation delay t_{pd} of a comparator can be calculated from the expression:

$$t_{pd} < \delta_{SW}/3\, f_d \tag{72}$$

Two of the best comparators currently available on the market are an ultra-fast AD9696 from Analog Devices and a HFA-0003 from Harris. They have the propagation delays 4.5 ns and 2 ns respectively [2], [3]. Simple calculations show that AD9696 can provide not more than 0.1 % accuracy at 74 kHz while the 0.1 % limit for HFA-0003 is 167 kHz.

If the ultra-high speed OA is used in comparator mode the required slew rate (SR) will be

$$SR > \frac{2V_{SRC} f_d}{\delta_{SW}} \tag{73}$$

For example if a hypothetical OA with SR = 1000 V/μs is used for driving the coil and errors introduced by other circuit components are not considered, in order to achieve 0.1 % accuracy the maximal driving frequency can not exceed 17 kHz for V_{SRC} = 10 V.

Additional limitations will be superimposed by the coil design. To achieve the highest possible oscillation frequency the small coil inductance must be driven by a large excitation current. But these two parameters are interdependent, and besides may

conflict with other design objectives. This is especially true with regard to small high-frequency cores.

To illustrate this point we may note that the current is limited by the wire size. Since the wire size is related to the core dimensions and also because it is undesirable to have a large driving current from the power consumption standpoint, the current must be limited. Yet to saturate the core with a smaller current the number of turns must be increased. This design step will subsequently increase the inductance.

In some cases increasing the oscillation frequency, even if possible, may conflict with sensitivity requirements. It was shown in Chapter 2 that for undersaturated operation and nonrectangular magnetization characteristics the sensitivity will grow with the reference levels set closer to the complete core saturation. This sensitivity growth will, however, be accompanied by the oscillation frequency decline that is demonstrated in Fig. 43. The higher the reference level is, the greater the sensitivity of the transducer will be, and the lower its oscillation frequency will be.

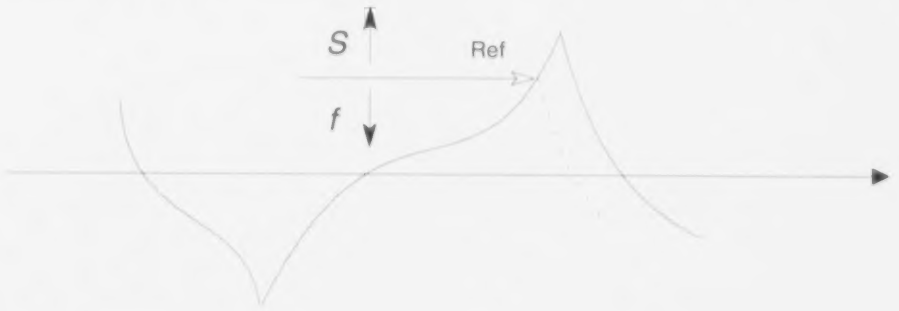

Fig. 43. Reference level effect on the sensitivity and oscillation frequency

3.2.4. Boosting the oscillation frequency and dead zone reduction

Considering the influence of reference levels in Chapter 2 it was shown that there exists some central part of the magnetization characteristic which is formally insensitive to the input current. As presented in Fig. 44 for the family of displaced linear-saturable ψ-i characteristics the dead zone is located between $+I_S - |\lambda|$ and $-I_S + |\lambda|$. Although this zone does not affect the pulse-width deviation it extends each

oscillation half cycle by a time interval needed to pass it. As a result two equal time intervals are added to the oscillation cycle which appears to be a damping factor for the oscillation frequency.

Since the transducer primary signal contains dead zone constituents which are further transmitted to integration and S/H steps, it affects both the signal range and the signal-noise ratio (S/N) of the current transducer. The signal range at the integrator output can be defined as a difference between a peak voltage value (eg. close to power supply) and an integrated length of dead zone pedestal. For example, if a dead zone occupies 40 % of an oscillation cycle the output of the integrator representing the measured input signal will be limited to 60 % of the full scale.

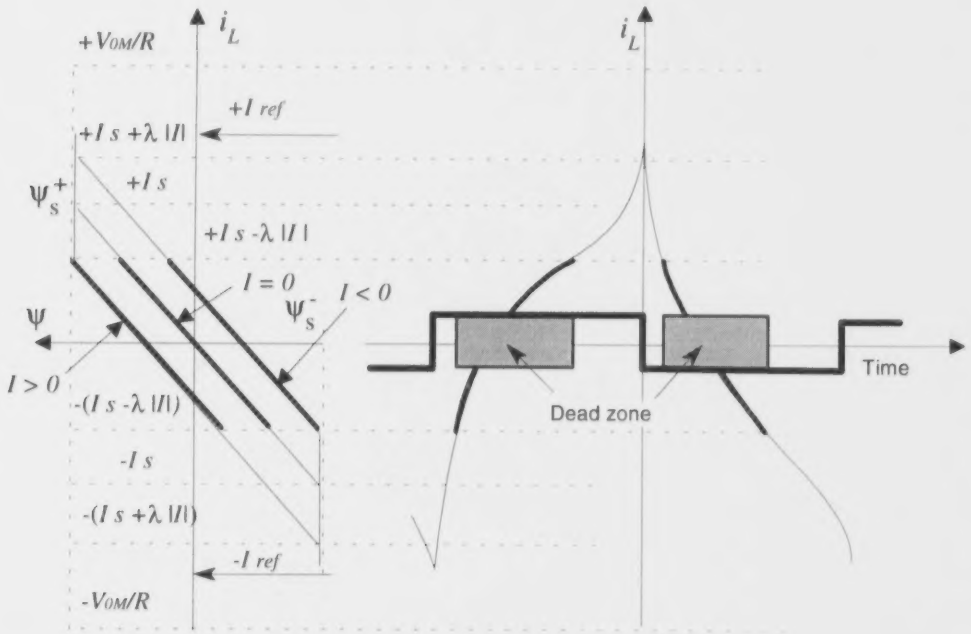

Fig. 44. Dead zone of the current transducer

The following circuit solution was proposed to reduce the dead zone and increase the oscillation frequency. It is based on a concept of introducing a special fast-charging mode such that the time spent in passing through the dead zone can be significantly shortened.

It is possible to temporarily increase the $\pm V_{0M}$ or reduce the load resistance inside the region recognized as a dead zone. This will increase the coil current and shorten the time spent inside this zone. Since the dead zone is passed through once in each half cycle it is important to provide the symmetry in switching the above electrical parameters. This will ensure the symmetrical reduction of the 'dead' portions from both T^+ and T^- half cycles.

The circuit presented in Fig. 45 contains the same functional blocks as the circuit with leading sampling in Fig. 38 with the addition of a DEAD ZONE REDUCTION (DZR) unit. In this circuit the polarity of the driving voltage is controlled by the COMPARATOR while the DZR output controls the value of driving voltage.

The DZR unit is essentially a window comparator whose function is to detect whether the coil current is inside the dead zone. For this purpose the DZR has two preset reference inputs (not shown in Fig. 45). When the current enters the dead zone and crosses one of the DZR reference levels the output of the DZR switches the corresponding voltage source to a higher $\pm V_{DZ}$ value. When the current leaves the dead zone the DZR unit returns the driving voltage to its initial $\pm V_{0M}$ level.

Because the applied voltage is substantially higher inside the dead zone it takes much less time for the coil to pass it through. As a result the total transient time necessary to move the coil from one saturation state to another is decreased. As shown in Fig. 45, this circuit solution can substantially increase the oscillation frequency.

An additional advantage of this circuit is that it eliminates the conflict between the transducer sensitivity and operating frequency, considered earlier in this chapter (see Fig. 43). Here it is possible to compensate an increase of maximum driving current (that normally leads to longer transient times) by cutting off the dead zone (which increase the operating frequency).

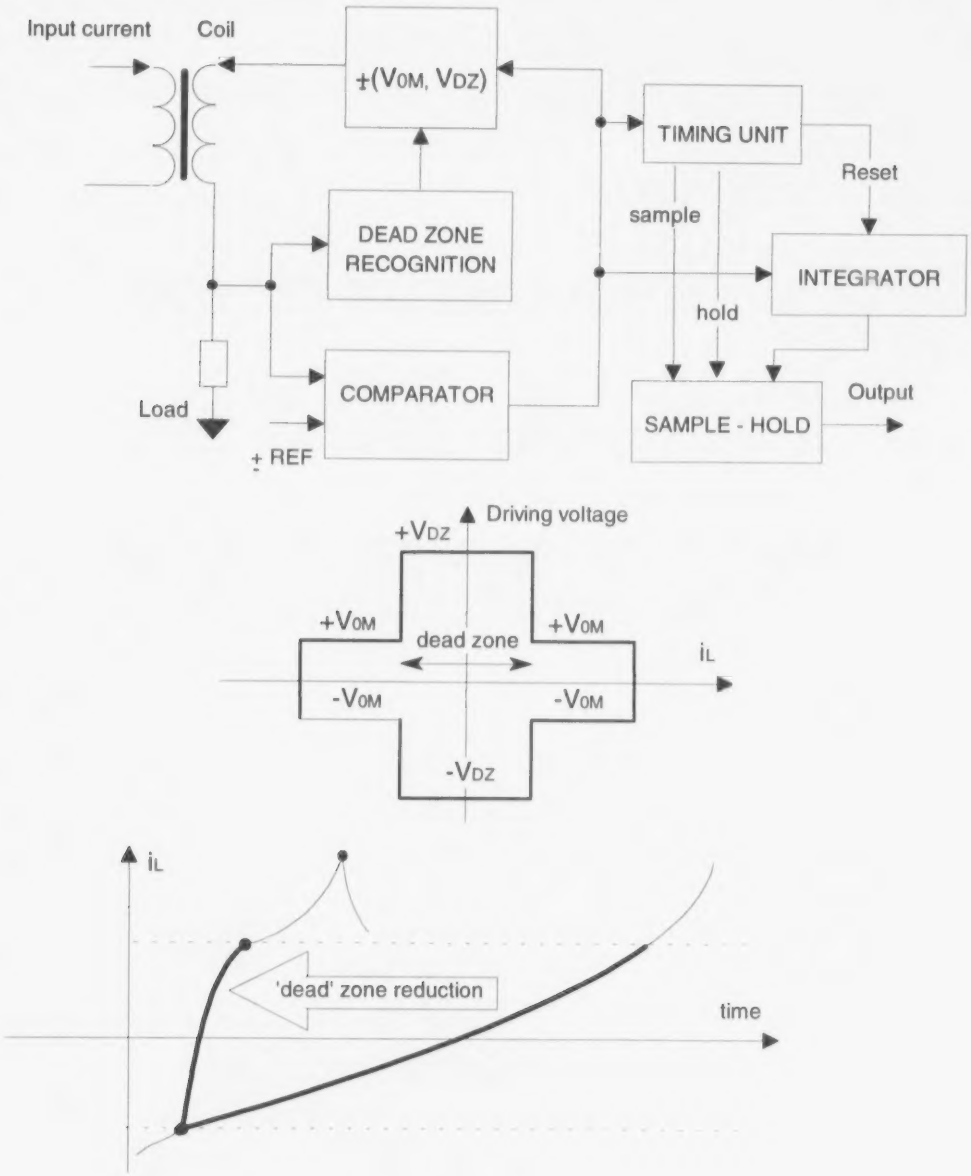

Fig. 45. Transducer with dead zone reduction (DZR) function

3.2.5. Increasing the dynamic range of dual integration

The dead zone reduction (DZR) principle must be supported by a very fast high quality window comparator and analog switches. In general it requires circuit components with even higher operating speeds than the rest of the circuit. This factor can make it difficult to design the DZR for transducers already working at high oscillation fequencies. Still there is a possibility to improve the S/N ratio of the integration stage without increasing the oscillation frequency.

The circuit presented in Fig. 46 contains an additional analog INTEGRATION SWITCH between the COMPARATOR and the INTEGRATOR input. This switch disconnects the INTEGRATOR input for the time T_{HOLD} each time a new oscillation half cycle starts. Switch operation is controlled by the TIMING UNIT.

The circuit modifies the INTEGRATOR operation such that one time interval T_{HOLD} is cut off from each integration direction. It allows use of a smaller INTEGRATOR time constant that is equivalent to obtaining the ΔT with higher resolution. Complete elimination of the dead zone effect on the INTEGRATOR output is reached when T_{HOLD} equals T_{DZ}.

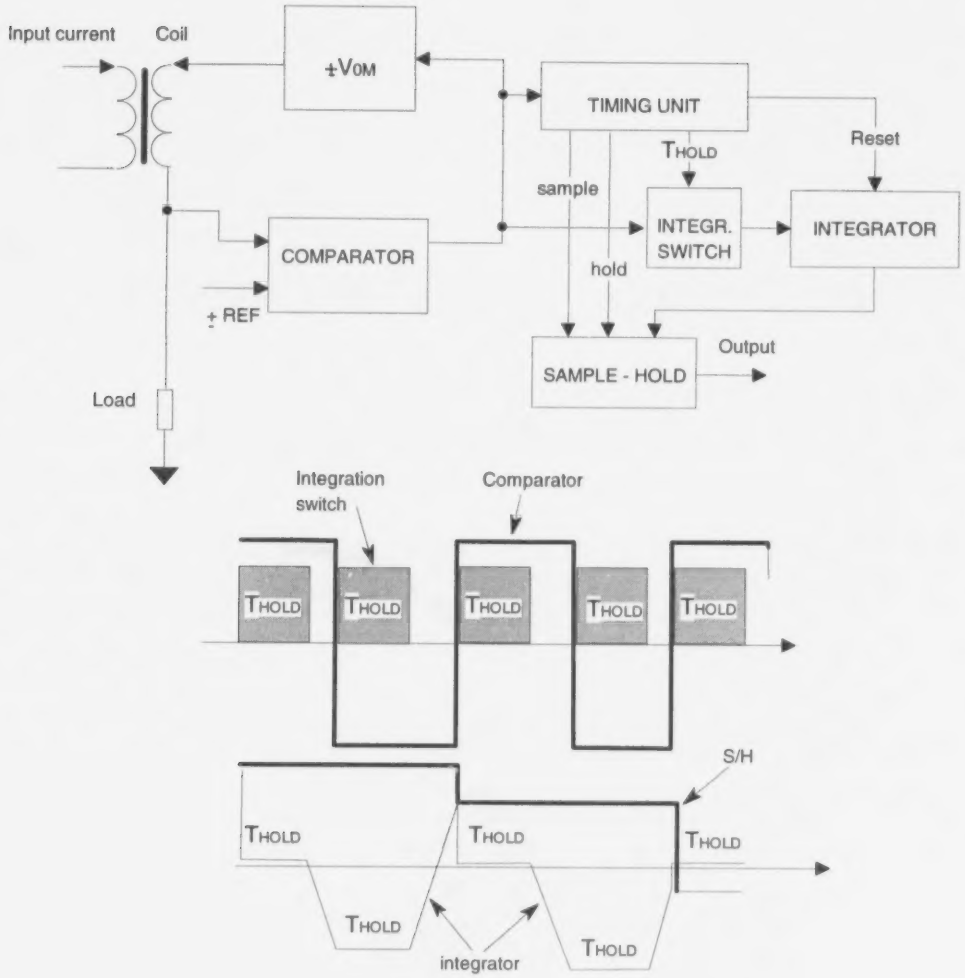

Fig. 46. Increasing the dynamic range of dual integration

3.2.6. Flux saturation detector

As mentioned previously, there are two possible methods of identifying the coil saturation. The first method is based on measurements of the coil current, while the second uses the voltage across the coil excitation winding. Because the derivative of the flux linkage approaches zero as the coil saturates, the voltage across the coil must also decrease dramatically, formally up to the level defined by the coil internal ohmic resistance.

The transducer circuits implementing this type of control can comprise of the same elements presented above with the exception of the COMPARATOR. The latter can be designed as a window comparator. Advantages of this type of multivibrator control were outlined in the Chapter 2.

3.2.7. Suppression of the oscillation frequency interference in a primary loop

All aforenamed transducer characteristics were derived with an initial assumption that the input signal is supplied by a current source. Indeed an ideal curent source would be insensitive to any voltage transformed from the driving winding N_1 to the measurement side N_2. However, in reality the current source characteristics can be approached either by considerably increasing the internal resistance of the input signal source or by electronic means located at the measurement side. Obviously the first solution makes it impossible to measure low currents (unless they are provided by very high voltage source), while the second defeats the purpose, which is to design an isolation transducer without any additional circuitry at the measurement side.

The circuit presented in Fig. 47 is an effective way to suppress the transformed voltage in the measurement loop at the cost of an additional coil. If both load resistors and the coils are identical it will provide a decoupling countercurrent in the measurement winding which will eliminate the effect of oscillation current.

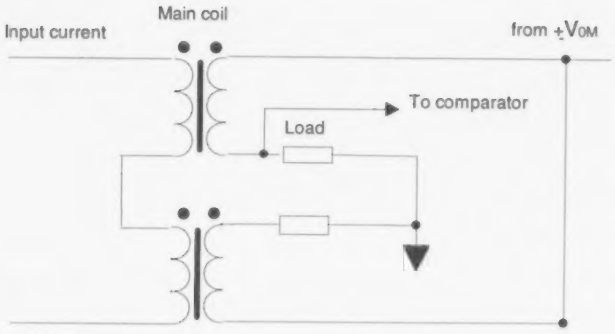

Fig. 47. Interference suppresser

3.3. Digital processing

Digital processing is an alternative approach to the current transducer design. Its major advantages include high speed, flexibility in choosing a suitable signal format and opportunities to store and process the measurement data. The digital processing will naturally be used for applications where the current transducer operates as part of a computerized data acquisition system. However, the digital processing is inconvenient in cases where the application requires an analog output.

We will consider the digital processing method based on a synchronous up-and-down counter with output latch memory. The circuit was designed and implemented as a custom FPGA CMOS integrated circuit (see Chapter 4). Fig. 48 presents functional and timing diagrams of the corresponding digital processing unit.

The digital processor circuit measures the time difference between adjacent positive and negative half-periods of the oscillation frequency. This task is performed with a help of an internal reference frequency provided by the CLOCK unit and the synchronous up-an-down COUNTER with latched ouput.

The COUNTER UP or DOWN mode is defined by the COMPARATOR state. When the COMPARATOR output is high the COUNTER is counting UP, reaching the M state (see Fig. 48) at the end of T^+ interval. When the COMPARATOR output is low

the COUNTER is counting DOWN, this results in a subtraction of some number of N pulses from M. Because M and N are proportional to T^+ and T^- respectively, by the time the COMPARATOR switches back to '1' the COUNTER will have reached the M-N state.

The LATCH memory is used to store the M-N number which is a measure of a pulse width difference $2\Delta T$. As shown in Fig. 48 the LATCH is turned on at the beginning of T^+ and stores the M-N result throughout the next oscillation cycle. After the M-N number is sent to the LATCH memory the COUNTER is reset.

The counter size (in bits) and CLOCK frequency should be chosen depending on the necessary accuracy and operating frequency of the current transducer. To avoid the counter overflow the following condition must be satisfied

$$2^{n-1}/f_{CLOCK} > T^+ \text{ or } T^- \tag{74}$$

Assuming that in an extreme case T^+ or T^- can change from 0 to $1/f_d$ we can write

$$2^{n-1}/f_{CLOCK} > 1/f_d \tag{75}$$

where f_d is the driving (oscillation) frequency.

Conversely, the measurement resolution of the digital processor expressed via the relative counting error δ_c is dependent upon the number of clock pulses that are available during each counting session

$$f_{CLOCK} > f_d/\delta_c \tag{76}$$

Combining (75) and (76) we finally obtain

$$f_d/\delta_c < f_{CLOCK} < 2^{n-1} f_d \tag{77}$$

Expression (77) enables us to calculate the necessary f_{CLOCK} for a particular counter size and given f_d and δ_c or find the minimal counter size for the rest of the known parameters. For example, if the transducer operates at 40 kHz and the error must not exceed 0.1 %, the clock frequency must be at least 40 MHz . If the clock frequency in turn is 40 MHz the second part of (77) yields $n_{min} = 11$.

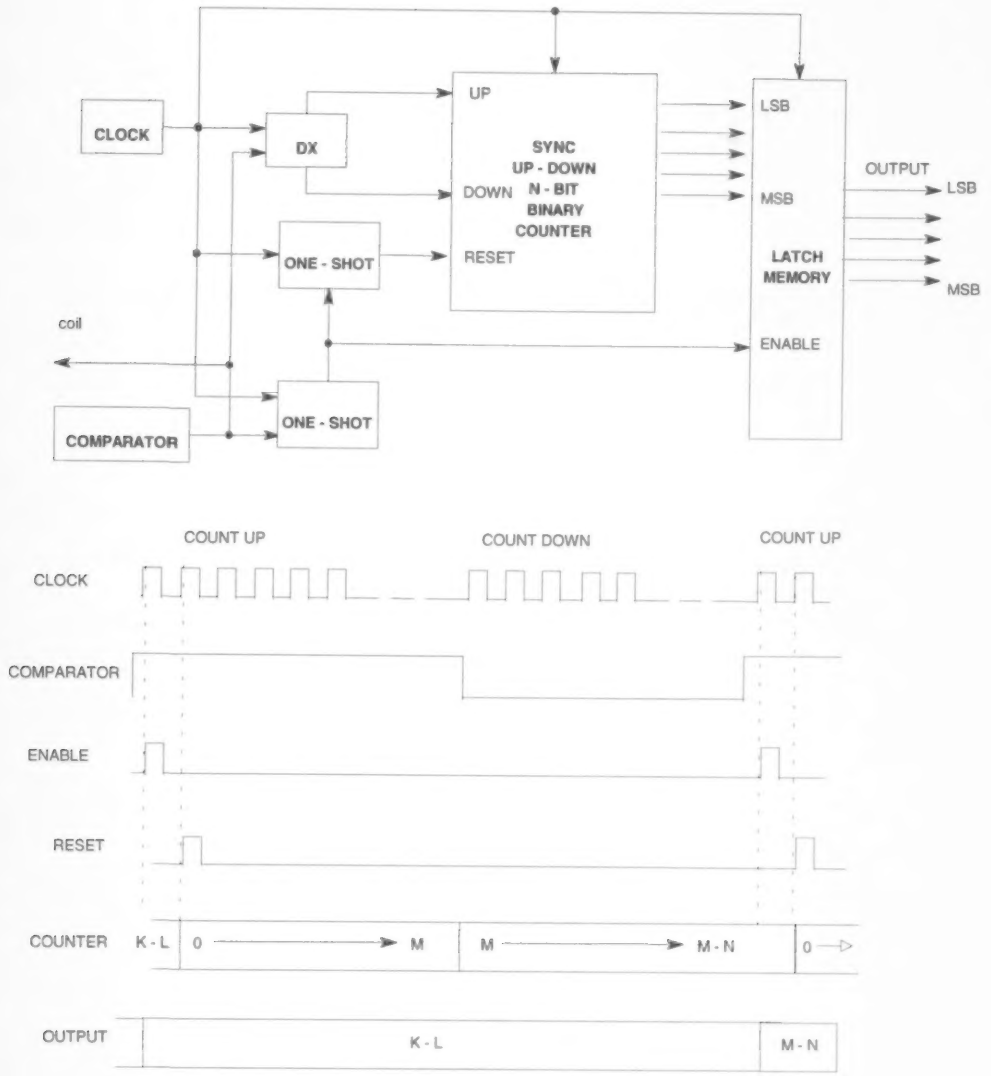

Fig. 48. Digital processing

In order to be able to express a bipolar input current the designed FPGA version of the digital processor is employs an offset binary code which is shown in the Table 3.

Table 3

Measured pulse-width difference, $2\Delta T$	Code
$-2\Delta T_{MAX}$	000 ... 000
0	100 ... 000
$2\Delta T_{MAX}$	111 ... 111

4. Design of the isolation measurement system

This chapter presents some practical isolation measurement circuits designed and experimentally studied during preparation of this thesis. Experimental results are discussed and some ways to improve the circuit performance are considered.

4.1. Performance parameters

4.1.1. Current range

There are no design factors which specifically define or limit the highest measureable current. The concept of isolation measurement circuit can still be implemented no matter how large the coil or wire size are. However, the current range increase can not be reached without indirectly affecting some other circuit characteristic. For example, to design a transducer for high current measurements the wire and core size must be increased whereas many materials are not available in large sizes. This will affect the choice of core material. As a result the sensitivity factor and measurement bandwidth will be affected and limited.

The lower limit of measurable input current I_{min} depends on uncertainty and Barkhausen noise [22], [35] found in a particular core material. In general the loop displacement associated with the minimal measurable current, as shown in Fig. 49, must be at least greater than the range of uncertainty in order to ensure the validity of measurements.

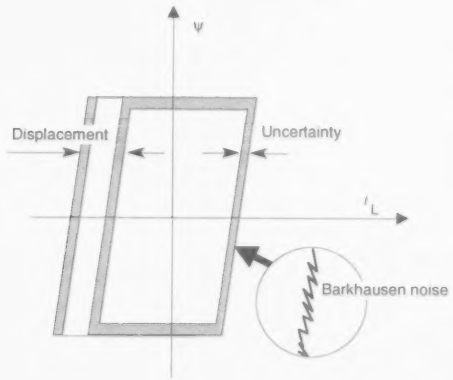

Fig. 49. Loop displacement vs magnetization loop uncertainty

Based on the studies of noise in magnetometers [28], [36 - 38] one can formulate several general rules for the core material selection:

1. The core losses must be minimal.
2. The material must have low magnetostriction
3. The material must have a low number of structural imperfections and low internal stresses
4. The material must have low coercive force

The following low-noise materials have most often been reported in regard to magnetometers, sensors and magnetic modulators: Ni-Mo permalloys, Co-based alloys, magnetic glasses, amorphous materials.

4.1.2. Operating temperature range

In many applications it is important to widen the operating temperature of an isolation measurement system. To make the coil operate at high temperatures it must have an adequate power handling capability. The latter is limited by wire loss, core loss and core geometry. For some core materials the type of encapsulating may be critical. If neither of these factors appear as a limitation first, the highest possible temperature will be defined by the Curie point. Ferromagnetic properties of a coil will deteriorate and eventually disappear when the temperature is approaching the Curie point (see Table. 4).

Table 4

Material	Curie point, °C
Fe	770
Co	1131
Ni	358
Manganese-Zinc ferrites	130 - 200
Nickel-Zinc ferrites	120 - 500
Supermendur	700
Square Permalloy	500
Metglas 2605	370

While there are always some magnetic cores with desireable characteristics operating at several hundred °C the electronic components used in a sensor circuit are much more restrictive. Commercial electronic components are currently available for temperatures up to 125 °C. However, progress has been made in recent years in high temperature electronics, and some 300 °C ICs are likely to appear in the near future. In the meantime it is likely that if the sensor is intended to work in a high-temperature environment not the coil but the electronic components will define the upper temperature limit.

It is interesting to note, however, that the isolation measurement system studied in this project can in fact be designed as a two part system. Because there are no active components to be placed on the measurement side it may be possible in some instances to implement the coil part as a remote probe with the rest of the circuit operating at a lower temperature. In this case the highest operating temperature of the probe will be set by the coil design and core material.

4.1.3. Power consumption

The coil excitation current must reach the saturation limits twice during each oscillation cycle. Therefore, in order to reduce power consumption we need to lower the driving current. This can be achieved by increasing the number of turns and/or choosing a magnetic core with a small coercive force.

4.1.4. Isolation voltage

The isolation voltage rating will be chosen as the least value from either the core encapsulation/coating rating or the wire isolation used. Even for small cores the isolation voltage can be made as high as 500 V.

4.2. Design examples

4.2.1. Basic low-frequency circuit

The basic experimental circuit of a current transducer with direct digital readout is presented in Fig. 50. The oscillator comprises a Schmitt trigger (operational amplifier LF356, R2, R3), a nonlinear coil (Hammond 640C transformer) and a current limiting resistor R1. The trigger output is directly connected to the 4 1/2 digital voltmeter (Fluke 87).

Because the circuit's operating frequency (1000-3500 Hz) is much higher than the voltmeter's sampling rate the readings will accurately represent the averaged output signal. The readout data in this circuit however is not available as an independent output signal.

A more practical modification of the basic low-frequency circuit is presented in Fig. 51. The Schmitt trigger output is connected to the second order low-pass Sallen and Key filter (U3, R5, R6, C1, C2). The output of U3 can be used for further signal processing.

It is demonstrated in the circuit of Fig. 51 that the filtered signal can be amplified (U2) and used in a feedback arrangement via an additional winding. Two feedback types were tested. In the first circuit the feedback winding is grounded while the second circuit uses an additional comparator (U5). The second type of feedback allows a substantial increase in the total amplification factor of the feedback, especially for small input signals.

Fig. 50. Basic low-frequency current sensor

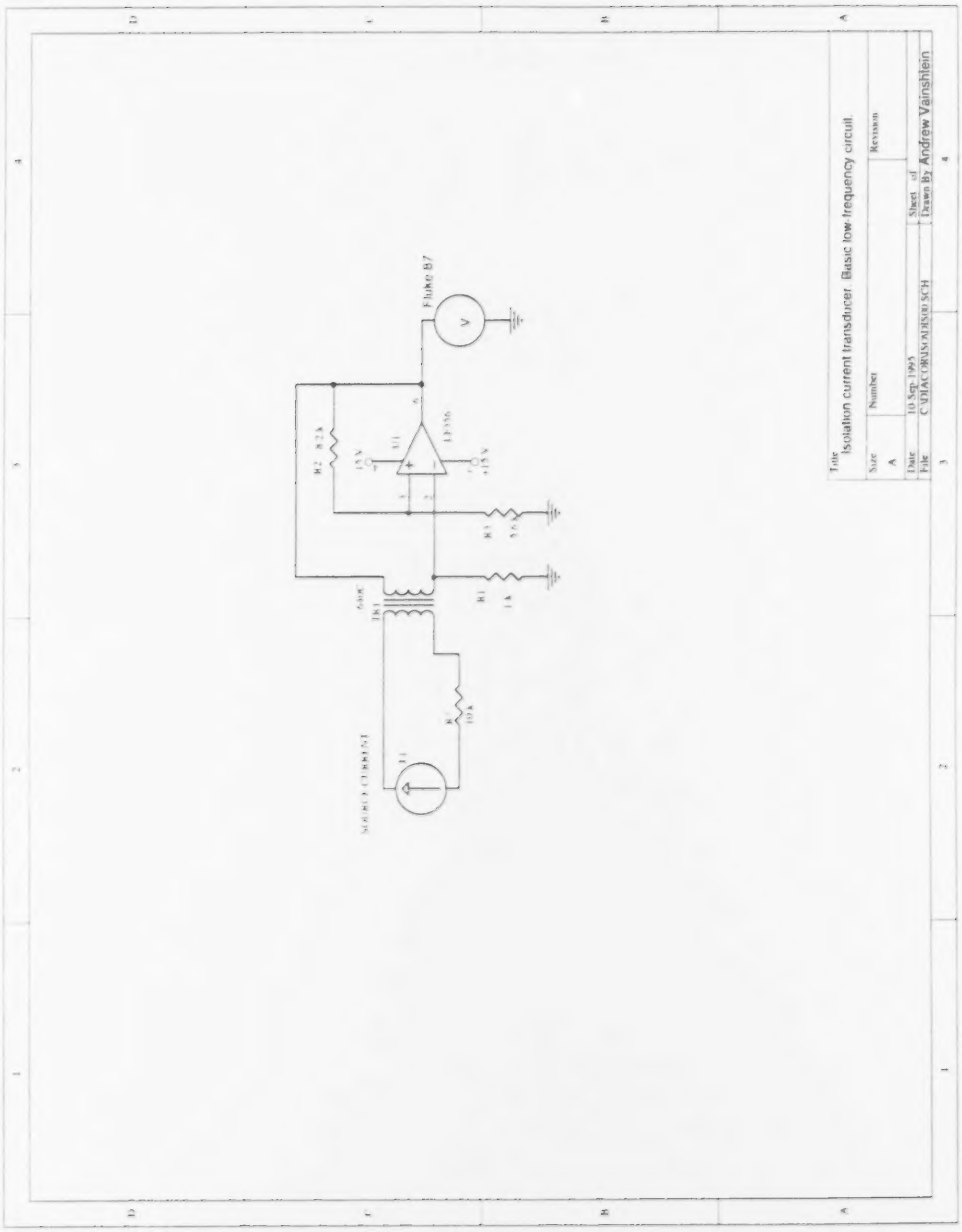

Fig. 51. Basic low-frequency current sensor with output filter and feedback

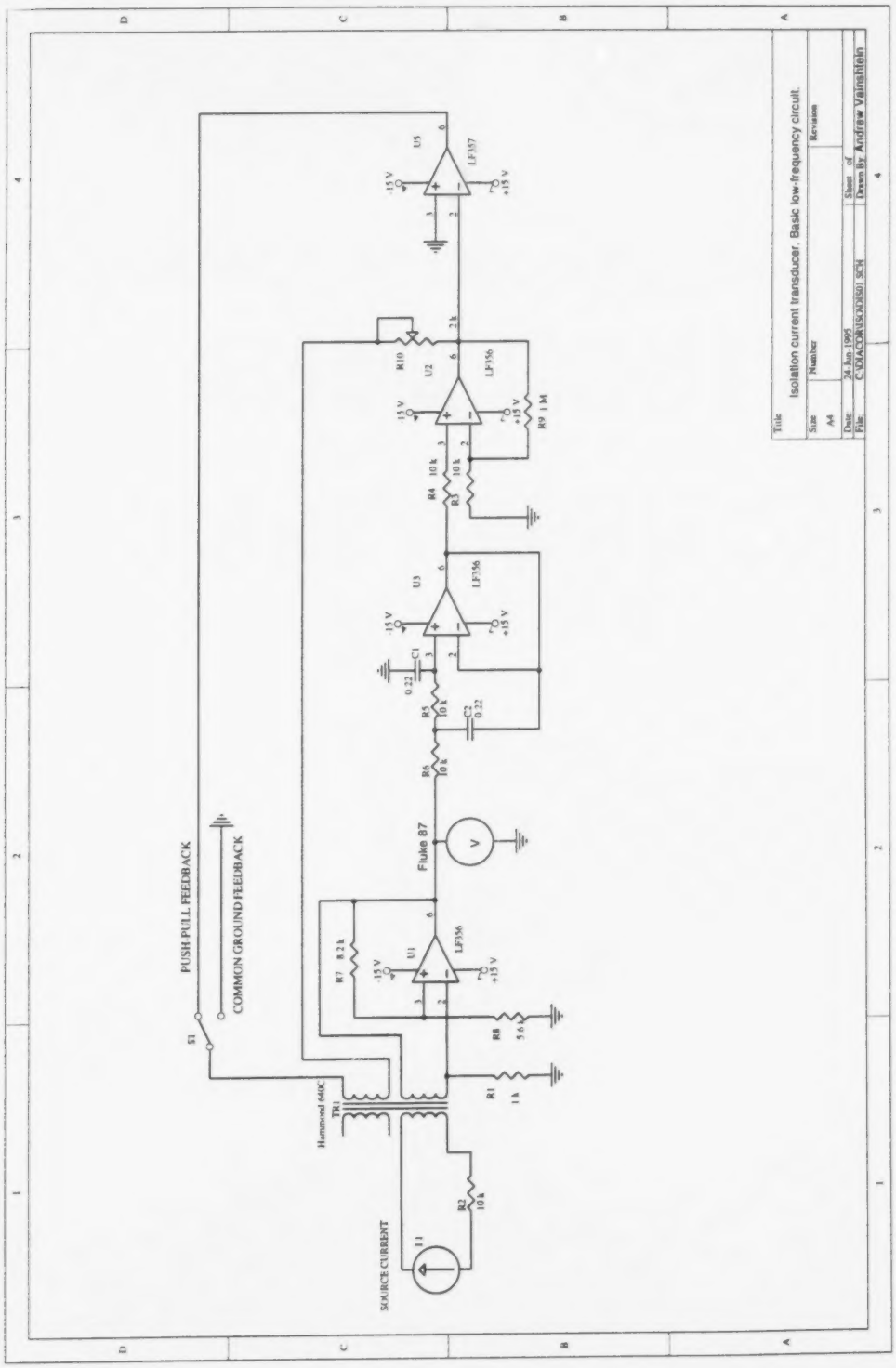

4.2.2. Basic low-frequency circuits experimental results

The low-frequency circuits given in Fig. 50, 51 were assembled and tested using a Fluke 87 digital multimeter, Tektronix 2430A digital oscilloscope with GPIB and a Hewlett-Packard 7470A plotter. This allowed measurement of all input-output characteristics of the circuit and a direct printout of results.

The coil current waveforms measured across the current limiting resistor are presented in Fig. 52 and 53 for dc and ac input currents. In accordance with our previous analysis, when the coil approaches saturation the slope of the current significantly increases showing almost vertical growth. The change of the current in the near saturation region is so fast that in Fig. 53 the amplitudes appear modulated by the ac input signal. In fact this effect is due to the limited sampling rate of the digital oscilloscope 'missing' sharp ends of the current waveform.

Averaged/filtered output voltage versus dc input current is presented in Fig. 54 for the coil 5-8 of the transformer used (Hammond 640C). These characteristics were obtained for an open loop circuit. The circuit allows us to measure an input current from -5 to +5 mA with sensitivity ~150 V/A. Linearity of the circuit is better than 2 % for input currents from 100 μA to 2 mA and from -100 μA to -2 mA but quickly deteriorates in the near zero region and also for large (>2 mA) currents.

Addition of the feedback leads to the considerable linearization of the output characteristic especially in the 2-5 mA current range that is shown in Fig. 55. The improvement of the small signal characteristic in the range of -55 μA to +55 μA due to the influence of noise is less effective. The small signal characteristic is presented in Fig. 56. The characteristic also demonstrates an offset ~2 mV.

In accord with our previous analysis (see Fig. 12) the oscillation frequency shown in Fig. 57 demonstrates a minor parabolic-type modulation by the input current.

Fig. 52. Experimental coil current waveforms for low frequency current sensor and dc input current

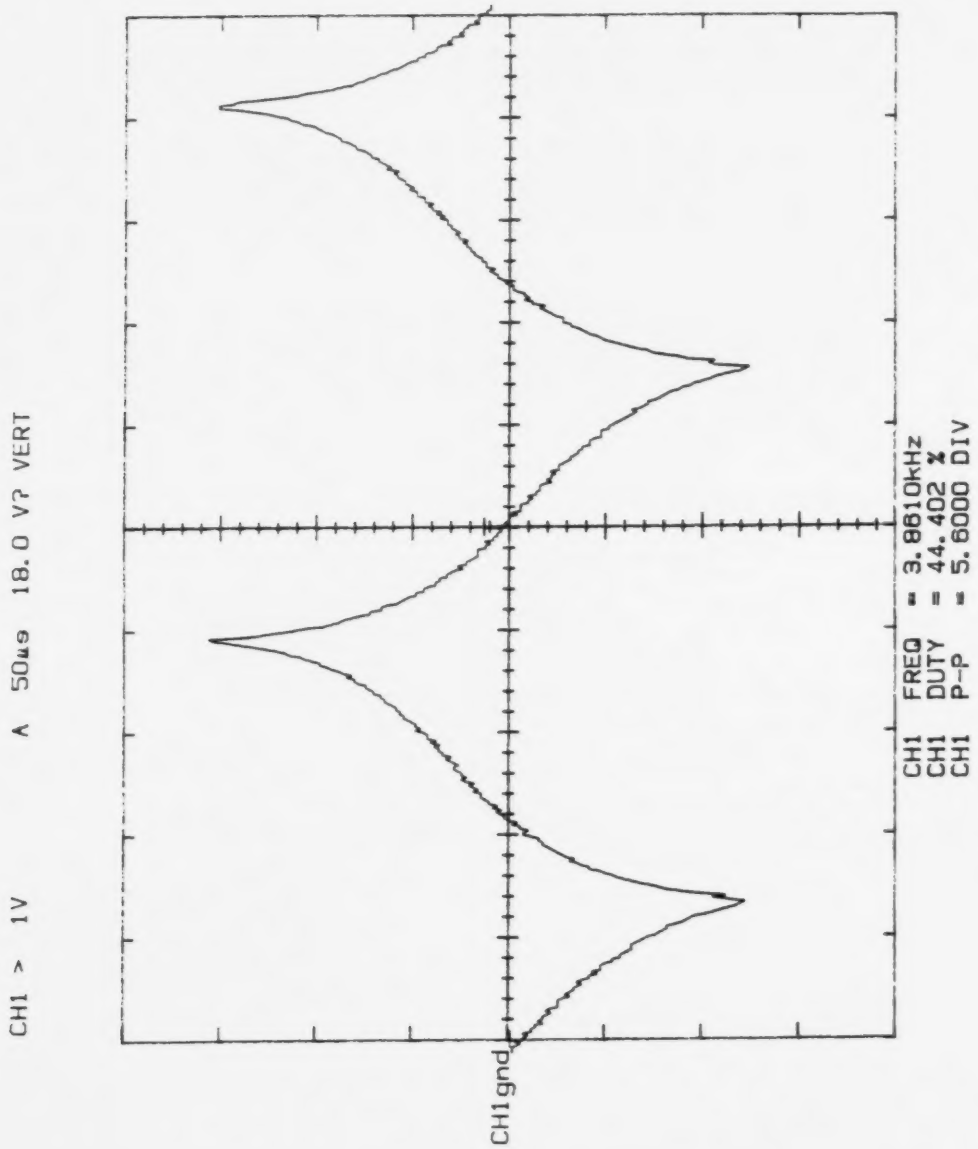

Fig. 53. Coil current for ac input current (low-frequency current sensor)

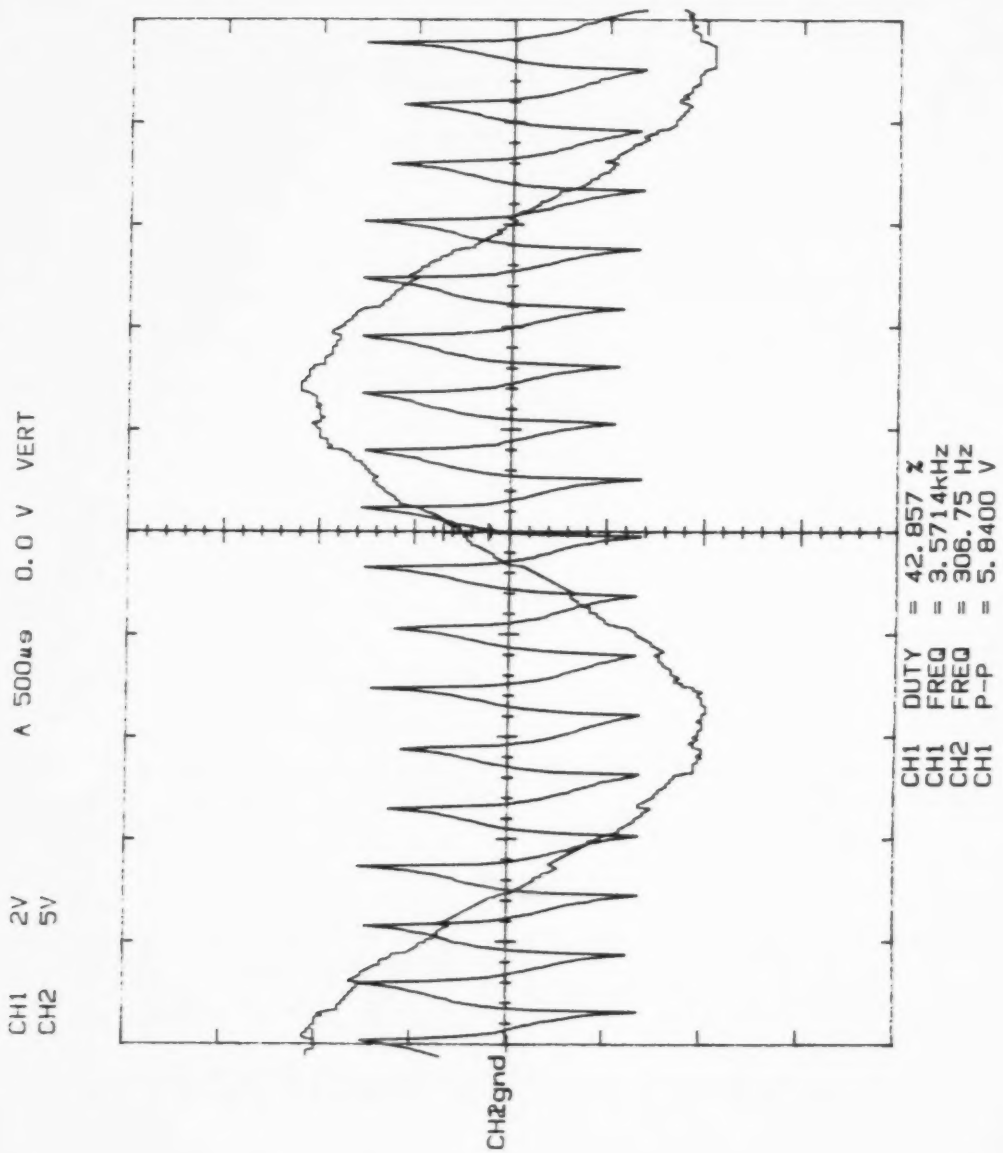

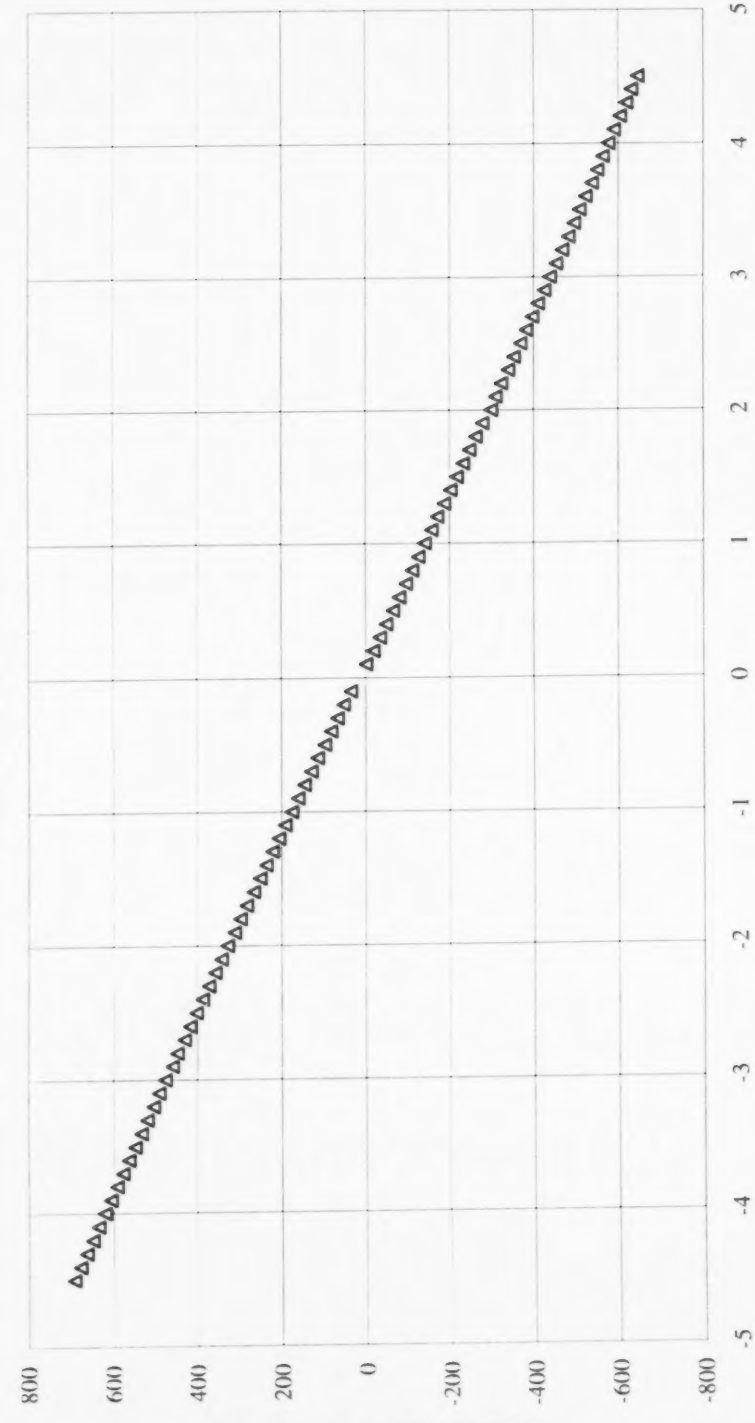

Fig. 54. Experimental output characteristic of the low-frequency isolation current sensor without feedback (dc input current)

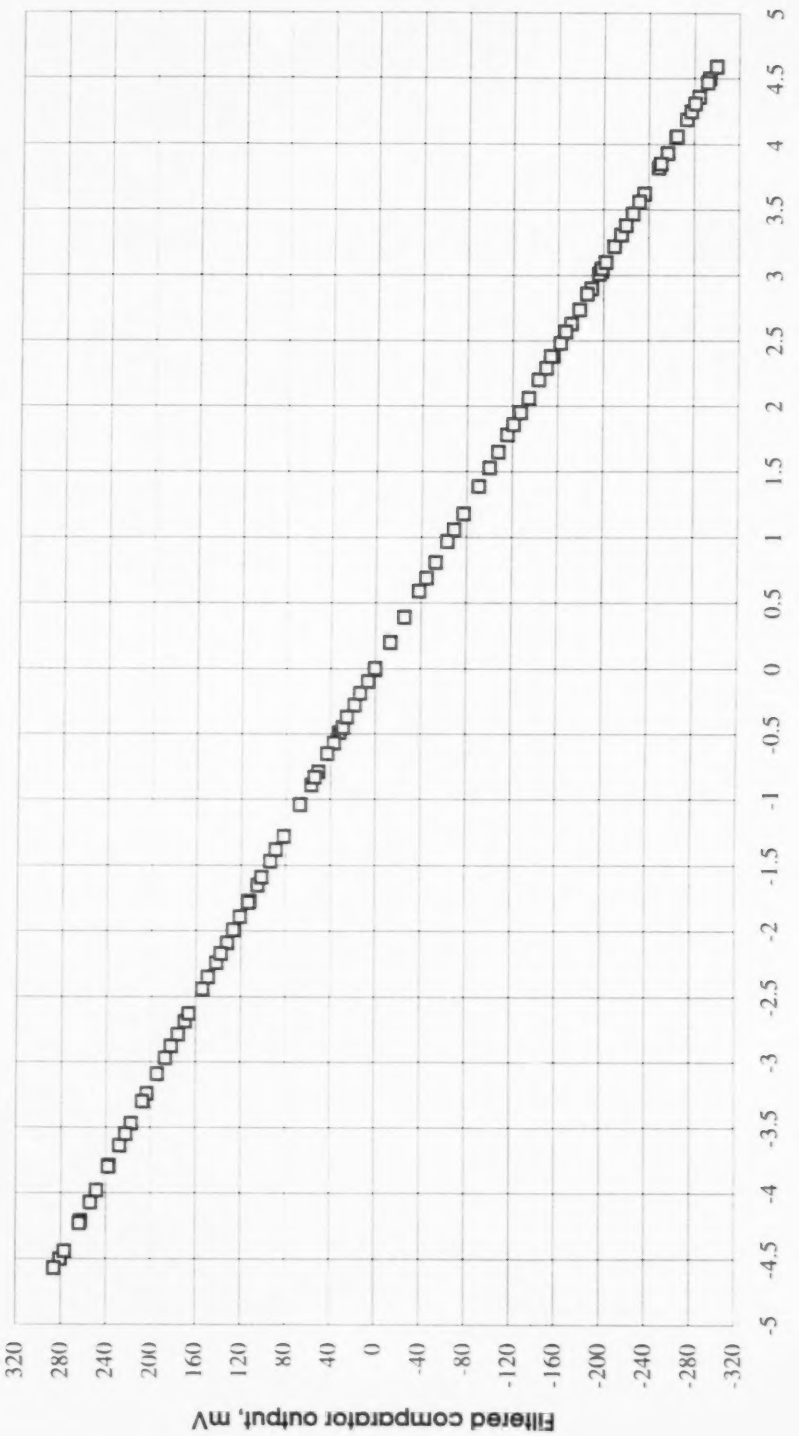

Fig. 55. Experimental large-signal output characteristic of the current sensor with feedback

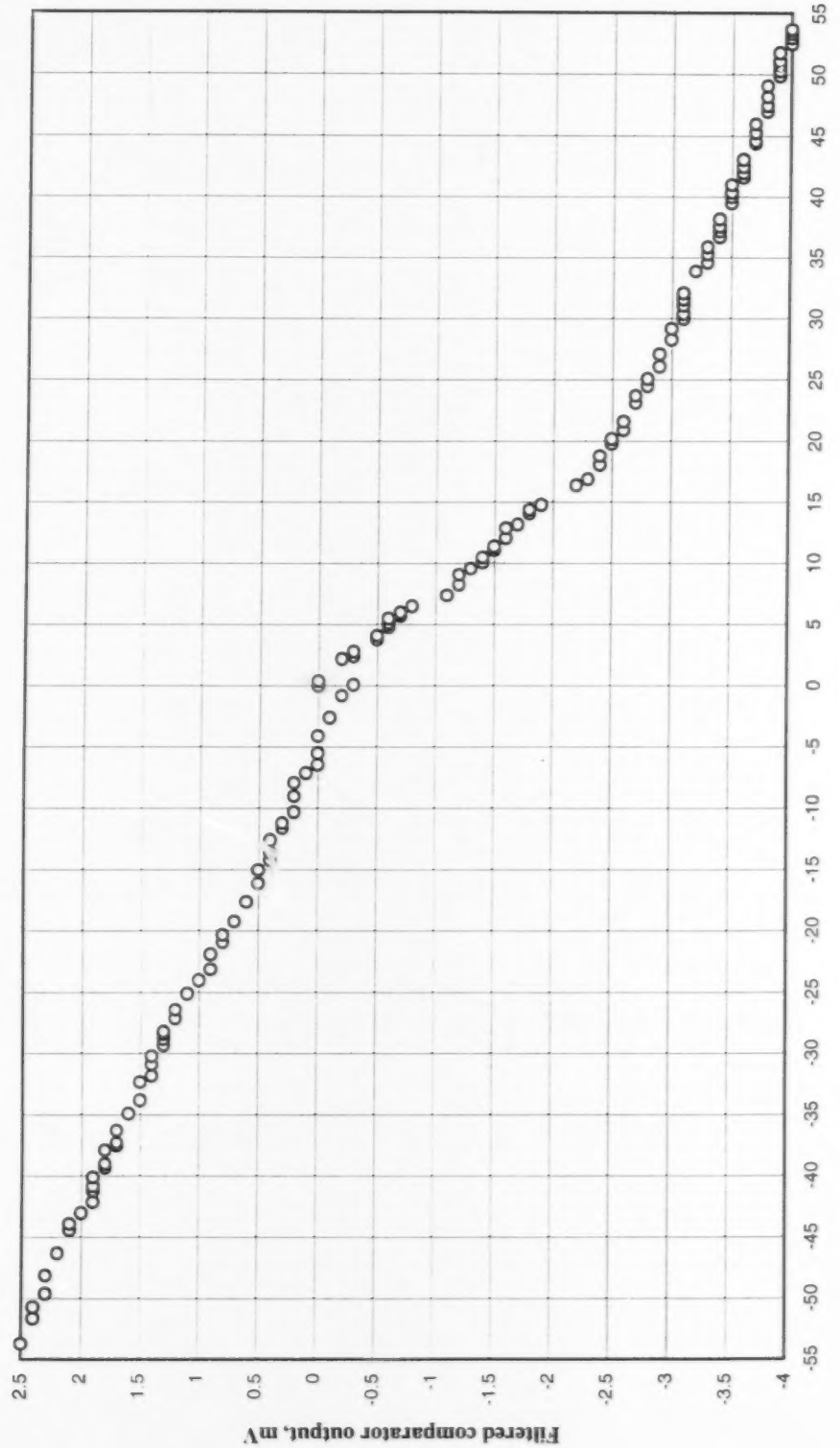

Fig. 56. Experimental small-signal output characteristic of the current sensor with feedback

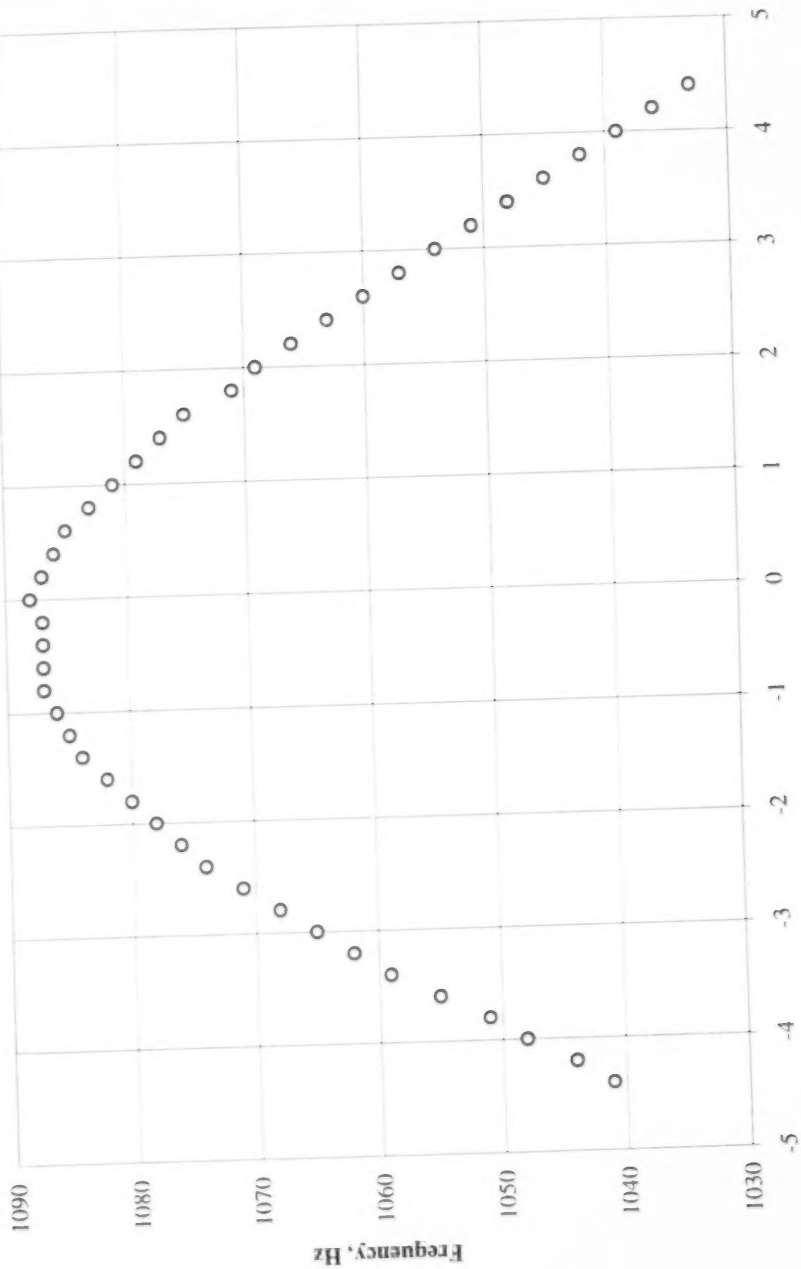

Fig. 57. Oscillation frequency of the current sensor as a function of input current

4.2.3. High frequency isolation current measurement circuit

The high frequency isolation measurement circuit was designed and tested using the INTEGRATOR-S/H structure (Fig. 58). The circuit employs two of the concepts described in Chapter 3. Specifically, the circuit utilizes the leading sampling that provides a high speed S/H operation. Additionally, in order to reduce the dead zone effect the circuit uses truncated integration times.

Similar to the low-frequency transducer structure (Fig. 51) the high frequency version has a Schmitt trigger (U1) switching to HIGH or LOW depending on the coil current crossing of the reference levels. But unlike the previous circuit the output of the trigger is not connected directly to the coil but instead is used as a synchronization signal for a digital TIMING UNIT.

The digital TIMING UNIT consists of four mono-stable multivibrators IC U9, U10, U11 and NOR U8. According to the timing diagram presented in Fig. 59 the above ICs generate four digital signals: $\pm V_{0M}$ CONTROL, INTEGRATOR HOLD, RESET, SAMPLE. $\pm V_{0M}$ CONTROL is used for switching the amplifier U3 from inverting into noninverting mode and vice versa. As a result, the voltage supplied by the reference source D2 through the follower U2 is converted into V_{0M} or $-V_{0M}$.

The voltage $\pm V_{0M}$ is further applied to the coil's driving winding and to the inverting INTEGRATOR formed by U5, R17, R18 and C6. At the beginning of each integration cycle the INTEGRATOR is reset by the RESET signal switching the S4 ON. The INTEGRATOR is switched to the HOLD mode each time the S2 switch controlled by the INTEGRATOR HOLD logic level is OFF. This mode is used for cutting off the integration times inside each oscillation half-cycle by the equal time intervals.

The output of the INTEGRATOR is passed to the S/H formed by U4 and C7 with the input switch S3 controlled by the SAMPLE digital signal. The S/H output signal as

shown in Fig. 59 holds the INTEGRATOR level as reached at the end of the previous oscillation cycle thus providing the true $T^+ - T^-$ operation.

The S/H is connected to the differential amplifier formed by U6, R4, R5, R21 and R22, with independent offset control provided by U7. This arrangement is used for the feedback loop using an additional coil winding.

Fig. 58. Schematics of the current transducer for 25-50 kHz operating frequency

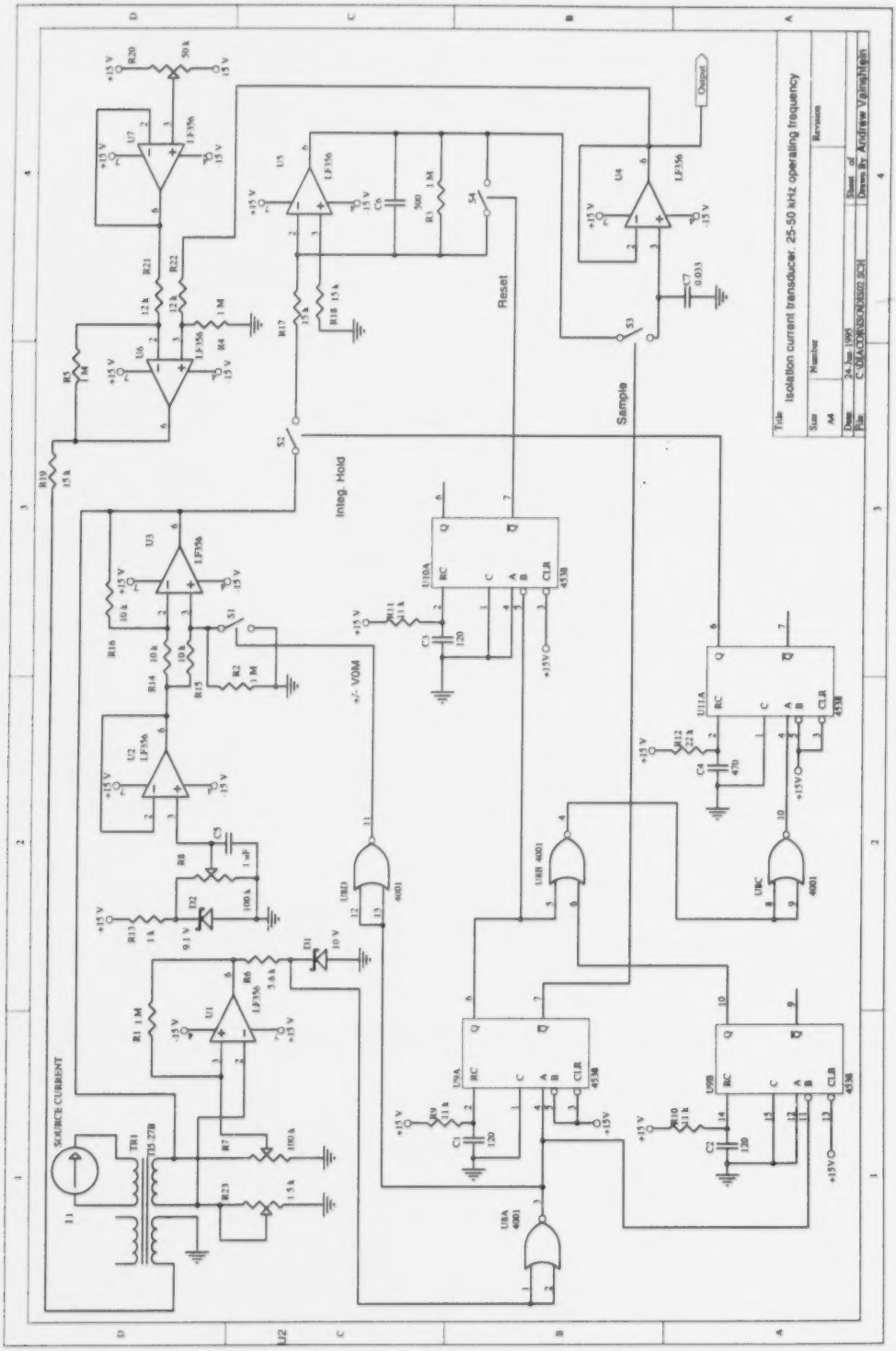

Fig. 59. Timing diagram of the current transducer for 25-50 kHz operating frequency

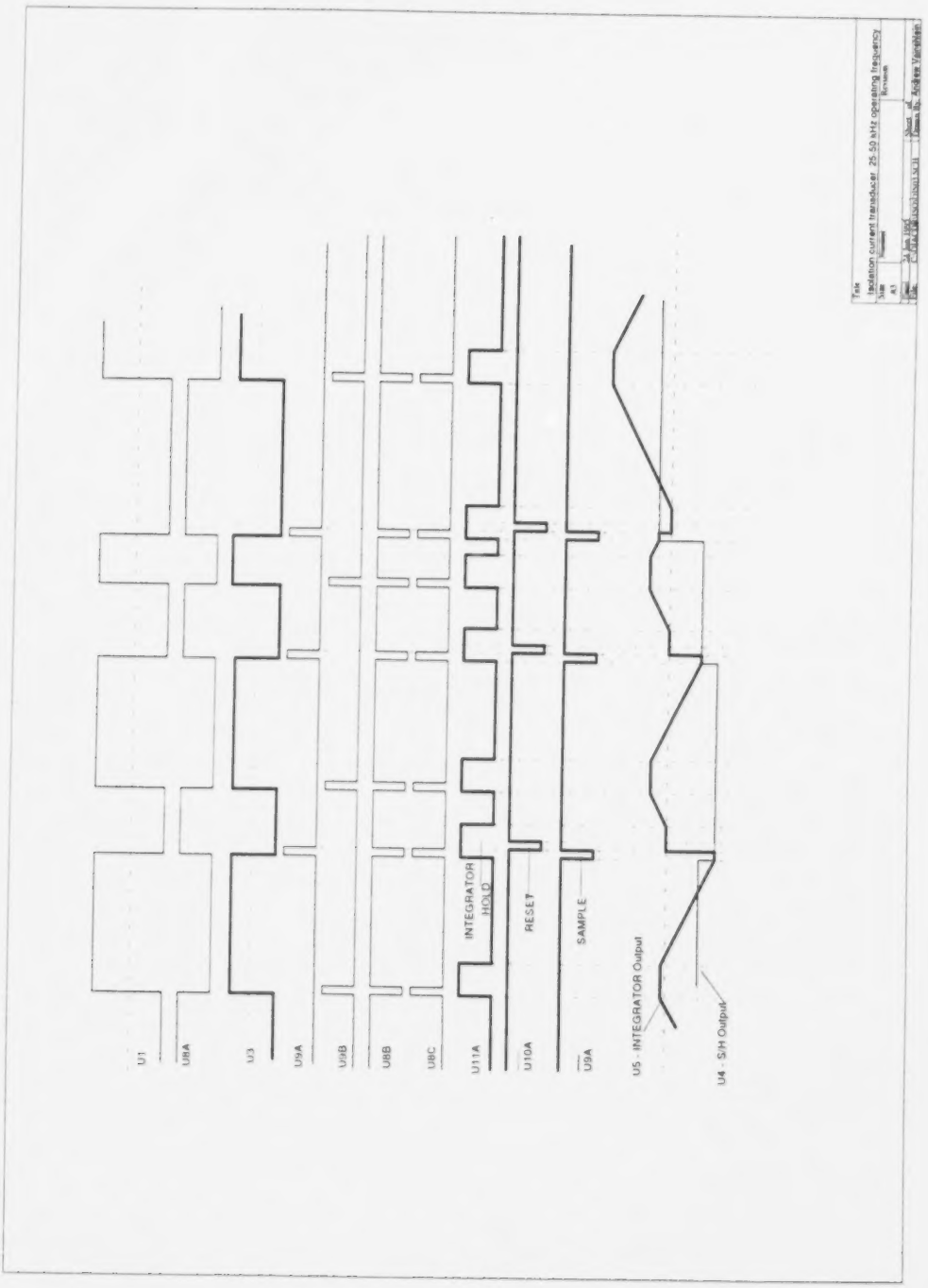

4.2.4. High frequency circuit experimental results

The circuit presented in Fig. 58 was experimentally studied with special attention given to the tuning procedure. Since both the coil driving current and the feedback determine the circuit performance the effect of these two factors will be shown below.

For the open loop circuit (no feedback) and rms driving current 2.5 mA the input current from -2.3 to +2.3 mA is converted into +4.5 - 4.5 V output signal. The sensitivity of the circuit is 8-10 higher than that of the circuit with direct filtering. However, the output characteristic presented in Fig. 60 demonstrates both low linearity and large hysteresis.

Addition of the feedback as shown in Fig. 61 leads to significant linearization of the output characteristic but has a minor effect on hysteresis in the near zero region.

According to the model proposed in 2.3.4 the hysteresis in the output characteristic may result from remanent magnetization of the core material when the driving ac current is insufficient in value. This model was effectively supported during the experimental study. The increase of the driving current results in suppression of the hysteresis effect (see Fig. 62) which can be practically zeroed for > 5 mA.

The combination of the higher driving current and active feedback results in the output characteristic presented in Fig. 63. The circuit provides 0.08 % linearity for the input current from -2.2 to + 2.2 mA excluding the near zero region ±200 μA where the nonlinearity error can reach 4 %.

The frequency response of the 25 kHz isolation measurement circuit is presented in Fig. 64. This characteristic is practically flat up to 1500 Hz.

Fig. 60. S/H output signal for 25 kHz current sensor without feedback (dc input current)

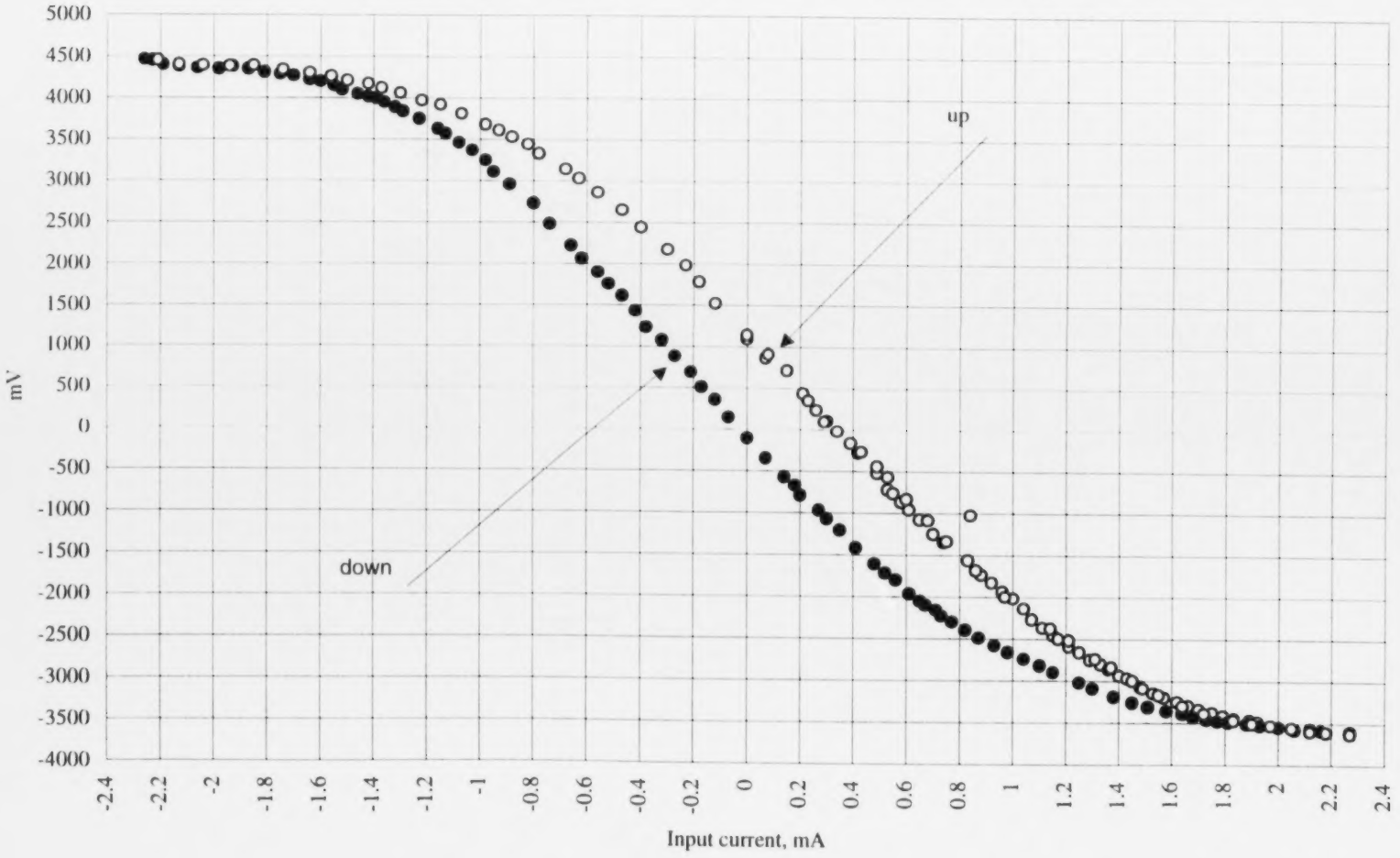

Fig. 61. S/H output signal for 25 kHz current sensor with feedback (i_L = 2 mA)

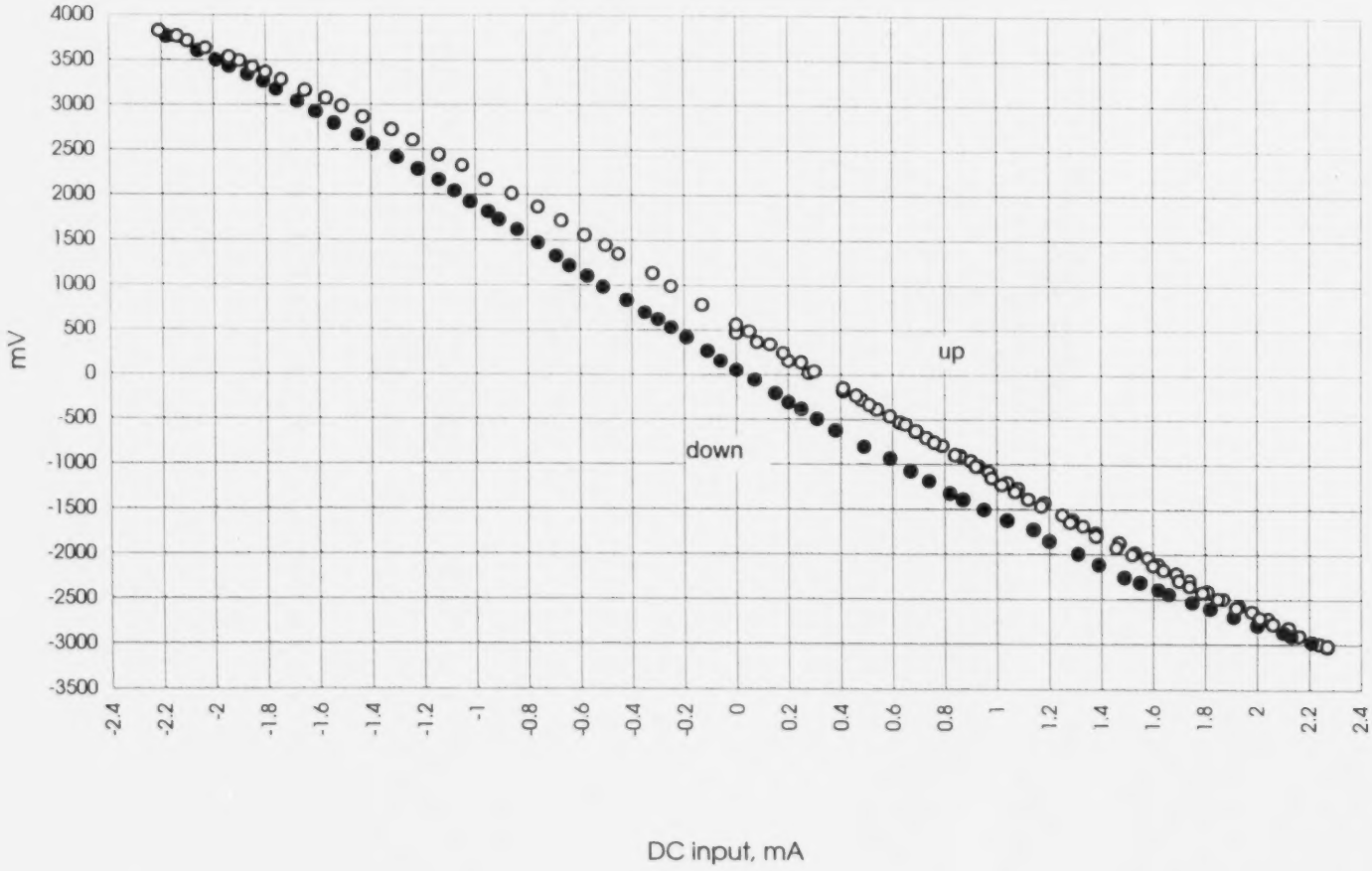

FIG011A Chart 9

Fig. 62. Hysteresis of the current sensor as a function of driving current

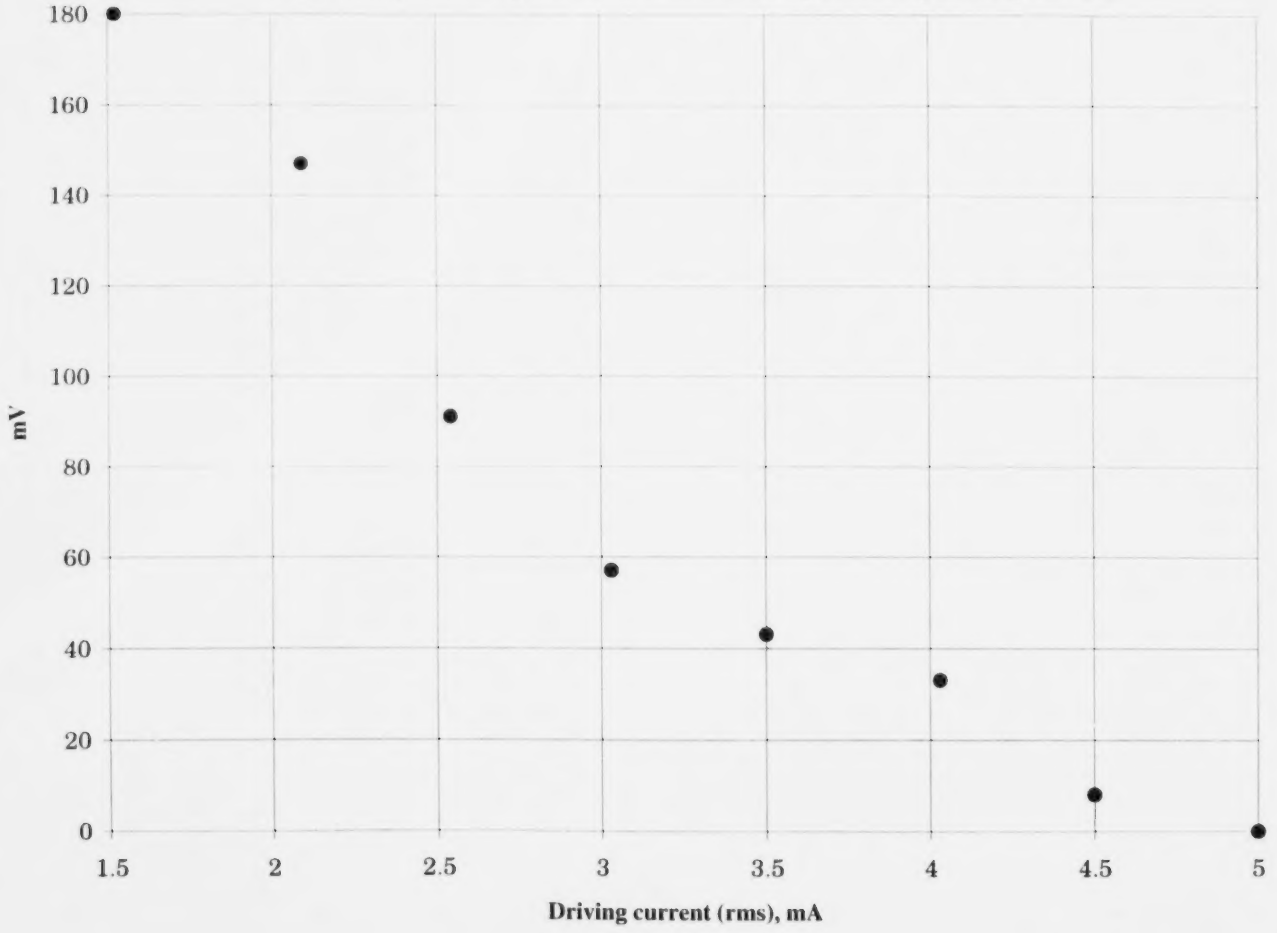

FIG011 Chart 1

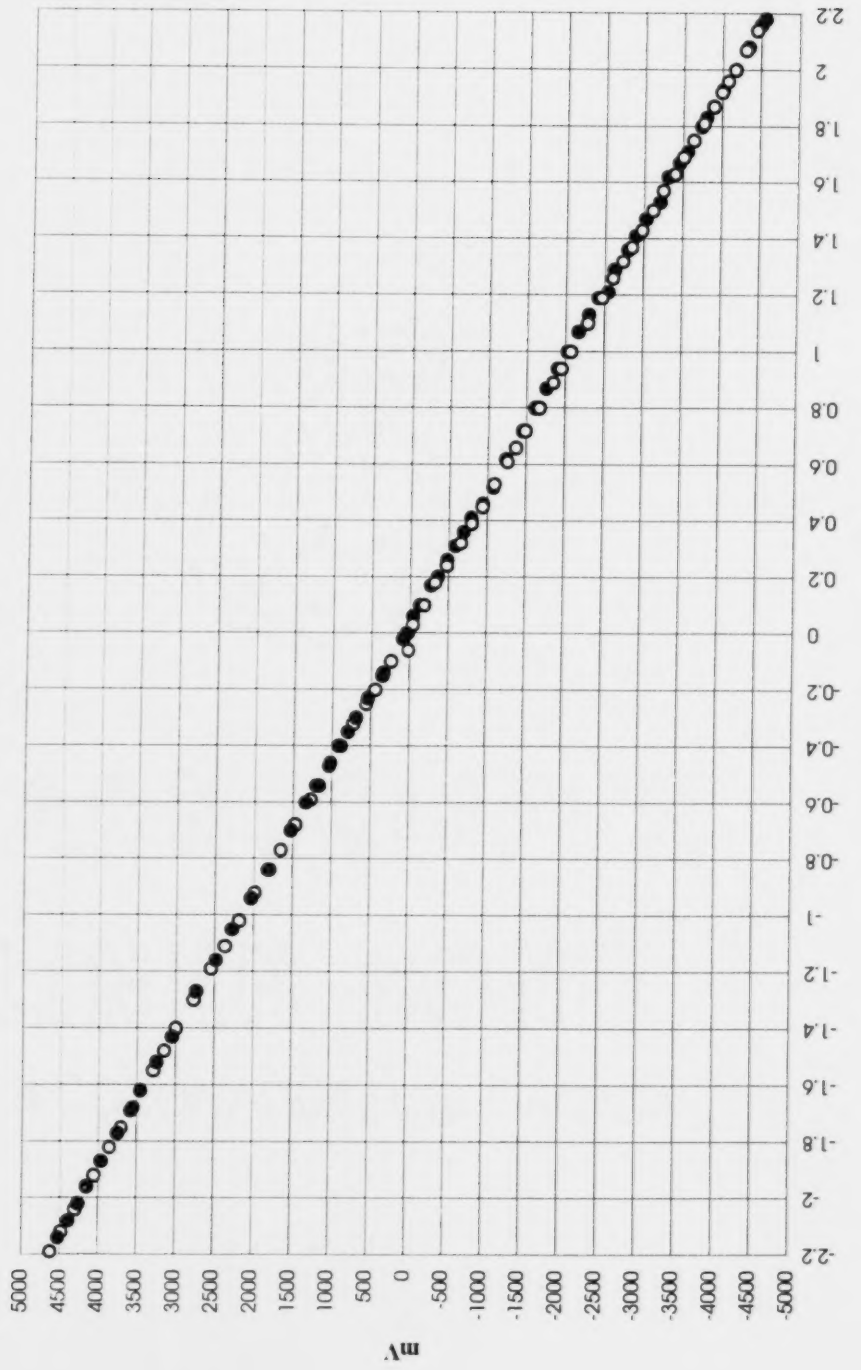

Fig. 63. S/H output of the current sensor with feedback and hysteresis suppression
i_L = 5 mA, f_d = 24.8 kHz

FIG011 Chart 4

Fig. 64. Frequency response of the isolation current sensor (f_d = 25 kHz)

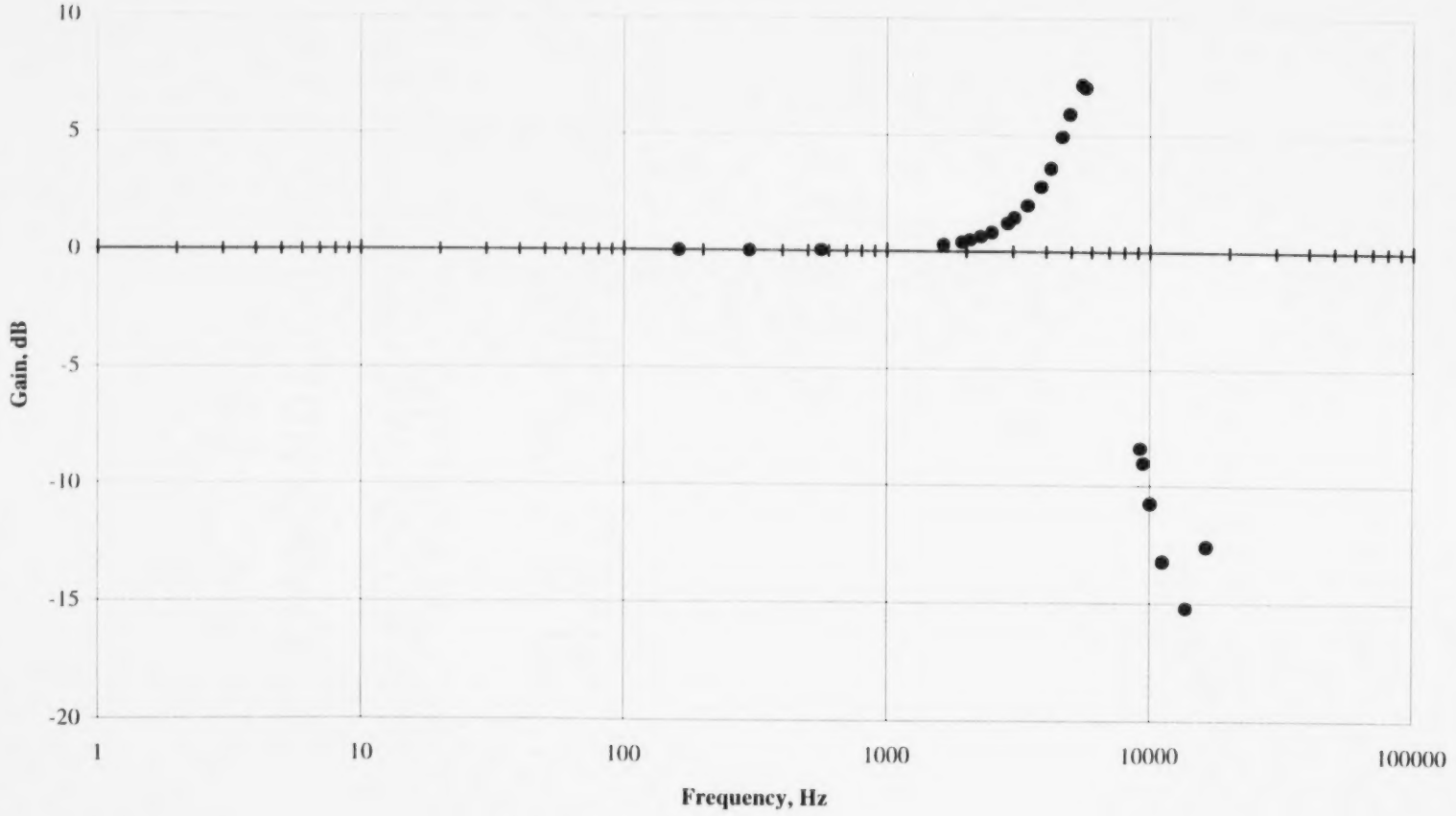

4.2.5. Circuits with dead zone reduction

The concept of a dead zone reduction (DZR) outlined in the section 3.2.4. was experimentally studied using two circuits presented in Fig. 65 and Fig. 66. An additional DZR unit incorporated into each circuit is used for boosting the coil current while it passes the dead zone.

In the first version as shown in Fig. 65 the Schmitt trigger directly drives the coil. The circuit includes an additional window comparator U1B, U1C, U2A controlling the level of the stabilized Schmitt trigger output. When the coil current is inside the region predefined as a dead zone $\pm V_{DZ}$ the window comparator turns the analog switch S1 OFF. This brings the trigger output to the high level $\pm(V_{Z1} + V_{Z2} + 2V_d)$ and results in a very fast coil transition through the dead zone.

When the current leaves the dead zone the switch S1 is turned ON which excludes the $\pm V_{Z2}$ from the trigger output. Consequently the trigger output becomes $\pm(V_{Z1} + 2V_d)$ which results in a stepped characteristic shown in Fig. 65(b).

The circuit with a DZR unit can be combined with independent switcheable $\pm V_{0M}$ sources as presented in Fig. 66. The circuit employs an array of analog switches S1-S6 and the window comparator. When the coil is in the dead zone the voltage applied to the driving winding is ±10 V that results in a very fast recharging of current in the coil. Outside the dead zone this voltage is set at ±2 V.

Fig. 65. Current sensor with dead zone reduction: (a) direct comparator control, (b) $\pm V_{0M}$ vs. coil current

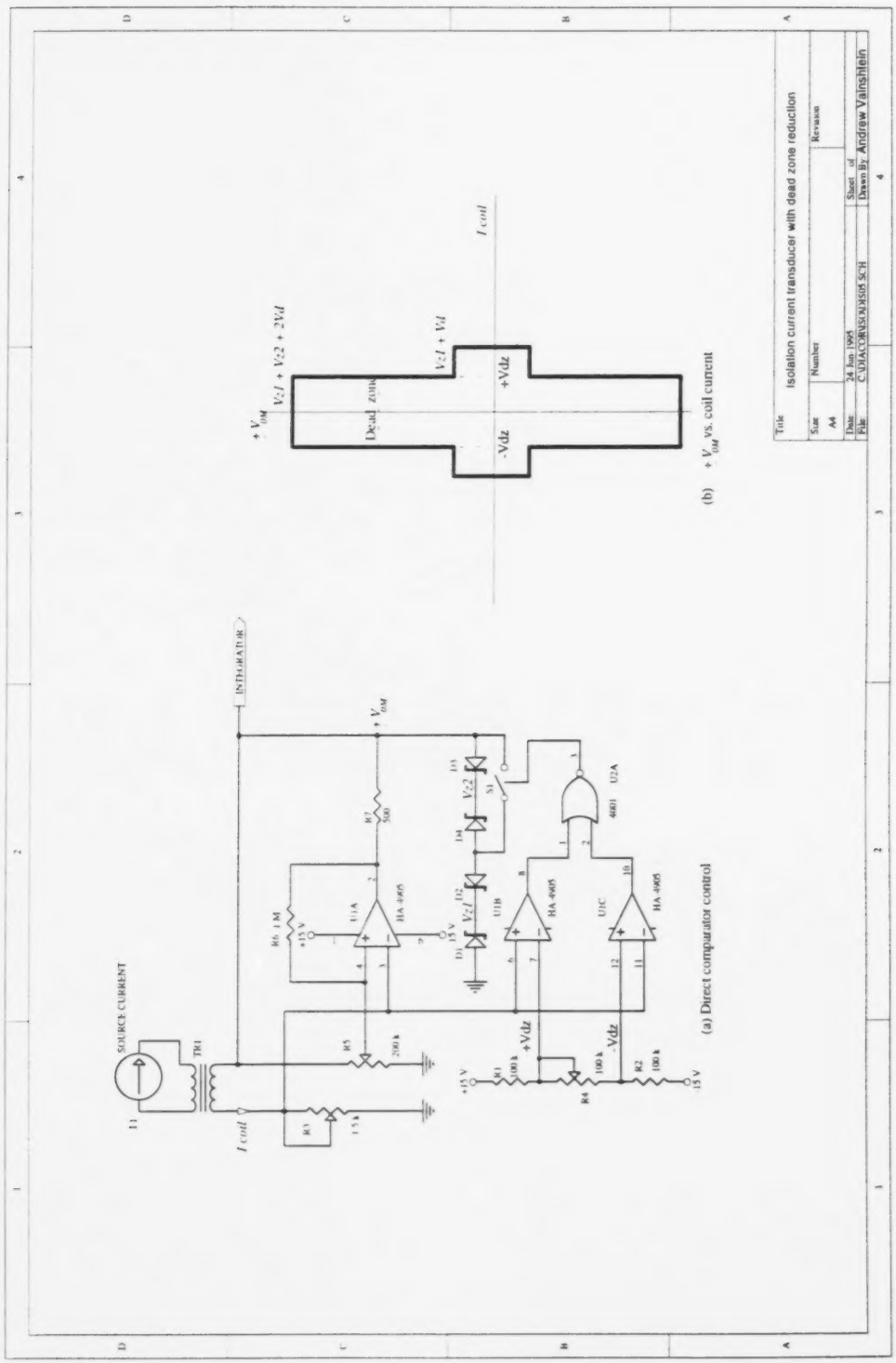

Fig. 65. Current sensor with dead zone reduction designed with additional excitation voltage sources

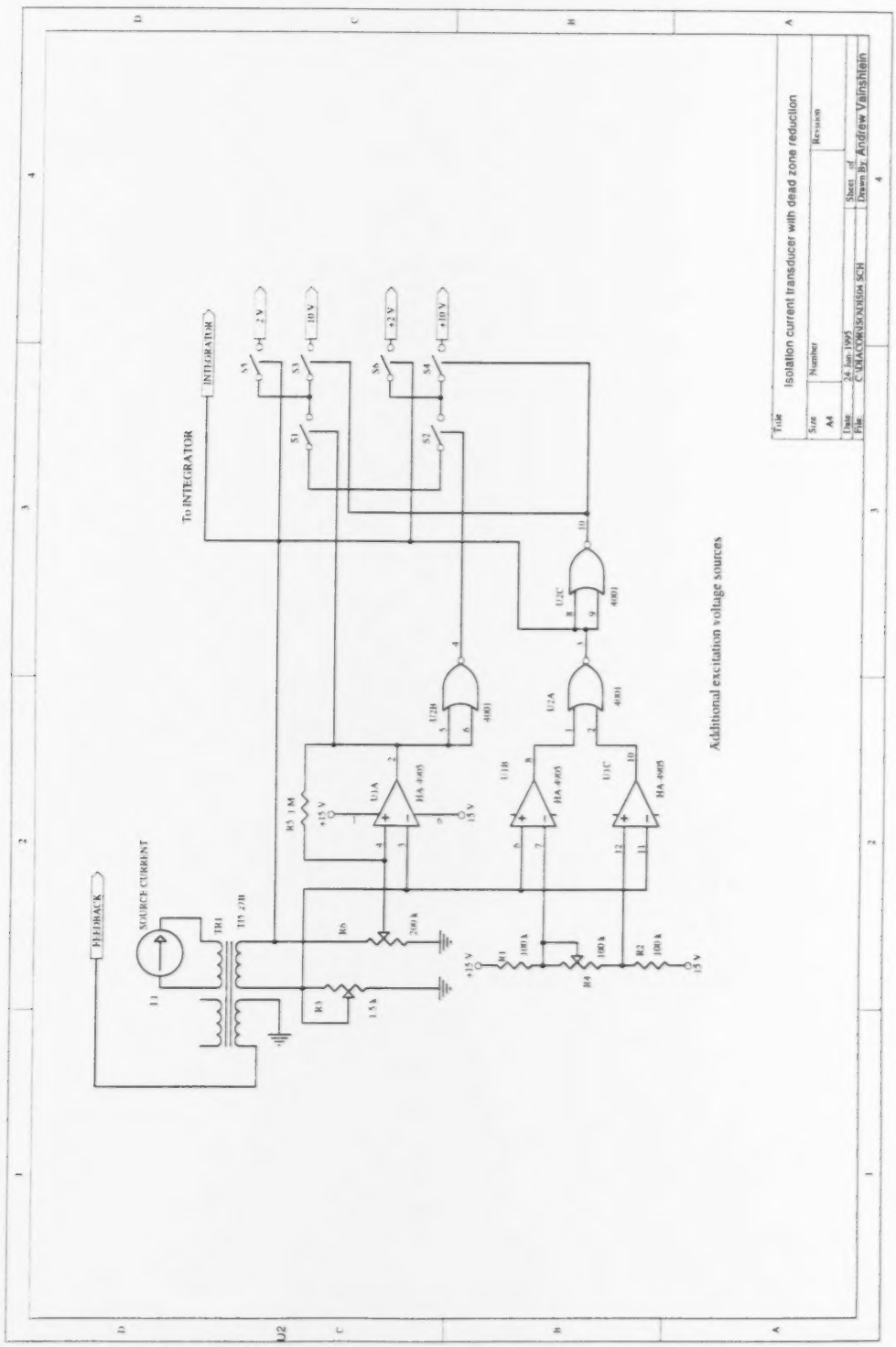

4.2.6. Experimental results for the circuit with DZR

To experimentally determine the correct dead zone limits the reference levels of the DZR unit $\pm V_{DZ}$ were symmetrically increased; simultaneously the sensor output was measured under the stable input current condition. The dead zone limits were set at the points at which the sensitivity was just starting to decline.

As shown in Fig. 67 the above tuning procedure allows us to increase the operating frequency from 25 to 63 kHz without any significant loss of sensitivity for the same experimental transformer. Fig. 68 presents the evolution of the sensitivity for different output characteristics and oscillation frequencies from 25 to 81 kHz. Sensitivity decline for higher than 63 kHz frequencies can be explained as a result of nonlinear regions of a magnetization characteristic being partially included into the fast charging mode.

Fig. 67. Output characteristics of the isolation current sensor with DZR

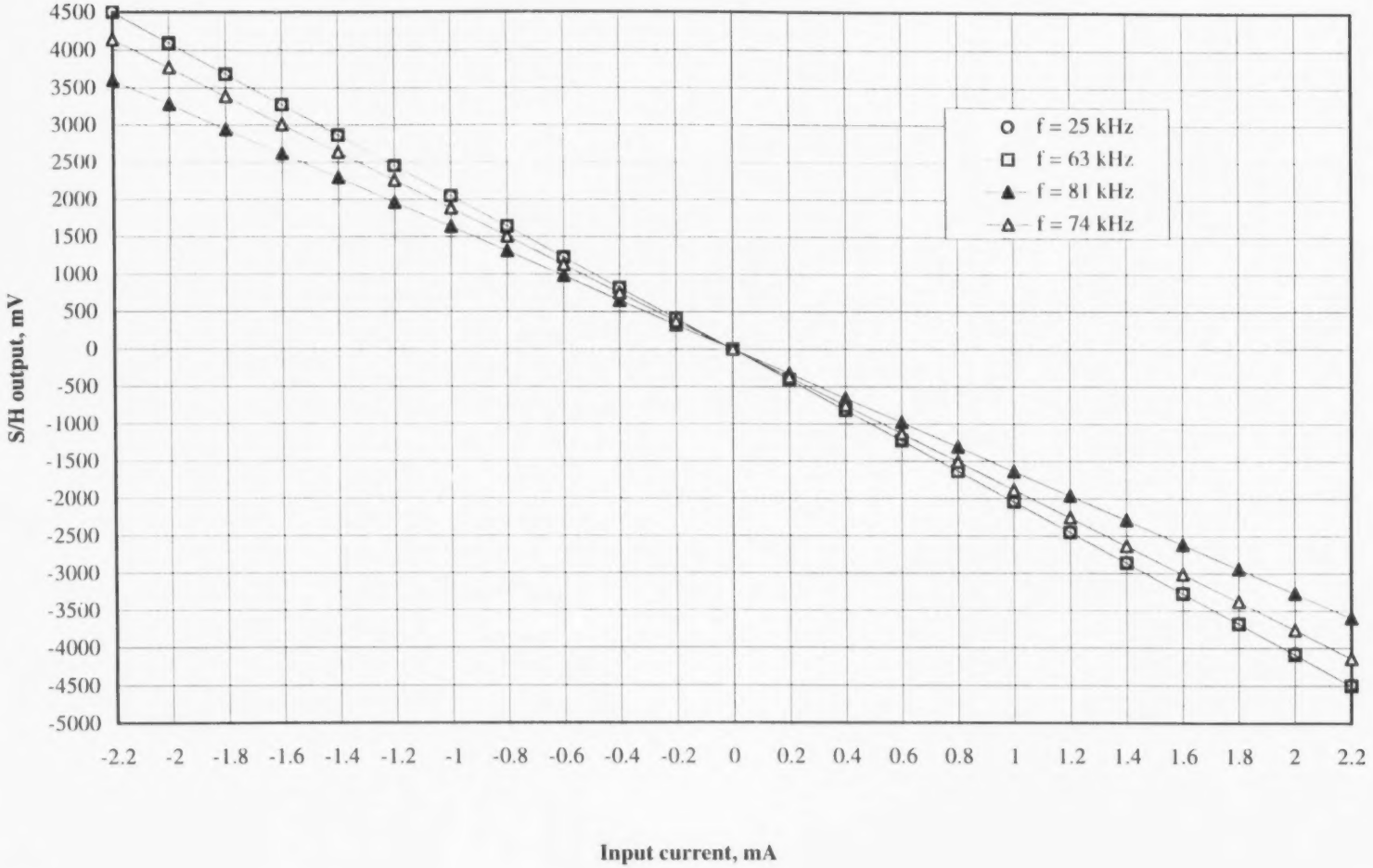

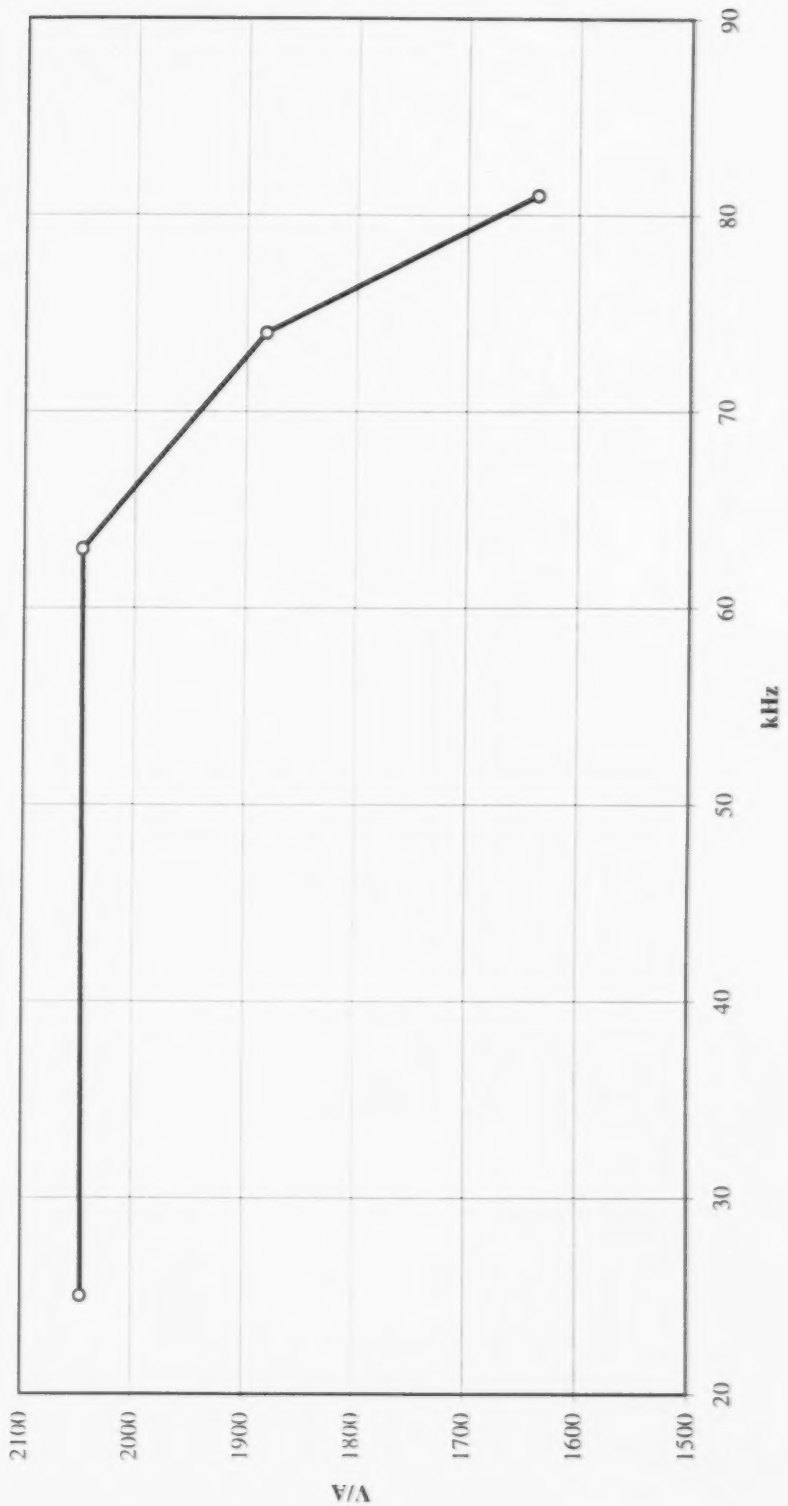

Fig. 68. Sensitivity of the isolation current sensor with DZR as a function of oscillation frequency

4.2.7. IC digital processor for the isolation current transducer

A specialized two channel digital processor IC based on the up-and-down counter with output latch memory was designed and implemented using Actel CMOS FPGA. The operation of the digital processor was described in 3.4. Appendix 2 presents the modular and detailed schematics of the designed chip.

Each of two channels consists of the following sub-units: **Countunit** , **Timing unit**, **Latches**. **Countunit** is a 12 bit up-down synchronous counter which contains 2 subunits of **Rev_counter** and 1 subunit of **Stage2_counter.**

With each positive edge of the input signal (taken from the current sensor COMPARATOR) the **Timing unit** provides one strob signal for **Latches**. This short pulse signal switches the **Latches** into a sampling mode. During this pulse the **Latches** memorize the output of the **Countunit.** At all other times the latches are in a hold mode. Right after sampling the **Timing unit** provides the setting of the **Countunit** in "0" state.

Latches sample and keep the number equal to the measured difference between $\mathbf{T^+}$ and $\mathbf{T^-}$ during the next measurement cycle.

4.2.8. Testing of the IC

The designed IC was tested using the **Lsim** computer simulation package and **IMS**. During functional tests the following characteristics were verified:

1) The IC can be set/reset through the asynchronous **Reset** input

2) The count can be stoped via **Enable** input

3) The circuit performed subtraction of the half-periods of the input signal.

The **Maximum operating frequency** was tested with IMS and found to be 7.7 MHz for the signal with 50 % duty cycle (NZR) type.

4. 3. Concluding remarks

Several different sensor circuits for the studied isolation current measurement system were designed and tested.

A low-frequency experimental sensor for the frequency range 1000-3500 Hz was designed using the basic current sensor and a second order low-pass filter. The nonlinearity of the sensor for high level signals is 2 %.

A 25 kHz experimental current sensor was designed using a high-frequency pulse transformer. The circuit uses the concept of dual integration with the output S/H and leading sampling. The nonlinearity of the circuit with feedback is 0.08 % for input current range ±(0.2 - 2.2) mA. The bandwidth of the sensor is about 1500 Hz.

A circuit with dead zone reduction was tested. An increase of operating frequency from 25 kHz to 63 kHz was achieved without decline of sensitivity.

It was experimentally verified that setting a higher driving current can serve as an effective way to eliminate the hysteresis from the output characteristics.

All experimental current sensors demonstrated substantial increase in nonlinearity for small input signals. This increase can be accounted for by the noise characteristics of the transformers used in the study.

A concept of digital processing was tested with a help of an experimental FPGA CMOS IC. The designed circuit provides direct digital processing of the low-frequency sensor output signal. The IC provides 12 bit conversion accuracy when working with 1000 Hz current sensor.

5. Conclusion

This thesis is aimed to further study the class of isolation current sensors proposed by Filanovsky, Piskarev and Taylor. These circuits provide an interesting opportunity to achieve some important measurement goals using a relatively simple circuit principle. The basic current sensor can comprise only OA, small transformer and three resistors. Nevertheless, as was demonstrated by the above authors, this simple circuit can provide a quite accurate conversion of the input current into the pulse-width modulated output signal.

The nonlinear coil operation is a key to understanding the sensor performance. Both piecewise linear and polynomial models describing the coil magnetization were previously studied. This thesis expands the list of magnetization models by adding the linear-saturable model (both with and without hysteresis) and piecewise model with an arbitrary number of segments. The output signal components obtained from the polynomial model were studied. The methods of achieving the maximal linearity and sensitivity were proposed based on the different types of formatting the above components. The application limits for the presented magnetization models were discussed with references to particular ferromagnetic materials and their properties.

The circuit analysis performed with the help of above magnetization models provided expressions for the duty cycle and frequency of the sensor output. Sensitivity and bandwidth of the transducer were shown to be dependent upon fundamental magnetization properties such as magnetic permeability, saturation limits for both B and H, and magnetization loop hysteresis. These results were used in the sample calculations which were performed for several real magnetic materials.

The basic current sensor circuit was simulated using the PSpice program. This analog simulation qualitatively supported all main results obtained by the linear-saturable, piecewise and polynomial models. The output characteristics of the current sensor obtained from the PSPICE and from the polynomial model were compared and

appeared quite close to each other. It should be noted that the magnetization analysis in the PSPICE is based on the numerical Jiles - Atherton model and therefore, can be considered as an independent control.

The previously published results were concerned only with the type of multivibrator control based on the measurement of coil current. A new type of control was proposed in this thesis. This new "flux" type control, as opposed to the "current" type, is based on the idea that the polarity of voltage applied to the coil must be switched at the times when the coil is completely saturated. To detect the saturation status it is suggested that the voltage accross the coil is measured. Since the flux does not change in the saturated core the zero coil voltage (which is the flux derivative) can be used for this purpose.

For circuits with "current" control it is important to correctly define the reference current levels. The detailed analysis of the current sensor sensitivity as a function of reference levels is presented in Chapter 2.

Certain factors can contribute to offset and hysteresis errors in the sensor output. The offset can result from asymmetrical power supplies and distortion of the magnetization loop associated with the undersaturated coil operation. The mechanism of such a distortion is discussed and the error calculation model is proposed. The loop distortion is typical only for the circuits employing the "current" type of multivibrator control and does not appear for the "flux" type circuits.

The model explaining the appearance of hysteresis in the sensor output is presented. The insufficient demagnetization current and the shift of the magnetization loop after the large pulse of input current are considered as the main sources of hysteresis error. To compensate the hysteresis the driving (demagnetization) current applied to the coil must be sufficiently high.

The basic isolation current sensor requires a circuit which will process the pulse-width modulated output signal. The simplest among data processing circuits discussed in Chapter 3 is a low-pass filter directly connected to the sensor output. This method though, can be used only for dc and ultra-low frequency measurements.

A high frequency sensor operation and related circuits were not considered in the previous studies. This problem therefore, was of a particular interest during the preparation of this thesis. Dual integration circuits can be used for converting the pulse-width modulated signal into the voltage level. To save the result of integration during the next oscillation cycle a sample-and-hold circuit must be connected to the integrator output. This data processing mechanism allows to achieve the highest possible conversion speed and maximize the measurement bandwidth.

To operate properly the data processing circuit requires a special timing unit which generates a series of digital commands. A correct sequence of these commands was studied, with the goal of eliminating data processing errors. As demonstrated, a circuit structure with "leading sampling" can provide an optimal functionality.

To obtain quantitative insight into the problem of measurement bandwidth and accuracy the analysis is presented with regard to an effect of amplitude distortion at the sample-and-hold output. Such distortion occurs whenever the operating frequency is not sufficiently high in comparison with the input signal frequency. Because of this factor the maximal measurement bandwidth of the current sensor as well as its accuracy are strongly dependent upon the sensor operating frequency.

To increase the sensor frequency the coil must have minimal inductance while the driving current must be as high as possible. In addition, it is important to use fast circuit components with the lowest switching times. An error budget associated with the finite comparator switching speed was evaluated.

The thesis presents the results of study concerned with the dead zone effect occurring in the current sensor output. This effect is caused by the fact that any transition between two opposite saturation limits inevitably include the region of the B-H curve which is associated with linear coil operation. Each oscillation cycle contains two such transitions which take equal amounts of time.

The dead zone occupies a large portion of each oscillation period and cuts down the dynamic range of the dual integration stage. Likewise, because of the smaller integrator output swing the S/N ratio of the data processing circuit is decreased. To solve this problem it was proposed to reduce the integration times in each direction by an equal time. This approach allows one even to completely exclude the dead zones from the integration stage, should this integration pause be set equal to the dead zone. As a result, the integration time constant can be reduced and the pulse-width difference can be obtained at the output with higher accuracy.

A radical solution to improving both the sensor S/N ratio and its operating frequency is provided by a circuit with dead zone reduction (DZR). The DZR controls the voltage level applied to the coil and increases it when the coil enters the dead zone. This forces the core magnetization to take place faster and reduces the dead times. As a result the oscillation frequency of the circuit with DZR can be dramatically increased. To provide an accurate dead zone reduction the voltage increase inside the dead zone must be equal for both half cycles.

Several practical circuits of the studied isolation current sensor were designed and experimentally tested.

A low-frequency experimental sensor operating at a frequency from 1000 to 3500 Hz was designed using the basic current sensor and a second order low-pass filter. Two types of isolation feedback control were designed and experimentally tested in conjunction with this circuit. The feedback uses a separate coil winding. The circuit

measures an input current in a range ±5 mA. The experimental nonlinearity of this current sensor for a large signal input is 2 %.

A 25 kHz experimental current sensor was designed using a high-frequency pulse transformer. The circuit uses the concept of dual integration with the output S/H, leading sampling and truncated integration times. The nonlinearity of the circuit with feedback is 0.08 % for the large-signal input in a range ±(0.2 - 2.2) mA. The above accuracy is guaranteed in the frequency range from dc to 1500 Hz.

A special study was conducted with regard to the hysteresis effect model presented in Chapter 2. It was experimentally verified that the higher driving current serves as an effective way to eliminate hysteresis from the output characteristics.

The experimental study showed that for both low and high frequency current sensors the feedback provides a strong linearization of the output characteristics. However, the feedback can not improve the low-signal performance of the sensor. All experimental current sensors demonstrated the large increase in nonlinearity for small input signals in comparison with large-signal operation. This increase can be accounted for by the noise characteristics of the transformers used in the study.

A circuit with dead zone reduction was designed and tested. The circuit employs a fast window comparator which controls the output swing of the Schmitt trigger. An increase of operating frequency from 25 kHz to 63 kHz was achieved without decline of sensitivity.

A digital processor was designed based on the FPGA CMOS IC. The circuit uses a concept of a synchronous up-and-down counter with an output latch memory. The circuit designed provides direct digital processing of the low-frequency sensor output signal. The IC provides 12 bit conversion accuracy when working with a 1000 Hz current sensor.

Several circuit concepts were not experimentally tested during the preparation of this thesis. Because the transformers used in experimental studies do not possess rectangular magnetization characteristics it was felt that the circuits with "flux" control will not provide substantial advantages over the "current" control circuits.

Another subject which was considered separate from the course of this thesis is the feedback circuit analysis. This issue involves some very important problems related to the general feedback theory as applied to the pulse-modulated systems.

During the preparation of this thesis some of the presented results were published [40], [41]. An area for future research would be a combination of a magnetic coil employing one of the special high-frequency low-noise materials with "flux" control circuit and a DZR unit. In conjunction with this future project it would be appropriate to test a special circuit of the interference suppresser proposed in Chapter 3.

References

1. System Application Guide, Analog Devices Inc., 1993.

2. Design-In Reference Manual, Analog Devices Inc., 1994.

3. Burr-Brown Integrated Circuits Data Book. Linear Products 1994, Burr-Brown Corporation, 1994.

4. Data Acquisition Catalog & Reference Guide, Volume 25, Keithley Metrabyte, 1992.

5. IEEE-488 and VXIbus Control, Data Acquisition, and Analysis, National Instruments Corporation, 1992.

6. M. Abe, H. Tsujimura and J. Nakazoe, "A magnetic-modulator-type current-dividing highly stable dc current transformer for large current," CPEM 90 (Conference on Precision Electromagnetic Measurements), pp. 365-366, 1990.

7. C. Sullender, "Magnetic current sensors for Space Station Freedom," IEEE Transactions on Power Electronics, vol. 8, no. 1, pp. 69-75, 1993.

8. H. Kiwaki, S. Shima, K. Nakamura and K. Shimada, "Wide-range high-accuracy current sensor using magnetic cores," Japan Annual Reviews in Electronics, Computers & Telecommunications. Recent Magnetics for Electronics, pp. 187-196, 1985/1986.

9. M. F. Zirngast, "Capacitive isolation expands analogue design options - Part 1," Electronic Engineering (London), vol. 61, no 748, pp. 37-38, 40, April 1989.

10. T. Sonoda, R. Ueda and K. Koga, "An ac and dc current sensor of high accuracy," IEEE Transactions of Industry Applications, vol. 28, no. 5, pp. 1087-1094, 1992.

11. D. Son and J. Sievert, "A new current sensor based on the measurement of the apparent coercive field strength," IEEE Transactions on Instrumentation and Measurement, vol. 38, pp. 1080-1082, 1989.

12. K. Harada and H. Sakamoto, "Current sensors with a small saturable core and MOSFETs," IEEE Transactions on Magnetics, vol. 24, no. 6, pp. 2910-2912, November 1988.

13. I. M. Filanovsky and V. A. Piskarev, "Sensing and measurement of dc current using a transformer and RL-multivibrator," IEEE Transactions on Circuits and Systems, vol. 38, no. 11, pp. 1366-1370, November 1991.

14. I. M. Filanovsky and L. Taylor, "Circuit with nonlinear transformer allowing dc current measurements via an isolation gap," Proceedings of the 35th Midwest Symposium on Circuits and Systems, vol. 1, pp. 318-323, 1992.

15. I. M. Filanovsky and V. A. Piskarev, "Design of electromagnetically coupled isolation operational amplifiers without input buffer," Proceedings of the 36th Midwest Symposium on Circuits and Systems, vol. 2, pp. 1414-1418, 1993.

16. I. M. Filanovsky and V. A. Piskarev, "RL-multivibrator and retrieving the coil magnetization curve," IEEE Transactions on Circuits and Systems, vol. 38 no. 6, pp. 650-653, June 1991.

17. A. Semlyen and F. de Leon, "Complete transformer model for electromagnetic transients," IEEE Transactions on Power Delivery, vol. 9, no. 1, pp. 231-238, January 1994.

18. T. Novak and F. C. Trutt, "Theoretical analysis of a dc saturable-reactor ground fault protection system," IEEE-IAS-1984 Industry Applications Society Annual Meeting, pp. 133-138, 1984.

19. F. C. Trutt, E. A. Erdelyi and R. E. Hopkins, "Representation of the magnetization characteric of dc machines for computer use," Transactions IEEE-IAS-1968, pp. 151-154, March 1968.

20. B. D. Cullity, Introduction to Magnetic Materials, Addison-Wesley, New York, 1972.

21. H. J. Williams, Physical Review, vol. 52, pp. 747-752, 1937.

22. S. Chikazumi, Physics of Magnetism, Wiley, New York. 1964.

23. D. C. Jiles, and D. L. Atherton, "Theory of ferromagnetic hysteresis," Journal of Magnetism and Magnetic Materials, vol. 61, pp. 48-60, 1986.

24. V. Ostovic, Dynamics of Saturated Electric Machines, Springer-Verlag New York, 1989.

25. C. E. Lin, C. L. Cheng and C. L. Huang, "Hysteresis characteristic analysis of transformer under different excitation," IEEE Transaction on Power Delivery, vol. 6, no. 2, pp. 873-876, April 1991.

26. J. K. Watson, Applications of Magnetism, John Wiley & Sons, New York, 1980.

27. Tape wound cores, Design Manual, Magnetics Corporation, TWC-400, 1995.

28. S. Takeuchi and K. Harada, "A resonant-type amorphous ribbon magnetometer driven by an operational amplifier," IEEE Transactions on Magnetics, vol. MAG-20, no. 5, pp. 1723-1725, September 1984.

29. L. A. Bessonov, Theoretical Electrical Engineering, Moscow, 1967.

30. D. Dolinar, J. Pihler and B. Grcar, "Dynamic model of a three-phase power transformer," IEEE Transactions on Power Delivery, vol. 8, no. 4, pp. 1811-1815, October 1993.

31. J. R. Lukas, P. G. McLaren, W. W. I. Keerthipala and R. P. Jayasinghe, "Improved simulation models for current and voltage transformers in relay studies," IEEE Transactions on Power Delivery, vol. 7, no. 1, pp. 152-154, January 1992.

32. R. Boll and K. J. Overshott, Magnetic Sensors, vol. 2, VCH, Veiden, Germany, 1989.

33. D. I. Gordon and R. E. Brown, "Recent advances in fluxgate magnetometry," IEEE Transactions on Magnetics, vol. MAG-8, no. 1, pp. 76-82, March 1972.

34. Rudy van de Plassche, Integrated Analog-to-Digital and Digital-to-Analog Converters, Kluwer Academic Publishers, Boston, 1994.

35. H. W. Katz, Solid State Magnetic and Dielectric Devices, John Willey & Sons, New York, 1959.

36. P. Ripka, "Review of fluxgate sensors," Sensors and Actuators, part A, vol. 33 pp. 129-141, 1992.

37. D. C. Scouten, "Noise in low-level flux-gate magnetometers," IEEE Transactions on Magnetics, MAG-8, pp. 223-231, 1972.

38. O. V. Nielsen, J. R. Petersen, A. Fernandez, B. Hernando, P. Spisak, F. Primdahl and N. Moser, "Analysis of a fluxgate magnetometer based on metallic glass sensor," Measurement Science and Technology, vol. 2, pp. 435-440, 1991.

39. T. Sonoda, R. Ueda, T. Irisa and S. Takata, "Application of an amorphous core with high permeability and rectangular characteristics to current zero point detection and current sensing in noncirculating cycloconverter," IEEE-IAS-1984 Annual Meeting Proceedings, pp. 754-759, 1984.

40. A. Vainshtein and I. M. Filanovsky, "Electromagnetically coupled dc and ac current sensor and detector with digital processing of output data," ASEE Annual Conference Proceedings, pp. 857-860, 1994.

41. A. Vainshtein and I. M. Filanovsky, "Isolation electromagnetically coupled dc and ac current sensor and detector," Proceedings of the 1994 IEEE International Symposium on Circuits and Systems. Part 5 (of 6), pp. 69-72, 1994.

Appendix 1. PSPICE simulation

DIS16.NET

```
* Schematics Netlist *

R_R1      0 $N_0001 100k
R_R2      $N_0002 0 0.01k
R_R3      $N_0004 $N_0003 10k
R_R4      0 $N_0004 8k
V_V1      $N_0005 0 DC -15V
V_V2      $N_0006 0 DC +15V
Q_Q1      $N_0006 $N_0007 $N_0003 Q2N3904
Q_Q2      $N_0005 $N_0007 $N_0003 Q2N3906
X_U1      $N_0004 $N_0002 $N_0006 $N_0005 $N_0007 uA741
L1_TX1    $N_0010 0 200
L2_TX1    $N_0003 $N_0002 200
K_TX1     L1_TX1 L2_TX1 0.99 K3019PL_3C8-X
I_I1      $N_0001 $N_0010 DC 0.2A
```

```
**** 03/20/95 22:07:46 ********** Evaluation PSpice (Jan 1994) *************
 * F:\DATA\ISOL-AMP\DIS16.SCH

 ****     CIRCUIT DESCRIPTION

*******************************************************************************


* Schematics Version 6.0 - January 1994
* Mon Mar 20 22:07:33 1995


** Analysis setup **
.tran 0.0001s 0.02s UIC
.LIB DIS13.lib


* From [SCHEMATICS NETLIST] section of msim.ini:
.lib nom.lib
.lib F:\MSIMEV60\LIB\EVAL.LIB

.INC "DIS16.net"

**** INCLUDING DIS16.net ****
* Schematics Netlist *


R_R1      0 $N_0001 100k
R_R2      $N_0002 0 0.01k
R_R3      $N_0004 $N_0003 10k
R_R4      0 $N_0004 8k
V_V1      $N_0005 0 DC -15V
V_V2      $N_0006 0 DC +15V
Q_Q1      $N_0006 $N_0007 $N_0003 Q2N3904
Q_Q2      $N_0005 $N_0007 $N_0003 Q2N3906
X_U1      $N_0004 $N_0002 $N_0006 $N_0005 $N_0007 uA741
L1_TX1    $N_0010 0 200
L2_TX1    $N_0003 $N_0002 200
K_TX1     L1_TX1 L2_TX1 0.99 K3019PL_3C8-X
I_I1      $N_0001 $N_0010 DC 0.2A

**** RESUMING DIS16.CIR ****
.INC "DIS16.als"

**** INCLUDING DIS16.als ****
* Schematics Aliases *

.ALIASES
R_R1          R1(1=0 2=$N_0001 )
R_R2          R2(1=$N_0002 2=0 )
R_R3          R3(1=$N_0004 2=$N_0003 )
R_R4          R4(1=0 2=$N_0004 )
V_V1          V1(+=$N_0005 -=0 )
V_V2          V2(+=$N_0006 -=0 )
Q_Q1          Q1(c=$N_0006 b=$N_0007 e=$N_0003 )
```

```
Q_Q2          Q2(c=$N_0005 b=$N_0007 e=$N_0003 )
X_U1          U1(+=$N_0004 -=$N_0002 V+=$N_0006 V-=$N_0005 OUT=$N_0007 )
L1_TX1        TX1(1=$N_0010 2=0 )
L2_TX1        TX1(3=$N_0003 4=$N_0002 )
X_TX1         TX1()
I_I1          I1(+=$N_0001 -=$N_0010 )
.ENDALIASES

**** RESUMING DIS16.CIR ****

.probe

.END
*
**** 03/20/95 22:07:46 *********** Evaluation PSpice (Jan 1994) *************

 * F:\DATA\ISOL-AMP\DIS16.SCH

 ****      Diode MODEL PARAMETERS

********************************************************************************



            X_U1.dx
       IS   800.000000E-18
       RS     1

*
**** 03/20/95 22:07:46 *********** Evaluation PSpice (Jan 1994) *************

 * F:\DATA\ISOL-AMP\DIS16.SCH

 ****      BJT MODEL PARAMETERS

********************************************************************************



            Q2N3904          Q2N3906          X_U1.qx
            NPN              PNP              NPN
       IS    6.734000E-15     1.410000E-15   800.000000E-18
       BF   416.4            180.7            93.75
       NF     1                1               1
      VAF    74.03            18.7
      IKF      .06678           .08
      ISE    6.734000E-15
       NE    1.259
       BR      .7371           4.977           1
       NR     1                1               1
       RB    10               10
      RBM    10               10
       RC     1                2.5
```

```
        CJE    4.493000E-12    8.063000E-12
        MJE     .2593            .3677
        CJC    3.638000E-12    9.728000E-12
        MJC     .3085            .5776
         TF  301.200000E-12  179.300000E-12
        XTF    2                6
        VTF    4                4
        ITF     .4               .4
         TR  239.500000E-09   33.420000E-09
        XTB    1.5              1.5

**** 03/20/95 22:07:46 ********** Evaluation PSpice (Jan 1994) **************

 * F:\DATA\ISOL-AMP\DIS16.SCH

 ****     Ferromagnetic Core MODEL PARAMETERS

*******************************************************************************



           K3019PL_3C8-X
     LEVEL    2
      AREA    1.38
      PATH   40.52
        MS  415.200000E+03
         A   44.82
         C     .4112
         K   25.74
     ALPHA    0


        JOB CONCLUDED

        TOTAL JOB TIME           97.11
```

Appendix 2. FPGA IC - digital processor for current sensor

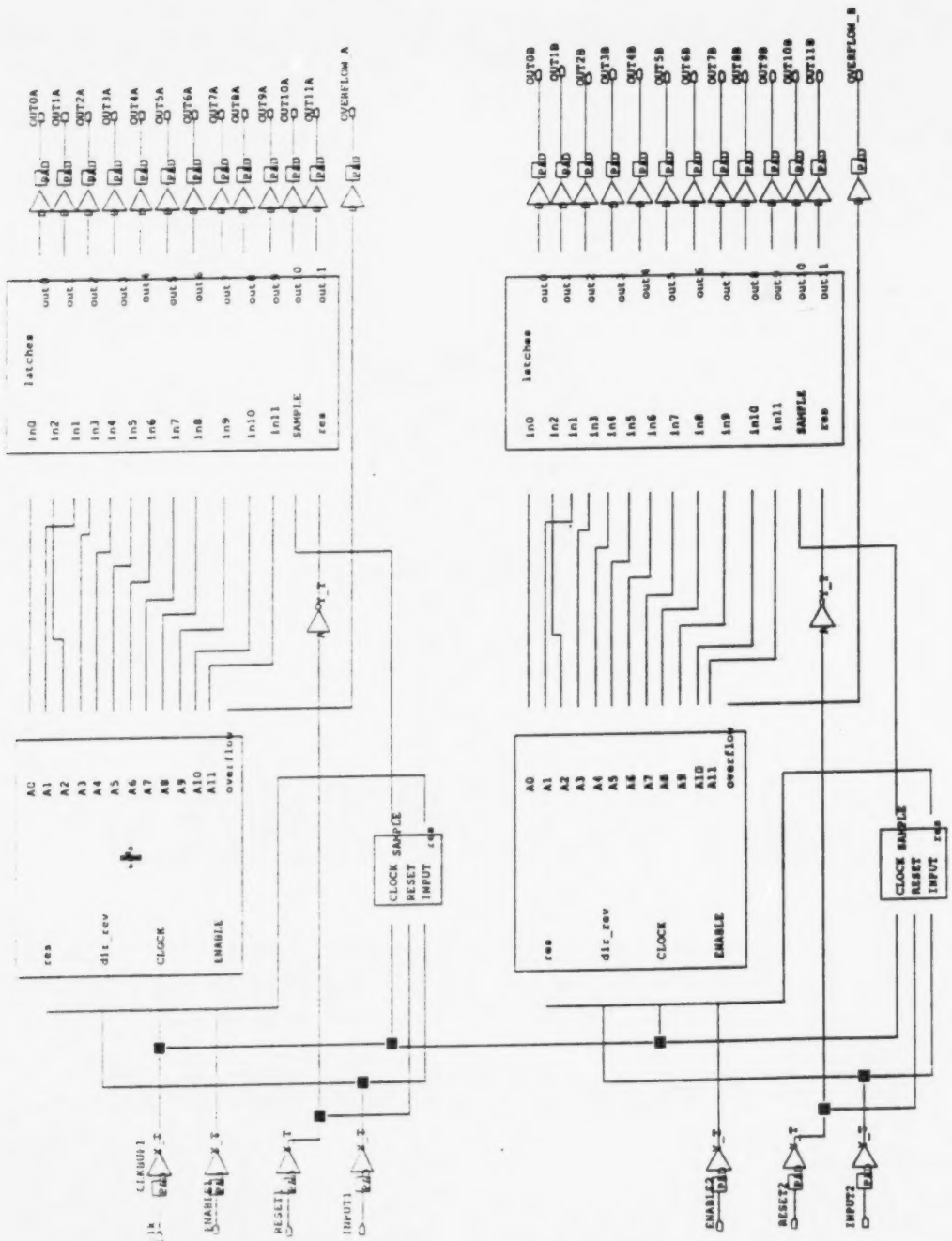
latches
SAMPLE
res
dir_rev
CLOCK
ENABLE
overflow
CLOCK SAMPLE
RESET
INPUT
OUT0A
OUT1A
OUT2A
OUT3A
OUT4A
OUT5A
OUT6A
OUT7A
OUT8A
OUT9A
OUT10A
OUT11A
OVERFLOW_A
OUT0B
OUT1B
OUT2B
OUT3B
OUT4B
OUT5B
OUT6B
OUT7B
OUT8B
OUT9B
OUT10B
OUT11B
OVERFLOW_B
CLKOUT1
ENABLE1
RESET1
INPUT1
ENABLE2
RESET2
INPUT2

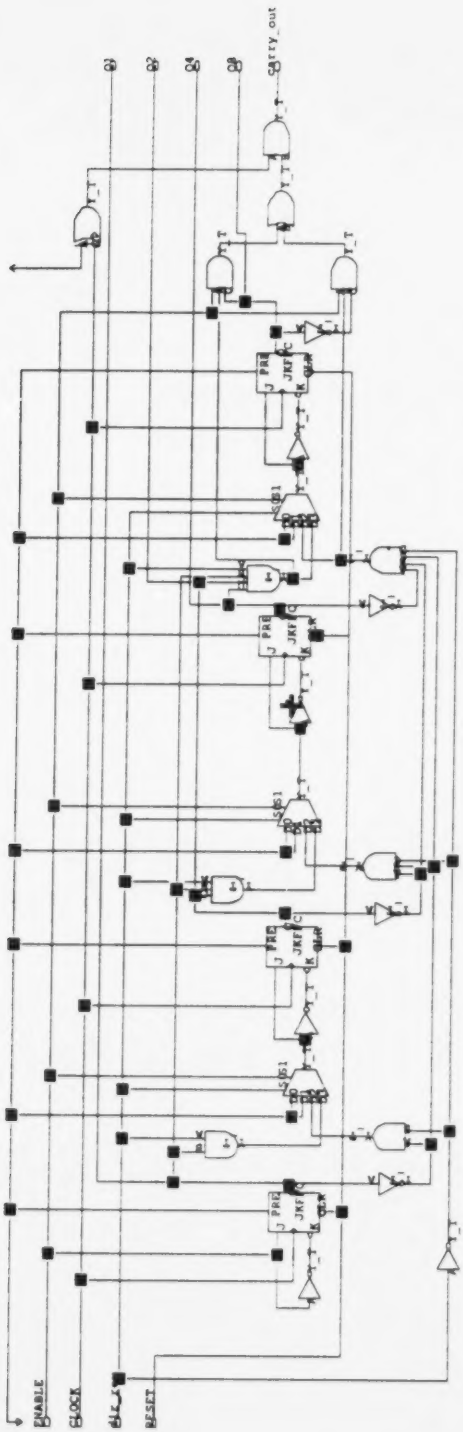
Q1
Q2
Q4
Q8
carry_out
ENABLE
CLOCK
RESET

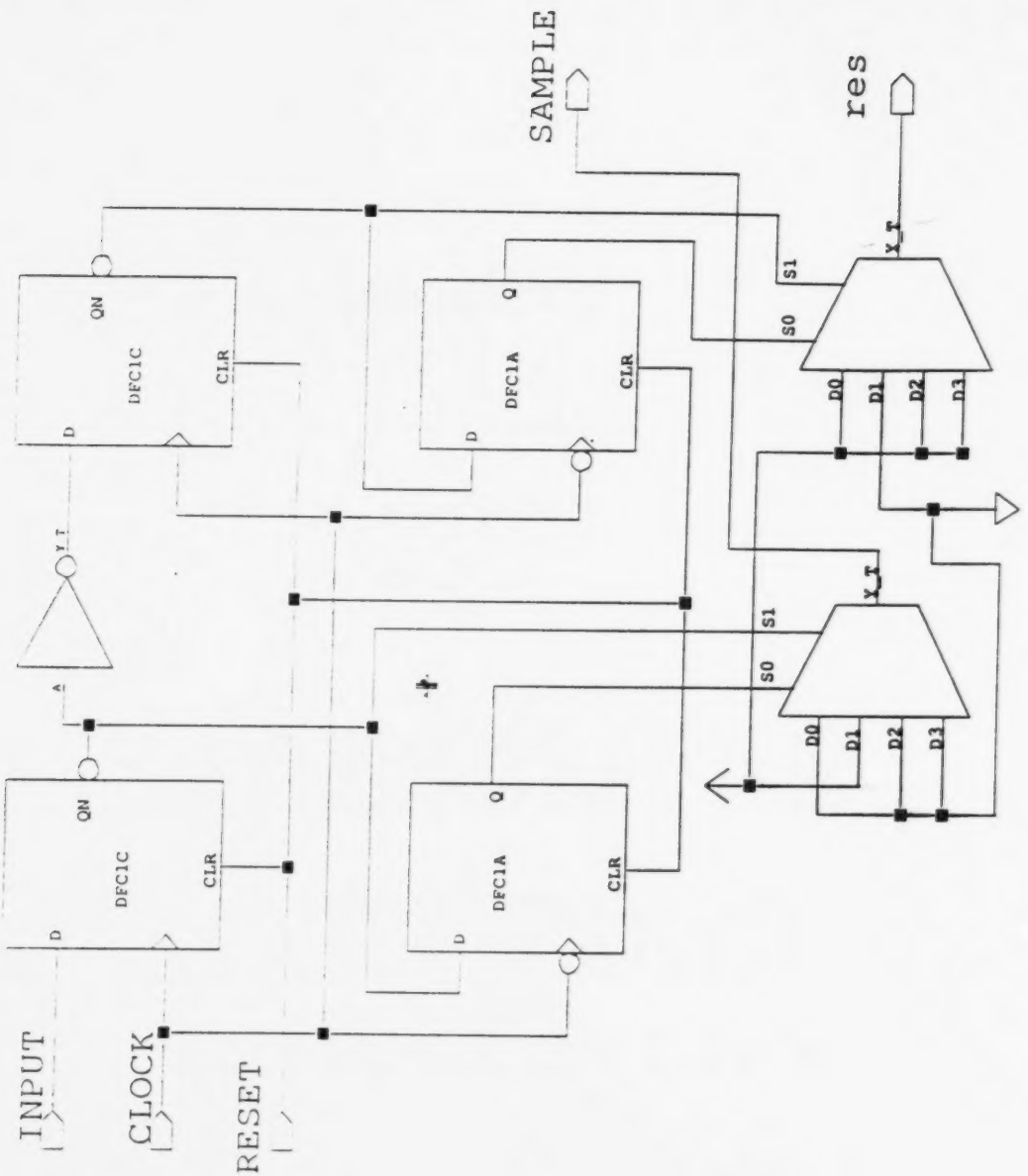
SAMPLE
res
INPUT
CLOCK
RESET
DFC1C
DFC1A
QN
Q
D
CLR
Y_T
A
S0
S1
D0
D1
D2
D3

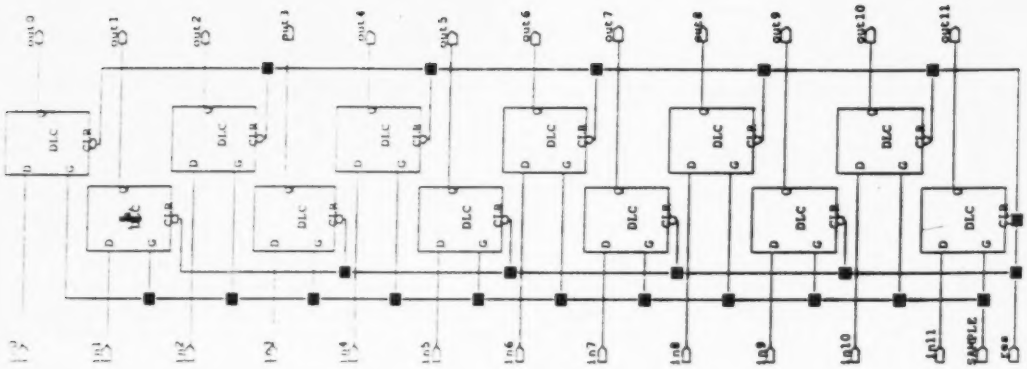
DLC
SAMPLE

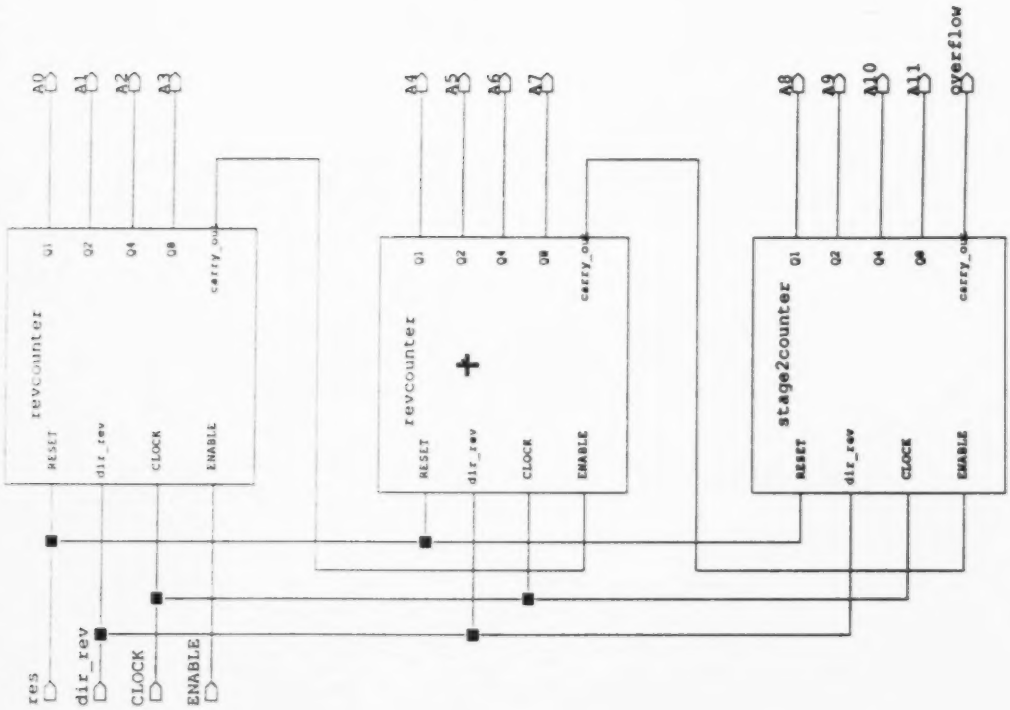
revcounter
RESET
dir_rev
CLOCK
ENABLE
carry_out
stage2counter
overflow
res
dir_rev
CLOCK
ENABLE

```
DEF Current Detector
NET ENABLE1; ; PIN:1.
NET ENABLE2; ; PIN:2.
NET RESET1; ; PIN:4.
NET RESET2; ; PIN:5.
NET INPUT1; ; PIN:6.
NET INPUT2; ; PIN:7.
NET OUT0A; ; PIN:8.
NET OUT1A; ; PIN:9.
NET OUT2A; ; PIN:11.
NET OUT3A; ; PIN:12.
NET OUT4A; ; PIN:13.
NET OUT5A; ; PIN:15.
NET OUT6A; ; PIN:17.
NET OUT7A; ; PIN:18.
NET OUT8A; ; PIN:19.
NET OUT9A; ; PIN:20.
NET OUT10A; ; PIN:22.
NET OUT11A; ; PIN:23.
NET OUT1B; ; PIN:24.
NET OUT2B; ; PIN:26.
NET OUT3B; ; PIN:27.
NET OUT4B; ; PIN:28.
NET OUT5B; ; PIN:29.
NET OUT6B; ; PIN:30.
NET OUT7B; ; PIN:31.
NET CLK; ; PIN:33.
NET OUT8B; ; PIN:36.
NET OUT9B; ; PIN:37.
NET OUT10B; ; PIN:38.
NET OUT11B; ; PIN:39.
END.
```